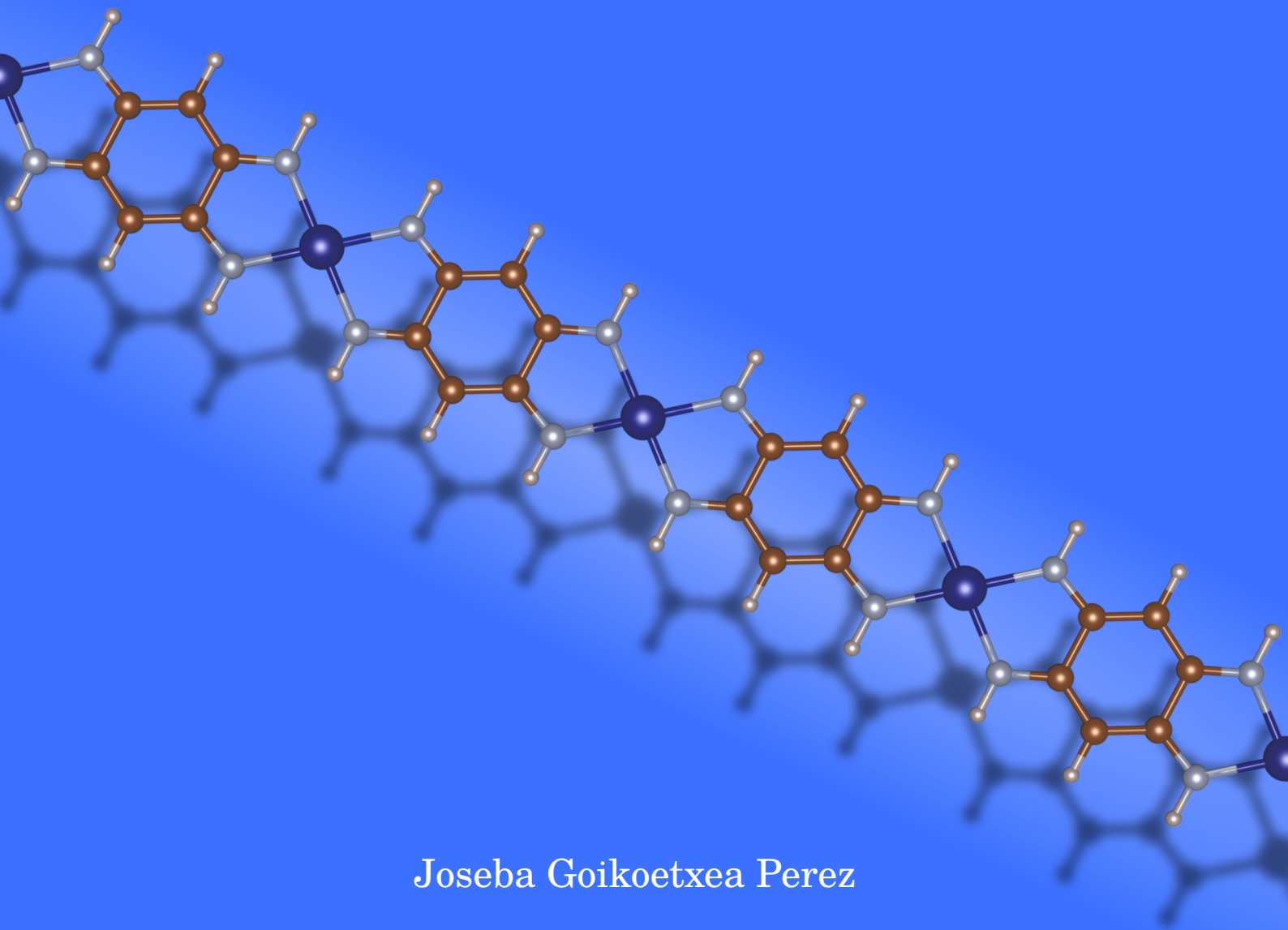


Electronic correlation and magnetic properties of one-dimensional systems



Joseba Goikoetxea Perez

Supervised by

Andrés Arnau Pino & María Blanco Rey



Universidad
del País Vasco

Euskal Herriko
Unibertsitatea

CAMPUS OF
INTERNATIONAL
EXCELLENCE

Electronic correlation and magnetic properties of one-dimensional systems

Joseba Goikoetxea Perez

Supervised by

Andrés Arnau Pino

María Blanco Rey

June 17, 2022



Zientziaren berri duen gizartea askeagoa eta manipulagaitzagoa da.

Zientziaren Giltzak

Aume, ama, aita, sis, loba, familixa eta lagun, zeuentzat

Contents

Contents	ix
Acknowledgements	xi
Laburpena	xiii
1 Introduction	1
2 Theoretical methods	9
2.1 The Many-Body problem in Condensed Matter Physics	9
2.2 Density Functional Theory	12
2.3 Spin-Orbit Coupling (SOC)	22
2.4 Constrained Random Phase Approximation (cRPA)	26
2.5 Maximally Localized Wannier Functions	30
3 Magnetic properties of planar free-standing transition metal oxide chains	35
3.1 Introduction	35
3.2 Structure model	37
3.3 Planar free-standing chain: Spin phase diagrams	37
3.4 Magnetic coupling in planar free-standing chains	40
3.5 Magnetic Anisotropic Energy in planar free-standing chains	42
3.6 Conclusions	47
4 Electronic correlation and multiplet effect in TMO chains	51
4.1 Introduction	51
4.2 Computational details	53
4.3 Planar free-standing XO_2 chains	57
4.4 Supported XO_2 chains on Ir(100)	66
4.5 Conclusions	73

5	Magnetic properties of transition metal-organic chains: the Co-QDI and CrQDI cases	75
5.1	Introduction	75
5.2	Computational details	77
5.3	Magnetic anisotropy and exchange coupling	85
5.4	Conclusions	91
	Conclusions	95
	Appendix A Magnetic Anisotropy Energy (MAE) convergence test	99
A.1	Convergence details	99
	Appendix B cRPA calculations	101
B.1	FLEUR and SPEX convergence parameters	101
B.2	cRPA calculation results	102
	Bibliography	105

Acknowledgments

May your heart be your guiding
key

Kingdom Hearts

These years have been awesome and awful, the full experience of science. I have been able to experience the beauty of science when you find something unexpected, the despair that brings all the questions arising (and calculations to do) and the joy when you find the answers. After almost four years, we reach the end of the Ph.D., and my journey into Academia with it. But, before this chapter of my life closes I feel the need to thank all the people that have been part of this journey.

First of all, I am really thankful to my supervisors Andres and Maria. Without your guidance, this Thesis would have been a sketch of what it has become. Even though, as Andres said once: "By the end of the Ph.D. you won't stand us." time has shown that this was true at certain moments! But, I am really grateful for the help you have given to me discussing the results and the patience you have shown with me. I am very grateful to Gustav Bihlmayer, as without the stay in the Forschungszentrum in Jülich this Ph.D. could have been very differently and half the interesting as it is now.

In 2018 the journey of the Ph.D. started after the CFM organized the Ph.D. fair, also known as the Hunger Games. In this journey, I have met many amazing people, so let's give it up to the crew of CFM! So, let's begin with the old (old) group that I first met in the CFM: Unai, Thomas, Andrea, Moritz and certainly Iker, thanks for your patience every time I went to ask you questions about the calculations when I started. 2020 arrived and a pandemia with it, modifying our life from day to night. After this pandemia and the old people were gone, the CFM crew totally changed for these last years. I am really grateful to Alvaro, Antton,

Adrian, Arru, August, Bruno, Carmen, Charlie, Cris larga, Cris corta, Fernando, Iker, Jon, Jorge grande, Jorge largo, Marina, Martin, Miguelf, Txemikel, Roberto and more! Thanks for all the beers after work, and the Drag Race viewing parties! Thanks to Jose, Francesco, Antonella, and Josu, for the laughs in the office and make this journey a bit more endurable! Last but not least, Idoia, I am really thankful to you. Thank you for the outreach activities you organize and let us be part of them. Each time I was in, I thought about how much I enjoyed physics. I hope you continue for many years like that!

Ah, zer, nire tesisin Ondarrutar enebalakun idatziko? Eon pixkatin! Eskerrik asko kuadrillako danai, natxe satellite baten latxeik ibili alkar ikusten gazenin zelan nabilen galdetzezuelako, natxe moska laga eta tutik ez ulertu ikerkuntzako mundun interesa jartzezuelako eta animuk emotetzazelako. Gradukuai, Amaia, Ainhoa, Lete, Iker, Aitor etab. dudaik eztakat zuek ezpaziñake eongo Fisika ikasten eongiñan (inpernuko) urtitan hona enitxakela allako.

Aume dana ondo juteko horrenbeste kandela ipinitxe gero tarjeta vip-e emonbikotzenela elixan, eta nire aukera guztik babestuzuzelako. Eta azkaneako, ama, aita eta sis, Fisika ikastea dezidiu neban momentun natxe harrixute gelditxu aurrea jarraitzeko animaztazue natxe hau mundu zuek ezautuzuenetik oso aparte gelditxu, eta edozein problema eukiaz laguntzeko prest zaze. Eta azkan agurre urtitan Ondarrure jun nazen momento guztik eurak ikusi hutsaz pozten nabena neure lobantzat Julen, eta azkan adiziñoi Nikole. Matxe-matxe eta muso bat danontzat!

That's all folks!

Laburpena

Tesi honen helburu nagusia, nanokate magnetiko desberdinetan, magnetismoaren eta elektroien arteko korrelazioaren analisi teorikoa egitea da. Egitura sinpleak izan arren, dimentsio baxuko sistemak ezaugarri magnetiko interesgarriak erakutsi ahal dituzte. Esperimentalki horrelako sistemak gauzatzeak erronka handia suposatzen du, eta ondorioz neurketak egitea ia ezinezkoa bihurtzen da. Beraz, analisi teorikoa ezinbestekoa da material horien ezaugarriak aurreikusteko. Gure lanaren lehendabiziko helburuan, kateen eta katea hazten den sustratuaren arteko elkarrekintzak aztertzen ditugu. Bi kasu ezberdin ditugu, lehena sustratua eta katearen artean elkarrekintza handiak daudenean eta bigarrena, elkarrekintza baxuak direnean, hau da, katea sustratuarekiko isolatuta egongo balitz bezala aintzat hartuz. Kate-sustratu elkarrekintzak elektroien korrelazioa erabat aldatu dezake, eta ondorioz, kateen magnetismoa guztiz aldarazi. Gure bigarren eta azken helburua, atomo magnetikoek erakutsi ahal duten egoera desberdinek (spin desberdin edo berdinarekin) propietate magnetikoetan duten eragina aztertzea da.

XX. mendean material magnetikoen ezagutzak izan zuen iraultzaz geroztik, material hauek gure egunerokotasuneko parte izatera pasa dira. Material magnetikoen erabilera ezagunena datuak gordetzeko ahalmena da: ordenagailuetako disko gogorrek material magnetikoz osatuta daude. Tresneria hauetan domeinu magnetikoen (atomoen momentu magnetikoek norabide orokorra duten eskualdeak) magnetizazioa neurtzen da, momentu magnetikoaren noranzkoak 0 edo 1 bit kodea ezartzen duelarik. Azken urte hauetan, mundu mailako datu kopuruak esponentzialki gora egin du, beraz memoria handiagoak duten disko gogorren beharra dugu. Kontutan izanda informazioa domeinu magnetikoetan gordetzen dela, memoria handitzeko modu bakarra domeinuak txikitzea da. Gaur egun, disko gogorretan 10^{16} bit/m²-ko oroimenen dentsitatea lor dezakete, hau da, domeinuak gutxi gorabehera 10 nm²-koak dira. Domeinu magnetikoen tamaina txikitzeak, domeinuen arteko hormak txikitzean lortzen da. Hormen tamaina bi elkarrekintzen araber-

akoa da: truke elkarrekintzak eta anisotropia magnetikoak. Truke elkarrekintzak atomoen arteko spinak lerrokatzearen alde egiten du, eta anisotropia magnetikoak spinak kristalaren norantza zehatz batean egoteak lehenesten du. Beraz, trukeak domeinuen arteko hormak luzatzea hobesten du, anisotropiak, ordea, horma motzagoak. Domeinu magnetikoen tamaina txikitzeak muga bat du, txikitzean efektu termikoak gero eta nabariagoak baitira, magnetizazioaren ausazko alderantziketarik sortuz. Muga honi muga superparagnetikoa deritzogu. Domeinu magnetikoen txikitzearen limitea dimentsio baxuko sistemekin gainditu dezakegu.

Dimentsio baxuko materia sorta bidimentsionalak (2D) diren sistemetatik imanen limitea den atomora (0D) arteko sistemek osatzen dute. Gure ikerkuntza dimentsio bakarreko (1D) sistemetan zentratuta dago. Zehazki, Tesi honetan, bi kate magnetiko mota aztertuko ditugu, bat trantsizio-metal atomoak O atomoekin lotura dutenean, hots, trantsizio metal-oxido kateak, eta bestean, trantsizio-metalak molekula organikoen bidez lotzen direnean. Zergatik dimentsio baxuak erabili? Sistemen dimentsioa txikitzen denean, gorputz anitzen arteko elkarrekintzak gora egiten du. Loturak dituzten atomo kopurua gutxitzen direnez, elektroien arteko Coulomb elkarrekintzak handiagoak dira, apantailatze efektuak txikiagotzen baitira. Ondorioz, spin-spin arteko truke elkarrekintza areagotzen da. Mermin-Wagner teoriaren arabera dimentsio baxuko materialetan ezin da ausazko irismen luzeko magnetismorik eman, baldin eta anisotropia magnetikorik ez badago. Beraz, anisotropia magnetikoa ezinbestekoa da dimentsio baxuetan magnetismoa gauzatzeko. Gainera, dimentsio baxuetan eremu kristalinoa (beste atomoek sortutako potentzial elektrikoaren konbinazioa) txikiagotzen da, elektroien momentu orbitalaren deuseztapena ezabatuz eta anisotropiari balio handiak izatea ahalbidetuz. Are gehiago, sistemen simetria ere txikiagotzen da, adibidez, inbertsio simetriarik ez dago, eta spinen arteko truke elkarrekintza handitzen denez, kolinealak ez diren spin egiturak egotea ahalbidetzen ditu, baita beste motatako elkarrekintzak agertu ere, adibidez, truke antisimetrikoa, spin egitura kiralak ahalbidetuz. Propietate horiek dimentsio baxuko sistemak gailu elektronikoetan erabiltzeko oso erakargarriak egiten dituzte. Baina batez ere, kateen ezaguarri magnetikoek interes handiena spintronikaren alorrean sustatzen dute, hau da, elektroien kargaz gain spina ere manipulatzeko ahalbidetzen duten tresnerien ikerkuntzan.

Lehenago aipatu dugun bezala, kalkulu teorikoak ezin bestekoak dira kateen propietateak aurreikusteko. Gure analisi teorikoa gauzatzeko dentsitate funtzionalaren teoria (DFT) erabili dugu. Metodo honek parametro empirikoen erabilera saihesten du, konputazio denboraren eta zehaztasunaren arteko balantzea orekatuta

mantenduz. Spina kontutan hartzen duten DFT kalkuluekin materialen propietate magnetikoak lortu ditzakegu, hala nola, spin egoera eta truke elkarrekintza konstantea \mathcal{J} . DFT kalkuluetan spin orbita elkarrekintza (SOE) sartuta anisotropia magnetikoaren energia lortu ahal dugu. DFT partikula bakarreko problematan oinarritzen denez gorputz askoko elkarrekintzak ez ditu ondo deskribatzen. Arazo hau argi ikusten da trantsizio-metal atomoetan, non, d orbitalean dauden elektroiek elkarrekintza handiak izan ahal duten. Coulomb elkarrekintzaren deskribapen mugatuaren ondorioz, materialen ezaugarrien emaitza okerrak izan ahal ditugu, adibidez, sistema metalikoa berez isolatzailea denean. Hau konpontzeko DFT+ U zuzenketa erabiltzen da, non, U parametroak orbital jakin bateko elektroien elkarrekintza deskribatzen duen. Honez gain, DFT metodo bariazionala izanik, energiaren minimizazio prozesu baten bitartez lortzen du oinarritzko egoera. Prozedura hau zehatza izango balitz beti energia gutxineko egoeran amaituko genuke, hau da, oinarritzko egoeran. Energiaren minimizazioaren prozedura ez denez perfektua, energetikoki baxuak diren egoera kitzikatuetan bukatu dezakegu, oinarritzko egoera saiheztuz.

Tesiak hurrengo egitura du:

2. atalean, lehendabizi, Estatu Solidoko Fisikan erabiltzen diren ekuazioen eta hurbilketen sarrera labur bat emango dugu. Bigarrenez, DFT teoriaren oinarritzko teorema eta ekuazioak azalduko ditugu, DFT+ U zuzenketarekin eta orbitalen okupazio kontrolaren metodoarekin batera. Jarraian, anisotropia magnetikoaren energia kalkulatzeko erabili ditugun bi metodoak azalduko ditugu: indar teorema eta autokonsistentzia zikloak. Amaitzeko, mugatutako ausazko fase hurbilketa azalduko dugu, metodo honekin elektroien elkarrekintza intraorbital, U , eta elkarrekintza interorbitala, J , parametroak kalkulatu ahal ditugu. Honekin batera maximoki lokalizatuta dauden Wannierren funtzioen azalpen labur emango dugu.

3. eta **4. ataletan**, trantsizio metal-oxido kateetan oinarrituko gara, XO_2 non $X = Ni, Co, Fe$ eta Mn izanik, $Ir(100)$ sustratuan hazita. **3. atalean**, isolatutako kateen propietate magnetikoak kalkulatuko ditugu. Atomoen arteko distantzia eta Hubbard- U parametroa aldatzen ditugunean hainbat spin egoera lortu ditzakegu atomo magnetikoetan. Zenbat eta U parametro handiagoa izan, orduan eta spin balio handiagoa lortzen ditugu. Katearen gela unitatea bikoiztuz, eta egoera antiferromagnetiko (AFM)-pin antiparaleloak- edo ferromagnetikoa (FM)-spin paraleloak- ezarriz, truke elkarrekintza kalkulatu dugu. Kate guztiak AFM egoera lehenesten dute, MnO_2 -k izan ezik, FM egoera nahiago izanda. Spin egitura bakoitzerako egoera dentsitateak kalkuluek MnO_2 kasuan FM egoera erdi-eroalea da erakusten dute. AFM egoera eroalea izanik. Beste kateetan aldiz AFM

egoera isolatzailea da. Beraz, spin egituraren lehenespena materialen metaltasunarekin zerikusia du. Azkenik, anisotropia magnetikoa kalkulatu dugu indar teorema eta kalkulu autokonsistenteak erabiliz. Bi metodoek ardatz leun (energia gutxieneko norabidea) berbera ematen dute, NiO_2 eta CoO_2 kateentzat katearen planoan baina bere norabidearekiko perpendikularra, eta beste bi kasuetan, FeO_2 eta MnO_2 , katearen planoarekiko perpendikularra. Baina NiO_2 kasuan balioak oso desberdinak dira, balio autokonsistentea indar teoremarena baino hiru bidar handiagoa izanik. Bi metodoak aplikatu eta geroko egitura elektronikoa kalkulatu dugu aldaketa horren arrazoa lortzeko. Egitura elektronikoa argi uzten du indar teoremak ez duela ondo deskribatzen SOE efektua Fermi maila inguruan. Honen arrazoa, gure materialaren dimentsio baxua izan ahal da. Simetriak gutxitzen direnez, elektroien uhin funtzioak ez daude mugatuta, beraz SOE ezartzean bilakaera handiagoa eman ahal da, eta indar teorema ez da gai deskribatzeko. Azkenik, anisotropia magnetikoaren energiaren dentsitatea kalkulatu dugu, hau da, autoenergia bakoitzak anisotropia magnetikoaren energian duen ekarpena. Honekin, kateen artean ardatz leunaren aldaketaren arrazoa bilatu ahal dugu, SOEaren ondorioz emandako banda banaketa garrantzitsuenak bilatuz eta banden orbitalen proiektzioa erabiliz.

4. atalean, X atomoetako $3d$ orbitalean ematen diren Coulomb elkarrekintzak azterkuko ditugu. Mugatutako ausazko fase hurbilketa erabiliz, U -ren zein J -ren balioak lortu ditzakegu. Lehendabizi, isolatutako katearen interakzioa kalkulatu dugu. Kate guztientzat $J \sim 1$ eV lortzen dugu. FeO_2 kate isolatzailean lortzen dugu balio handiena $U \sim 7.7$ eV, gainerakoak erdi-eroaleak izanik $U \sim 6$ eV balioa lortzen dugu. NiO_2 katen bi egoera desberdin lortzen ditugu, C1 eta C2 egoerak, DFT kalkuletan ezartzen dugun U balioaren arabera. Bi egoera hauek, bi U balio desberdin ematen dituzte mugatutako ausazko fase hurbilketa kalkuletan, batek $U^{C1} \sim 6$ eV eta besteak $U^{C2} \sim 2.4$ eV. Korrelazio espazioa aldatuz $O(p)$ orbitala interakzioaren apantaimenduan ekarpen handiena duen orbitala dela ezartzen dugu. Gainera, kalkulu hauekin $\text{Ni}(d)$ - $O(p)$ loturaren arteko interakzioa C1 eta C2 egoeretako aldatu egiten dela ezartzen dugu, ondorioz, apantailamendu efektuak aldatuz. Sustratua gehi kate sisteman U ren balioa are gehiago txikitzen da balioak $U \lesssim 2$ eV izan arte kate guztietan, MnO_2 a izan ezik non $U \sim 3.8$ eV den. J ren balioak ez du aldaketa nabaririk sustratuta ezartzean. Sustratua ezartzean, FeO_2 kateak du aldaketa handiena $U \sim 1.4$ eV izatera bihurtzen da, aldaketa bortitz hau isolatzailetik metaliko izatera pasatzearen ondorioa deritzogu. Horretaz aparte, sustratuak karga katera transferitzeko gai da orbitalen egoerak aldatuz eta ondorioz spin egoera spin egoera aldatzen da, adib., FeO_2 katean $S = 2$ -tik $S = 3/2$ -ra. Honek $X(d)$ orbitalaren eta $O(p)$ arteko interakzioa aldatzen du,

kalkuluek baieztatzen dute apantailamenturako beste efektu bat izan ahal dela. Gainera, bi efektu hauek ezin dira bi termino desberdinetan banatu, beraz ezin dezakegu bakoitzaren ekarpena kalkulatu.

5. atalean, trantsizio metal-molekula organiko kate polimerikoetan zentratuko gara. Kate hauetan Co eta Cr atomoak 2,5-diamino-1,4-benzoquinonediimina (QDI) molekularen bidez lotzen dira. Hasieran, U -ren balio desberdinetarako geometria erlaxatzen dugu. $4 \leq U \leq 5$ arteko kalkulek, kate hauetan Co atomoak bi spin egoera desberdin izan ahal duela frogatzen dute, $S = 1/2$ eta $S = 3/2$, bi egoeretan atomoen distantzia desberdina izanik. Gainera, $U = 4$ eV kasuan, oinarrizko egoera $S = 1/2$ den bitartean $U = 5$ ezartzean $S = 3/2$ egoera pasatzen da oinarrizko egoera izatera. Aldiz, CrQDI katean soilik $S = 2$ egoera lortzen dugu Cr atomorako. Metaegoeren azterketa bat burutzen dugu orbitalen okupazio kontrolaren metodoa erabiliz. Co atomoarentzat metaegoera bat lortzen du $S = 3/2$ -rekin, oinarrizko egoeratik 72 meV-ra. Co $S = 1/2$ eta Cr atomoan lortutako metaegoerak oinarrizko egoeratik energikoki oso urrun daude, beraz ez ditugu kontutan hartzen. Anisotropia magnetikoaren energia kalkuluek, CoQDI ardatz leuna katearen planoan baina berekiko perpendikularra ezartzen dute $S = 3/2$ egoeretan, eta kateraren norabiden $S = 1/2$ egoerarentzat. CrQDI katean ardatz leuna katearen planoaren normalaren norabidean dago. Truke elkarrekintzaren kalkuluek, CoQDI kateko $S = 3/2$ egoerek AFM egitura lehenesten dutela frogatzen dute, aldiz $S = 1/2$ -ko egoerak FM egitura, CrQDI kateak AFM egitura erakusten du. Emaitza hauek Pavel Jelineken taldeak XMCD eta XLD esperimentuetan neurtutako emaitzekin bat egiten dute. Soilik CrQDI truke elkarrekintzan neurtutako seinaleak AFM egitura ahula neurtzen du eta gure kasuan AFM egitura egonkorra lortzen dugu. Truke elkarrekintzaren desberdintasuna azaltzeko asmoz katean zentzu fisikoa duten aldaketak egiten saiatu gara, adib.: U ren balioa aldatu, spinen egitura kolinealak ez diren egiturak ezarri, katearen geometriari distortzioak eragin etab. Hala ere, aldaketa hauek ez dute truke elkarrekintzan ia eraginik, soilik U ren aldaketek txikitzen du truke elkarrekintza, baina ez esperimentua azaltzeko bezain beste.

Azkenik, **6. atalean**, Tesi honetan burutu dugun ikerkuntzaren ondorio nagusiak aurkezten ditugu.

Chapter 1

Introduction

Pretentious quotations are the
surest road to tedium

H.G. and F.G. Fowler

The main purpose of this Thesis is to perform a theoretical analysis of the magnetism and electronic correlation on different spin chain system¹. Though simple in their structure, they show intriguing magnetic properties due to their low dimensionality. Synthesizing one-dimensional systems on different substrates presents a significant challenge to realize experimentally, and to do any measurement is a great task. Therefore, theoretical calculations are essential to find ideal candidates to be able to grow experimentally and also predict the magnetism in these systems. Our work's first aim is to give insights into the interplay between chains and the substrate where the chain is grown. Studying two different systems, the chain with and without the substrate. Depending on the interaction between substrate and chain, the magnetic atom electron occupancy can be entirely modified and interaction between the electrons affected, thus, modifying the magnetic properties of the system. Our second goal is to analyze the consequences when the theoretical analysis is capable to converge to excited states apart from the minimum energetic ground state. We will study the change in the magnetic properties when the different states are set in the magnetic atoms.

¹We refer as spin chains to chains where spin-spin interactions between magnetic atoms take place [1]

The discovery of magnetic materials and their utility has been a key element in the development of human history. For instance, without the magnetic compass pointing to the North pole² navigation would have been inconceivable. Since the late 20th century, magnetic materials have become a part of our daily life, from the most common use as magnets sticking to the fridge to data storage devices in computers. These advances have been only possible after deeply understanding the origin of magnetism. Historically speaking, the first clear reference to magnetism was given by Thales of Miletus around the 6th century BC with lodestones, a magnetic mineral of Fe_3O_4 . The understanding of magnetism took a huge step forward in the 19th century with the experiments of Oersted and Faraday, which linked electric currents and the magnetic field. Later generalized by Maxwell's equations, giving rise to the joint theory of electromagnetism. These equations could describe the magnetic and electric fields, but the description of the source of magnetism in materials was still lacking. In the 20th century, the advent of Quantum Mechanics and a better understanding of the structure of the atom brought a great revolution in the research of magnetic materials. The Stern-Gerlach experiment showed that a neutral beam of Ag atoms under a nonuniform magnetic field separated into two spots, becoming the first experimental signature of the electron's spin [3]. Uhlenbeck and Goudsmit were the first to propose the hypothesis of the "spinning" electron³ [4]. In their hypothesis, they proposed a magnetic moment proportional to the angular momentum \mathbf{S} . Pauli had already proposed that another quantum number should be needed to understand the electronic structure, hence, he further developed the idea of the electronic spin, setting that the spin operator \mathbf{S} is an orbital moment associated with the quantum number m_S . As the orbital momentum \mathbf{L} , \mathbf{S} can be associated with a vector $\mathbf{S} = (S_x, S_y, S_z)$, its component values are given by the three Pauli matrices. In 1925, Pauli proposed his well-known exclusion principle for the electrons, stating that particles with $S = 1/2$, can not be in the same state, i.e., have equal quantum numbers⁴. The formal derivation of the half-integer spin into theory was made by P. Dirac with the inclusion of relativity in Schrödinger's equation resulting in the so-called Dirac's equation [5, 6]. The spin appears automatically in Dirac's equation, setting the spin as a quantum property of particles without any equivalent characteristic in classical physics. Considering all this theory, the total magnetic moment has two contributions from

²In fact, for the last 780.000 years, it is the magnetic South pole [2] due to the inversion of the magnetic field of the Earth.

³Note, that even if we mentioned "spinning" electron, this is not true as in our theory we treat the electron as a point-like particle.

⁴The generalized exclusion principle for the fermions, i.e., particles with half-integer spin was stated in 1940.

the different angular momenta: orbital (μ^L) and spin (μ^S), the latter being twice the first one because of the gyromagnetic factor. The spin magnetic moment of the atoms originates from the unpaired electron spins resulting in a total net spin different from zero. This implies that all atoms that have unpaired orbitals should show magnetism.

In contrast to the atomic model, where atoms with an odd number of electrons should show a magnetic moment, band theory predicts that only a few materials are magnetic in bulk. In general, magnetism appears in materials that contain transition metal atoms and rare-earth elements [7, 8, 9]. Magnetism in solids originates from the competition between the motion, i.e., the kinetic energy, and the exchange interaction between electrons resulting from the Coulomb interaction. While Coulomb interaction favors the electron localization and thus the magnetic moment, while kinetic energy favors the itinerancy of electrons. $3d$ transition metals are a good example of the interplay of these two effects, as d electrons are localized within the magnetic atoms but still can form dispersive bands [10]. In magnetic materials, the atomic spin magnetic momenta can be aligned in different ways (see Fig. 1.1), such as, parallel (ferromagnetic) [11] and antiparallel (antiferromagnetic) [12], ferrimagnetic or forming complex non-collinear structures [6]. These spin orderings are possible by the exchange interaction proposed by Heisenberg: $\mathbf{S}_i \cdot \mathbf{S}_j$, where \mathbf{S}_i is the spin vector at atom i . The exchange interaction counteracts thermal disorder effects. There is a critical temperature where all spin order vanishes, namely the Curie temperature for ferromagnets and the Néel temperature for antiferromagnetic materials. Above these temperatures, the magnetic material are randomly oriented, resulting in a zero net magnetic moment, i.e., these materials are paramagnetic. The stability of the magnetic moment is also related to the magnetocrystalline anisotropy, i.e., the preference of the spin to be aligned with a specific crystallographic⁵ direction, due to the spin-orbit coupling (SOC). The higher the magnetocrystalline anisotropy the harder to change the spin orientation, e.g., using external magnetic fields.

A well-known use of magnets is as data storage, where data is stored in magnetic domains, i.e., regions in magnetic materials where the atoms have a common magnetization direction, using as support, for example, magnetic tapes and hard disk drives [13]. These devices are made of thin films of ferromagnetic materials, such as Co-based alloys, deposited on a non-magnetic substrate, e.g., aluminum, glass or ceramic. The different magnetization alignments in the domains set the 0

⁵The preferred direction is known as easy-axis.

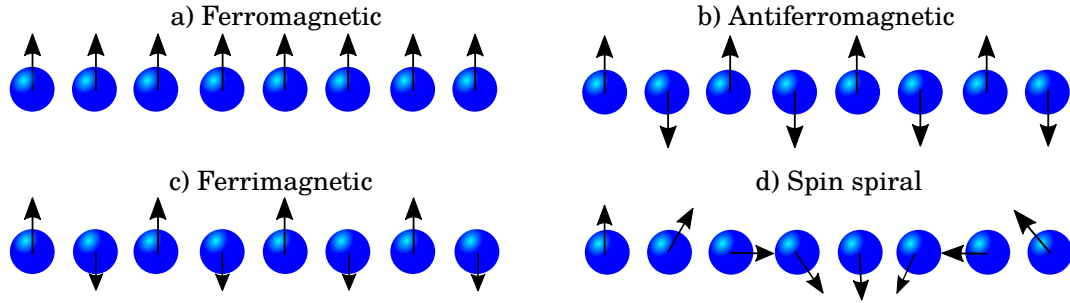


Figure 1.1: Examples of spin orders in a chain. (a) Ferromagnetic, (b) antiferromagnetic, and (c) ferrimagnetic orders are collinear, while the (d) spin spiral is a non-collinear order.

or 1 bit encoding in the read-write processes. The amount of information that can be stored depends on the magnetic domain density. Nowadays, hard disk drives can reach a memory density of 10^{16} bit/ m^2 , where each bit spatial extent is roughly 100 nm^2 [14]. With the rapid progress of information technology, the data that needs to be stored in these devices has grown exponentially in the last years [15]. Magnetic domains need to be reduced to allow larger data storage. The size of the domains can be controlled by manipulating the walls that separate each other. The wall length is given by the competition between the exchange coupling and magnetic anisotropy [16], where the exchange favors larger walls and anisotropy shorter ones. As the size of the magnetic domains is reduced, thermal effects can drive to random magnetization flips, the so-called superparamagnetic limit, which may lead to the loss of the stored information [17]. Low-dimensional systems can be considered, from two-dimensional systems (2D) up to the 0D limit of the magnet: the atom. Our work is focused on one-dimensional (1D) systems. 1D chains comprise a diverse family of different structures, such as, atomic chains (a linear array of atoms) or complexes such as metal-oxides or metal-organic molecule chains. In this family, we also include "quasi-one-dimensional" nanowires (or nanoribbons), wires with some lateral extension, where 1D quantum effects determine their properties [18, 19] to 3D structures that effectively can be treated as arrays of stacked 1D chains [20]. Specifically, in this Thesis we will work with chains where the transition metal atoms are linked with O atoms (transition metal-oxide, TMO) chains [21, 22, 23] and with organic molecule ligands, forming metal-organic chains [24, 25, 26, 27, 28].

Along with the reduction of dimensionality, the many-body interactions become more relevant than in the bulk state. Due to the lower coordination, Coulomb interaction screening is reduced compared to that of a bulk system, thus, enhancing the spin-spin exchange interactions. Therefore, there exists a possibility of mag-

netism in otherwise non-magnetic materials, for example, *sp* elements such as Al nanowires [29]. In low dimensional systems ($d \leq 2$), the Mermin-Wagner theorem forbids long-range spin ordering at any non-zero temperature [30], unless magnetic anisotropy is present. The lower dimension favors larger spin and orbital moments, enhancing the magnetic anisotropy [9]. The 1D chains can be used for electronic purposes [31], such as logic gates [32], diodes [33] or transistors [34, 35]. But the main interest in one-dimensional chains comes from their intriguing magnetic properties. Symmetry reduction in chains (e.g., lack of inversion symmetry) and the Heisenberg exchange interaction makes different magnetic collinear or non-collinear order possible. The loss of centrosymmetry combined with SOC allows the appearance of other interactions such as the antisymmetric (Dzyaloshinskii-Moriya) exchange, leading to non-collinear chiral spin orderings. This type of interaction allows the existence of exotic magnetic textures, such as, skyrmions in nanowires [36] and spin-orbit torque [37], which make them fundamental for state-of-the-art technological devices based on spintronics [38], i.e., devices that consider the spin degree-of-freedom [39, 40, 41]. Low dimensional systems can help reducing the size of devices. However, they have a drawback: their critical temperature is lower than that of 3D materials [9].

Synthesizing one-dimensional systems is challenging for experimentalists. Among the used techniques are the controlled self-assembly, e.g., in stepped surfaces [42] [43, 44, 45] and atomic manipulation [46] by STM [47]. The first experimental evidence of magnetic order in atomic chains was reported in 2002 by Gambardella *et al.* [48], who found ferromagnetism in monoatomic Co chains grown along the step-edges of Pt(997) substrate. Experimentally, the geometry can be characterized at the atomic scale by means of low-energy electron diffraction (LEED) [49] and scanning electron microscopy (STM) [50]. The electronic structure can be studied using scanning electron spectroscopy (STS) [51], inelastic electron tunneling spectroscopy (IETS) [52] and angle-resolved photoemission spectroscopy (ARPES) [53]. Magnetic characterization can be performed by X-ray magnetic circular dichroism (XMCD) and linear dichroism (XLD) [54, 55] also using IETS [56] and spin-polarized STS techniques [57, 58, 59]. The improvement of the experimental techniques, such as, the STM allows the characterization of the spin of individual atoms, and in some cases, the displacement and transfer of specific atoms [46, 1], this allows to a spin-by-spin control and characterization of the magnetic chains [60].

Early theoretical studies of spin chains include Heisenberg's work on ferromagnetic chains [11], Bethe's research on antiferromagnetism [61], the study of

spin-wave excitations by des Cloizeaux [62, 63] and many others [64, 9]. Later on, the development of *ab initio* calculation methods, such as, density functional theory (DFT) allowed to perform calculations without empirical parameters but still with an adequate balance between accuracy and computation cost. The spin-polarized DFT allows us to calculate the system's total energy for different spin alignments. This allows to obtain the magnetic ground state configuration and thus, the exchange coupling constant \mathcal{J} between these spin orderings. The magnetic anisotropic energy (MAE) of each system can be obtained by the difference in the total energy for different magnetization orientations in DFT+SOC calculations. MAE is around $\sim 1 - 10$ meV in low dimensional systems [9]. Thus, the total energy convergence needs to be obtained with a large precision. Different approaches have been considered to ease the evaluation of SOC effects in the systems. In our work, we use two different methods: one where SOC is considered self-consistently and the other is the force theorem [65, 66]. In the latter one, SOC effects are evaluated in a converged spin-polarized electron density without any further density updates; hence, a computationally less demanding calculation is made, compared to the former one. In the self-consistent calculation, a more accurate effect of SOC is obtained, as the electron density is allowed to relax at the cost of increasing the computational cost.

DFT is based on a one-electron picture, hence, it can not always describe the properties of strongly correlated materials. In these materials, the electron-electron interaction needs to be considered in the calculation. This problem becomes evident in $3d$ transition metal atoms, where the d shell is strongly localized, particularly, in low-dimensional systems. This limitation may result in the erroneous prediction of a metallic system instead of insulating [67]. To improve the description of the localized electrons, different corrections have been implemented into DFT, e.g., self-interaction correction [68, 69, 70] and the DFT+ U correction. In our work, we use the latter method where a Hubbard-like term [71] is included in the Hamiltonian to describe the interaction between the localized electrons. Another limitation when DFT is used to compute the ground-state properties is that we rely on that the converged state is the ground state. If the energy minimization procedure was exact, the resulting state would always be the ground state. However, the numerical procedure is not perfect, it can find configurations with sufficient energetic barrier that the energy minimization can not surpass, hindering the true ground state [72, 73]. Therefore, methods that can consider these occupation variation need to be applied to ensure the ground state.

The structure of the Thesis is as follows:

In **Chapter 2**, we describe the theoretical framework used in our work. We begin with a brief introduction to the basic equations in Solid State Physics. Next, the DFT background is described along with the DFT+ U correction scheme and the occupancy matrix control (OMC) method used to find metastable configurations. Next, we present the two methods used to evaluate the MAE: the self-consistent method and the force theorem approach. Finally, we describe the constrained random phase approximation (cRPA) method, used to calculate the U (intraorbital) and J (interorbital) interaction parameters needed in the DFT+ U calculations. Together, a brief introduction to maximally localized Wannier functions (MLWF) is given.

In **Chapters 3** and **4**, we present the results for our research on TMO chains, XO_2 where $X = Ni, Co, Fe$ and Mn [23, 74]. In **Chapter 3**, we show the obtained results for the magnetic properties of free-standing TMO chains. We calculate the ground state dependence on U , along with the Heisenberg coupling and MAE.

Chapter 4 explores the screened Coulomb interaction in the d shell of the X atom in the TMO chains. Using cRPA, we compute U and J for the isolated and supported chains on an Ir(100) substrate. We study the variation of U and J with the X atom d -orbital configuration for both cases.

Chapter 5 is devoted to the analysis of the metal-organic chains formed by Co and Cr atoms coordinated with 2,5-diamino-1,4-benzoquinonediimine (QDI) ligands [75]. In particular, we analyze the existence of metastable states in the TM atoms and their effects in the magnetic features. Our theoretical results on the electronic structure and the magnetic properties help to interpret the experimental measurements of XMCD and XLD made by the group of Prof. Pavel Jelinek from the Institute of Physics in Prague.

Finally, in **Chapter 6**, we present the main conclusions of the investigation performed during the Thesis.

Chapter 2

Theoretical methods

That is brand-new information!

Phoebe Buffay, *Friends*

In Condensed Matter Physics, the framework to study materials at the atomic scale is quantum mechanics. In this chapter, we introduce the theoretical background of the Thesis.

2.1 The Many-Body problem in Condensed Matter Physics

An atomistic model of matter starts by N_i nuclei and N_e electrons that interact via Coulomb's law and obey the time-dependent many-body Schrödinger equation:

$$\hat{H}\Phi(\{\mathbf{r}\}, \{\mathbf{R}\}, t) = i\frac{\partial\Phi(\{\mathbf{r}\}, \{\mathbf{R}\}, t)}{\partial t}, \quad (2.1)$$

where \hat{H} is the Hamiltonian of the system, $\Phi(\{\mathbf{r}\}, \{\mathbf{R}\}, t)$ is the many-body wavefunction, $\{\mathbf{R}\} = (\mathbf{R}_1, \mathbf{R}_1, \dots, \mathbf{R}_{N_i})$ are the spatial coordinates of nuclei and $\{\mathbf{r}\} = (\mathbf{r}_1, \mathbf{r}_1, \dots, \mathbf{r}_{N_e})$ are the electronic spatial coordinates. t is the time. In the case of the stationary problem, we can separate the spatial degrees of freedom from the time:

$$\hat{H}\Psi(\{\mathbf{r}\}, \{\mathbf{R}\}) = E\Psi(\{\mathbf{r}\}, \{\mathbf{R}\}), \quad (2.2)$$

being E the total energy of the stationary system and Ψ the time-independent wave function. The Hamiltonian can be split into the kinetic energy of the ions and electrons and the interaction terms between them. For a system under no external fields, the non-relativistic Hamiltonian in atomic units¹ can be written:

$$\begin{aligned} \hat{H} = \hat{T}_i + \hat{T}_e + \hat{V}_{ii} + \hat{V}_{ie} + \hat{V}_{ee} = & \sum_i^{N_i} \frac{\mathbf{P}_i^2}{2M_i} + \sum_n^{N_e} \frac{\mathbf{p}_n^2}{2} + \frac{1}{2} \sum_{i \neq j}^{N_i} \frac{Z_i Z_j}{|\mathbf{R}_i - \mathbf{R}_j|} \\ & - \sum_i^{N_i} \sum_n^{N_e} \frac{Z_i}{|\mathbf{R}_i - \mathbf{r}_n|} + \frac{1}{2} \sum_{n \neq n'}^{N_e} \frac{1}{|\mathbf{r}_{n'} - \mathbf{r}_n|}, \end{aligned} \quad (2.3)$$

where \hat{T}_i and \hat{T}_e are the kinetic energy operators of the ions and electrons, respectively, and \hat{V}_{ii} , \hat{V}_{ie} and \hat{V}_{ee} the Coulomb interaction terms between the ions, ion-electron and electrons, respectively. The subindices i and j run over the ion nuclei and n and n' over the electrons. \mathbf{P}_i and \mathbf{p}_n are ionic and electronic momentum operators, respectively. M_i is the nuclear mass and Z_i the nucleus charge.

Solving Eq. (2.2) allows us to obtain the exact wavefunction Ψ and, therefore, all information regarding the system. However, we face an equation system with $3(N_i + N_e)$ spatial degrees of freedom and Coulomb interactions make it impossible to separate the many-body problem into a single-particle one. Furthermore, if the goal is to obtain solutions for macroscopic behavior, we deal with an enormous number, $\sim 6 \times 10^{23}$, of atoms. Therefore, an exact solution is unfeasible and approximations are required from the beginning.

The Born-Oppenheimer approximation

In the Born and Oppenheimer approximation, the full many-body wavefunction is split into two different functions [76] as follows:

$$\Psi(\{\mathbf{r}\}, \{\mathbf{R}\}) = \sum_n \chi_n(\{\mathbf{R}\}) \psi_n(\{\mathbf{r}\}; \{\mathbf{R}\}), \quad (2.4)$$

where χ_n and ψ_n stand for the set of nuclei and electron wavefunctions, and n runs through the nuclei states. The Born-Oppenheimer approximation is based on the huge difference of masses between the electrons and nuclei (for instance, in the Hydrogen atom the mass ratio between electron and nuclei is $1/1836$). Hence, in the electron framework, nuclei move slow enough² for the electron wavefunction

¹ $m_e = e = \hbar = 1$.

²Sommerfeld's theory of conduction predicts ~ 10 Å/fs for electrons and classical harmonic theory predicts $\sim 10^{-2}$ Å/fs for ions [77].

to adapt instantaneously to their movement. Inserting Eq. (2.4) into Eq. (2.2) we build a Hamiltonian \hat{H}_e that depends only on the electronic degrees of freedom and where the ion spatial coordinates $\{\mathbf{R}\}$ enter as parameters:

$$\hat{H}_e \psi_n(\{\mathbf{r}\}; \{\mathbf{R}\}) = E_n(\{\mathbf{R}\}) \psi_n(\{\mathbf{r}\}; \{\mathbf{R}\}), \quad (2.5)$$

$$\hat{H}_e = \hat{T}_e + \hat{V}_{ie} + \hat{V}_{ee} + E_{II}, \quad (2.6)$$

where the interaction between nuclei E_{II} is a constant, $\psi_n(\{\mathbf{r}\}; \{\mathbf{R}\})$ and $E_n(\{\mathbf{R}\})$ in Eq. (2.5) are obtained for a given nuclear configuration. Within the Born-Oppenheimer approximation, the system with $3(N_i + N_e)$ degrees of freedom is reduced to $3N_e$ electronic variables.

Hartree-Fock approximation

Despite the Born-Oppenheimer approximation, we still face the complexity of the many-body character of the electronic wavefunction and the electron-electron interaction. One of the proposed approaches to deal with this problem is the Hartree-Fock (HF) method [78]. The HF method is a mean-field theory where the many-body wavefunction is approximated by an independent electron wavefunction. In order to construct the approximated wavefunction³ we use the Slater determinant[79]:

$$\psi(\mathbf{r}_1, \mathbf{r}_2, \dots, \mathbf{r}_{N_e}) = \frac{1}{\sqrt{N_e!}} \begin{vmatrix} \phi_1(\mathbf{r}_1) & \phi_1(\mathbf{r}_2) & \cdots & \phi_1(\mathbf{r}_{N_e}) \\ \phi_2(\mathbf{r}_1) & \phi_2(\mathbf{r}_2) & \cdots & \phi_2(\mathbf{r}_{N_e}) \\ \vdots & \vdots & \ddots & \vdots \\ \phi_{N_e}(\mathbf{r}_1) & \phi_{N_e}(\mathbf{r}_2) & \cdots & \phi_{N_e}(\mathbf{r}_{N_e}) \end{vmatrix}, \quad (2.7)$$

where $\phi_\nu(\mathbf{r}_\mu)$ are a single-particle wavefunctions. The Slater determinant builds an antisymmetric wavefunction suitable for fermionic systems that fulfills the Pauli exclusion principle. The expectation value of the Hamiltonian Eq. (2.6) using the wavefunction of Eq. (2.7) is

³For the sake of simplicity, we remove the implicit dependence on the nuclei positions $\{\mathbf{R}\}$.

$$\begin{aligned}
\langle \hat{H}_e \rangle &= \sum_n \int d\mathbf{r} \phi_n^*(\mathbf{r}) \left[-\frac{1}{2} \nabla^2 + V_{\text{ext}} \right] \phi_n(\mathbf{r}) \\
&+ \frac{1}{2} \sum_{nn'} \int d\mathbf{r} d\mathbf{r}' \frac{|\phi_n(\mathbf{r})|^2 |\phi_{n'}(\mathbf{r}')|^2}{|\mathbf{r} - \mathbf{r}'|} \\
&- \frac{1}{2} \sum_{nn'} \int d\mathbf{r} d\mathbf{r}' \phi_n^*(\mathbf{r}) \phi_{n'}^*(\mathbf{r}') \frac{1}{|\mathbf{r} - \mathbf{r}'|} \phi_{n'}(\mathbf{r}) \phi_n(\mathbf{r}') .
\end{aligned} \tag{2.8}$$

The first term contains the kinetic energy of each particle and the external potential acting on the electrons. The second and third terms are two-body Coulomb interactions, direct and exchange terms between two electrons, the latter one arising because of the Pauli exclusion principle.

In the HF method, we use the variational principle to find the approximated ground state energy of the system. Using Lagrange multipliers, the energy is minimized while maintaining the constraint of orthogonality between one-electron wavefunctions:

$$F[\phi_n] = \langle \hat{H}_e \rangle - \sum_n \epsilon_n \left[\int d\mathbf{r} |\phi_n(\mathbf{r})|^2 - 1 \right] \tag{2.9}$$

where F is the functional to be minimized, the first term is given by Eq. (2.8) and the second term is the set of orthogonality constraints, where ϵ_n are the Lagrange multipliers. But, even if the electrons were uncorrelated, we still face a set of non-linear equations with $3N_e$ variables, which makes the problem computationally demanding.

2.2 Density Functional Theory

In Density Functional Theory (DFT), the center of interest is the electron density instead of the wavefunction. Hohenberg and Kohn stated the two principal theorems that established DFT foundations [80]:

Theorem 2.1 *The external potential $V_{\text{ext}}(\mathbf{r})$ is determined by a unique functional, aside from a constant, of the ground state electron density $n_0(\mathbf{r})$.*

Theorem 2.2 *There exists a functional of the total energy dependent on the electron density, $E[n]$, for any external potential. The exact ground state density gives the global minimum of the energy functional which is the ground state energy.*

These two theorems set the relationship between the energy and the density. However, the kinetic energy can not be directly rewritten in terms of the density and the wavefunctions within a many-body problem are still intractable.

Kohn and Sham proposed an approach that, instead of studying an interacting many-body problem, replaced it with a non-interacting one. Still, the non-interacting picture upholds the same exact ground state density of the many-body system [81]. All the information related to the many-body character of the particles is incorporated in an exchange-correlation functional term. Within the Kohn-Sham (KS) ansatz the electron density is obtained from non-interacting single-particle wavefunctions, $\psi_i^{KS}(\mathbf{r})$:

$$\rho(\mathbf{r}) = \sum_i^{N_e} |\psi_i^{KS}(\mathbf{r})|^2 . \quad (2.10)$$

The electronic energy functional can be decomposed as:

$$E^{KS}[\rho] = T^{KS}[\rho] + E_{\text{ext}}[\rho] + E_H[\rho] + E_{\text{xc}}[\rho] , \quad (2.11)$$

where the kinetic energy expressed in terms of the KS orbitals is:

$$T^{KS}[\rho] = -\frac{1}{2} \sum_i^{N_e} \int [\psi_i^{KS}(\mathbf{r})]^* \nabla^2 \psi_i^{KS}(\mathbf{r}) ; . \quad (2.12)$$

In the kinetic functional, the dependence on the density is implicit, it comes from the KS wavefunctions. Note that $T^{KS}[n]$ does not account for the correlation component of the kinetic energy as we use non-interacting KS orbitals to build the functional.

The energy due to the external potential can be expressed as:

$$E_{\text{ext}}[\rho] = \int d\mathbf{r} \rho(\mathbf{r}) V_{\text{ext}} , \quad (2.13)$$

and the Hartree energy, which corresponds to the electron-electron interaction is:

$$E_H[\rho] = \frac{1}{2} \int d\mathbf{r} d\mathbf{r}' \frac{\rho(\mathbf{r}')\rho(\mathbf{r})}{|\mathbf{r} - \mathbf{r}'|} . \quad (2.14)$$

The information regarding the many-body features is in the exchange-correlation energy. In the KS approach, the exchange-correlation energy can be approximated by a local functional of the density as:

$$E_{xc}[\rho] = \int d\mathbf{r} \rho(\mathbf{r}) \epsilon_{xc}([\rho], \mathbf{r}), \quad (2.15)$$

where $\epsilon_{xc}([\rho], \mathbf{r})$ is the exchange-correlation energy per electron. The solutions of the total energy functional are obtained by minimizing the functional 2.11 with the Lagrange multipliers method:

$$\delta \left[E^{KS} - \mu \left(\int d\mathbf{r} \rho(\mathbf{r}) - N \right) \right] = 0 \quad (2.16)$$

where the constraint is set to be a fixed number N , of electrons with the chemical potential μ acting as the multiplier.

In the KS picture the Hamiltonian is separable into single-particle KS orbitals as follows:

$$\left[-\frac{1}{2} \nabla^2 + V^{KS}(\mathbf{r}) \right] \psi_i^{KS}(\mathbf{r}) = \epsilon_i \psi_i^{KS}(\mathbf{r}), \quad (2.17)$$

where V^{KS} is the effective potential of the system:

$$V^{KS} = V_{\text{ext}} + \int d\mathbf{r}' \frac{\rho(\mathbf{r}')}{|\mathbf{r} - \mathbf{r}'|} + \frac{\delta E_{xc}}{\delta \rho(\mathbf{r})}. \quad (2.18)$$

Eq. (2.10) and Eq. (2.17) constitute the KS equations. The KS equations are solved iteratively following the procedure shown in Fig. 2.1. From an initial guess of the density, $\rho(\mathbf{r})$, we get the potential of Eq. (2.18). Introducing the obtained V^{KS} potential into the Kohn-Sham eigenvalue problem, Eq. (2.17), we obtain a set of KS orbitals. We build a new density from the latter and repeat the process until we reach a certain convergence threshold.

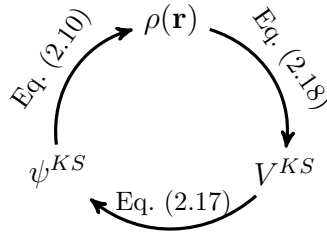


Figure 2.1: Simplified scheme of the self-consistent cycle to solve the Kohn-Sham equations.

If the exact form of the exchange-correlation functional ϵ_{xc} were known, we would be able to attain an exact description of the electronic properties of the systems. Instead, ϵ_{xc} is obtained by means of approximations. In the following section, we present the ones used in our calculations.

Exchange and correlation functional

Kohn and Sham proposed one of the most successful approaches: the local density approximation (LDA) [81]. In LDA, the exchange-correlation energy is considered a local function of the density in the limit of the uniform electron gas (UEG).

$$E_{xc}^{\text{LDA}} = \int d\mathbf{r} \rho(\mathbf{r}) \epsilon_{xc}^{\text{UEG}}(\rho(\mathbf{r})). \quad (2.19)$$

In LDA the functional ϵ^{UEG} can be separated into the exchange and correlation terms [82]:

$$\epsilon_{xc}^{\text{UEG}} = \epsilon_x^{\text{UEG}} + \epsilon_c^{\text{UEG}} \quad (2.20)$$

where the exchange term ϵ_x^{UEG} is known for a UEG system, whereas no analytic form is known for the correlation energy ϵ_c^{UEG} . Numerical methods, such as the Monte Carlo method, are used to obtain approximated values of the correlation energy. LDA is a fine approximation unless the system presents high inhomogeneities. Well-known systematic inaccuracies are present in the LDA approximation. The most remarkable is the overestimation of the binding energies and, in consequence, the underestimation of the bond-lengths [83].

The next step to improve the LDA is the construction of a semi-local approximation. In the generalized gradient approximation (GGA) a gradient of the density is included to take into account the spatial variations of the density.

$$E_{xc}^{\text{GGA}} = \int d\mathbf{r} \rho(\mathbf{r}) \epsilon[\rho(\mathbf{r}), |\nabla\rho(\mathbf{r})|]. \quad (2.21)$$

In the GGA functional, E_{xc} has the general form:

$$E_{xc}^{\text{GGA}} = \int d\mathbf{r} \rho(\mathbf{r}) \epsilon^{\text{UEG}}[n(\mathbf{r})] F_{xc}(\rho(\mathbf{r}), |\nabla\rho(\mathbf{r})|), \quad (2.22)$$

where $F_{xc}(\rho(\mathbf{r}), |\nabla\rho(\mathbf{r})|)$ is the so-called enhancement function, which holds information about the non-locality of the density. In our calculations, we have used the parametrization given by Perdew, Burke and Ernzerhof (PBE) [84].

Another way to improve the exchange-correlation functional is to combine the Hartree-Fock (HF) exchange and the LDA or GGA exchange-correlation functionals. The hybrid functionals consider a mixing of both [85]:

$$E_{xc}^{\text{Hybrid}} = (1 - a) E_{xc}^{\text{HF}} + a E_{xc}^{\text{LDA/GGA}}, \quad (2.23)$$

where the parameter a is a mixing factor $0 < a < 1$. In our calculations, we use the Heyd–Scuseria–Ernzerhof hybrid functional [86], in this hybrid functional the exchange term is divided into short and long range part, depending on a parameter μ , where only the short-range term is mixed with the HF. Specifically, we use the HSE06 formulation where $a = 3/4$ and $\mu = 0.2$ are set [87].

Spin in DFT

Hohenberg and Kohn developed DFT theory for spinless systems, while von Barth and Hedin extended it to include spin-polarized systems [88]. Spin-polarized DFT uses spinor wavefunctions to build a density matrix. The density matrix, $\hat{\rho}$, can be separated into a scalar density ρ and vectorial \mathbf{m} density:

$$\hat{\rho}(\mathbf{r}) = \psi^{\alpha*} \mathbf{1} \psi^\beta + \psi^{\alpha*} \boldsymbol{\sigma}^{\alpha\beta} \psi^\beta = \frac{1}{2} \begin{pmatrix} \rho(\mathbf{r}) + m_z(\mathbf{r}) & m_x(\mathbf{r}) - im_y(\mathbf{r}) \\ m_x(\mathbf{r}) + im_y(\mathbf{r}) & \rho(\mathbf{r}) - m_z(\mathbf{r}) \end{pmatrix} \quad (2.24)$$

where ψ^α is the wavefunction with spin α , $\beta = \uparrow, \downarrow$, $\mathbf{1}$ is the 2×2 unitary matrix and $\boldsymbol{\sigma} = (\sigma_x, \sigma_y, \sigma_z)$ are the Pauli matrices. The density matrix elements are given by: $\rho_{\alpha\beta} = \psi^{\alpha*} \psi^\beta$. In the case of no external magnetic field coupling to the spin the resulting Schrödinger-like equation is:

$$\left[\left(-\frac{1}{2} \nabla^2 + \sum_{\alpha} \int d\mathbf{r}' \frac{\rho^{\alpha\alpha}(\mathbf{r}')}{|\mathbf{r} - \mathbf{r}'|} \right) \mathbf{1} + V_{\text{ext}}^{\alpha\beta}(\mathbf{r}) + \frac{\delta E_{xc}[\rho^{\alpha\beta}(\mathbf{r})]}{\delta \rho^{\alpha\beta}(\mathbf{r})} \right] \begin{pmatrix} \psi^\uparrow \\ \psi^\downarrow \end{pmatrix} = \epsilon_i \begin{pmatrix} \psi^\uparrow \\ \psi^\downarrow \end{pmatrix} \quad (2.25)$$

Analogously to the density, the exchange-correlation functional is spin dependent. Eq. (2.25) is the general case that describes noncollinear spin textures. Considering that all atoms align their spins in the z -axis direction, such as in the collinear case, e.g. antiferromagnetic, ferromagnetic or ferrimagnetic, the potential matrix becomes diagonal, resulting in two decoupled equations [89]:

$$\left[-\frac{1}{2} \nabla^2 + \int d\mathbf{r}' \frac{\rho^{\uparrow\uparrow}(\mathbf{r}')}{|\mathbf{r} - \mathbf{r}'|} + V_{\text{ext}}^{\uparrow\uparrow} + v_{xc}^{\uparrow\uparrow} \right] \psi^\uparrow = \epsilon_i^\uparrow \psi^\uparrow \quad (2.26)$$

$$\left[-\frac{1}{2} \nabla^2 + \int d\mathbf{r}' \frac{\rho^{\downarrow\downarrow}(\mathbf{r}')}{|\mathbf{r} - \mathbf{r}'|} + V_{\text{ext}}^{\downarrow\downarrow} + v_{xc}^{\downarrow\downarrow} \right] \psi^\downarrow = \epsilon_i^\downarrow \psi^\downarrow \quad (2.27)$$

where $v_{xc}^{\uparrow\uparrow, \downarrow\downarrow} = \frac{\delta E[\rho^{\uparrow\uparrow, \downarrow\downarrow}]}{\delta \rho^{\uparrow\uparrow, \downarrow\downarrow}}$.

DFT in strongly correlated systems: DFT+ U method

LDA and GGA functionals consider an orbital-independent potential. Both functionals have been successful to obtain material properties but they can fail when strong electron interactions are present in the systems. The latter systems are usually compounds with transition metal, or rare-earth, atoms with partially filled d or f orbitals [90]. If the strong correlations are not taken into account, LDA- and GGA-based calculations can miss their localized character, resulting sometimes in an itinerant electron behavior and a metallic state instead of insulating [67]. This latter problem is evident in Mott insulators[91], where non-interacting band theory predicts a metallic state, but experiments show an insulating behavior, e.g., in V_2O_3 and CoO[92]. Several magnetic properties depend strongly on the value of the interaction between the electrons, such as, magnetic moment, magnetic exchange coupling, etc. [93, 94, 10].

In order to obtain the correct ground-state properties in strongly correlated systems, we need to properly take into account the Coulomb intratomic interactions between the localized states. A way to do so is to combine DFT and the Hubbard Hamiltonian, which constitutes the so-called DFT+ U scheme. The Hamiltonian of the system is separated into two terms: one where the orbital-independent one-electron potential is maintained and another one where we include a Hubbard-like term [71], aimed at describing the screened Coulomb interaction⁴ [95, 96] between electrons in the correlated orbitals (d orbital in this work). The DFT+ U energy functional[97] is defined as follows:

$$E^{\text{DFT}+U}[\rho^\sigma, n_l^\sigma] = E^{\text{DFT}}[\rho^\sigma] + E^{ee}[n_l^\sigma] - E^{\text{DC}}[n_l^\sigma], \quad (2.28)$$

where $E^{\text{DFT}}[\rho^\sigma]$ is the functional with the LDA or GGA exchange-correlation. Considering collinear spins, ρ^σ is the spin density with spin $\sigma = \uparrow, \downarrow$. The second term is the multiorbital Hubbard-like functional dependent on the orbital occupation matrix n_l^σ , where l is the orbital shell number, and the last term is the double counting (DC) term. In Eq. (2.28) the DC term is introduced to eliminate the electron-electron interaction of the localized states that is already taken into account in E^{DFT} . Next, we describe details about the two different forms of the Hubbard term that have been used in the manuscript. The first one is proposed in Ref. [98]⁵:

⁴From now on, when we write *screening*, we refer to the screening of the localized d states. In the case of the screening of the full system, W , we will explicitly write *fully* screened.

⁵We adopt Dirac's notation to account for the Coulomb matrix elements.

$$E^{ee}[n] = \frac{1}{2} \sum_{\substack{\sigma\sigma' \\ m_1, m_2 \\ m_3, m_4}} \hat{n}_{m_1 m_2}^\sigma (\langle m_1 m_3 | V_{ee} | m_2 m_4 \rangle - \langle m_1 m_3 | V_{ee} | m_4 m_2 \rangle \delta_{\sigma\sigma'}) \hat{n}_{m_3 m_4}^{\sigma'} \quad (2.29)$$

where $\hat{n}_{m_1 m_2}^\sigma$ are the matrix elements of the occupation matrix, m_i are the orbitals of the shell l , running for $m_i = -l, \dots, l$, and V^{ee} is the screened Coulomb interaction. Different flavours to account for DC term exist, such as the around mean-field approximation [95] (AMF) and the fully-localized limit [97] (FLL). Results may depend on the chosen DC term. In the FLL, the states that are more than half-occupied are lowered in energy while in the AMF case the states with an occupation higher than the average are lowered in energy [99, 100]. In our calculations, we use the DFT+ U within the fully localized limit DC term [101]:

$$E^{\text{DC}}[n] = \frac{U}{2} N(N-1) - \frac{J}{2} \sum_{\sigma} N^{\sigma} (N^{\sigma} - 1) , \quad (2.30)$$

where $N^{\sigma} = \text{Tr}(\hat{n}^{\sigma})$ is the trace of the \hat{n}^{σ} matrix, and $N = N^{\uparrow} + N^{\downarrow}$. The U and J parameters are the screened electron interaction and the exchange parameters, obtained from the screened Coulomb interaction as follows:

$$U = \frac{1}{2l+1} \sum_{m_1 m_3} \langle m_1 m_3 | V^{ee} | m_1 m_3 \rangle \quad (2.31)$$

$$J = U - \frac{1}{2l(2l+1)} \sum_{m_1 m_3} (\langle m_1 m_3 | V^{ee} | m_1, m_3 \rangle - \langle m_1 m_3 | V^{ee} | m_3 m_1 \rangle) . \quad (2.32)$$

The second one is a simplified version of Eq. (2.29), derived by Dudarev *et al.* [102] considering the Hamiltonian given in [96]:

$$E^{ee}[n] = \frac{U}{2} \sum_{mm'\sigma} n_m^{\sigma} n_{m'}^{-\sigma} + \frac{U-J}{2} \sum_{m \neq m' \sigma} n_m^{\sigma} n_{m'}^{\sigma} . \quad (2.33)$$

where n_m is the occupation number of the m orbital, i.e. $n_m = \hat{n}_{mm}$.

In order to take into account the DC term, we evaluate the previous equation in the limit of integer values of the occupation matrix and subtract it from the DFT energy. The resulting DFT+ U functional in Dudarev's approach is expressed as:

$$E_{\text{Dudarev}}^{\text{DFT}+U}[\rho^{\sigma}, n] = E^{\text{DFT}}[\rho^{\sigma}] + \frac{U-J}{2} \sum_{\sigma} \left(\sum_{m_1} \hat{n}_{m_1 m_1}^{\sigma} - \sum_{m_1 m_2} \hat{n}_{m_1 m_2}^{\sigma} \hat{n}_{m_2 m_1}^{\sigma} \right) . \quad (2.34)$$

where, the second term, proportional to $U - J$, acts as a penalty function on the DFT energy, driving the system towards an integer on-site occupancy matrix, $n_m^\sigma m$.

In the DFT+ U , the U correction scheme is only applied to states with the orbital character of the localized orbital and the total energy will depend on U and J . This means that total energies resulting from two calculations that use different U and J values cannot be compared.

Bloch's theorem

3D perfect crystals are formed by repeated units with lattice vectors \mathbf{R}_1 , \mathbf{R}_2 and \mathbf{R}_3 . Therefore, the effective potential V_{eff} acting on the electrons has to be \mathbf{R} -periodic.

$$V_{eff}(\mathbf{r} + \mathbf{R}) = V_{eff}(\mathbf{r}), \quad (2.35)$$

Bloch's theorem [103] states that the eigenfunctions ψ of a Hamiltonian with a periodic potential like Eq. (2.35) can be written as a product of a plane-wave and a function $u(\mathbf{r})$ with the periodicity of the lattice:

$$\psi_{n\mathbf{k}}(\mathbf{r}) = e^{i\mathbf{k}\cdot\mathbf{r}} u_{n\mathbf{k}}(\mathbf{r}) \quad (2.36)$$

$$u_{n\mathbf{k}}(\mathbf{r}) = u_{n\mathbf{k}}(\mathbf{r} + \mathbf{R}) \quad (2.37)$$

where \mathbf{k} is a wave vector in the first Brillouin zone of the reciprocal lattice and n is a band index resulting from different solutions for a given \mathbf{k} . Because of Eq. (2.36), we can expand the wavefunctions using a plane-wave basis:

$$\psi_{n\mathbf{k}}(\mathbf{r}) = \frac{1}{\sqrt{V}} \sum_{\mathbf{G}} c_{n\mathbf{k}}(\mathbf{G}) e^{i(\mathbf{k}+\mathbf{G})\cdot\mathbf{r}} \quad (2.38)$$

where V is the volume of the cell, $c_{n\mathbf{k}}(\mathbf{G})$ the coefficients and \mathbf{G} are reciprocal lattice vectors.

Projector Augmented Wave (PAW)

In order to solve the KS equations numerically, different methods have been implemented in software codes. In our calculations, we use two different codes: VASP (*Vienna Ab-Initio Software Package*) and FLEUR. Both codes calculate the electronic structure and ground-state properties of the systems. In this section, we will describe briefly the projector augmented wave (PAW) method [104] used in VASP. For a detailed description, the reader is referred to ref. [105].

The PAW method generalizes the pseudopotentials and linearized augmented plane-wave techniques. The valence electrons are responsible for most physical and chemical properties and therefore enter into the KS equations and construction of the density. The valence electrons wavefunctions show a rapid oscillatory behavior near the nuclei, making it necessary to use a large number of plane waves to describe them correctly. To overcome this problem, the potential acting on the core electrons is replaced by a pseudopotential inside a spherical region, where valence electrons are described by smoothed pseudowavefunctions. In the PAW method, the transformation from the pseudowavefunction to the true one-electron wavefunction $\tilde{\psi}_{n\mathbf{k}}$ is done by:

$$\psi_{n\mathbf{k}} = (1 + \mathcal{L}) \tilde{\psi}_{n\mathbf{k}} \quad (2.39)$$

where \mathcal{L} is the linear transformation function acting inside the PAW sphere, which maps the pseudowavefunction $\tilde{\psi}_{n\mathbf{k}}$ to the true wavefunction. Inside this region the constructed pseudowavefunction is a mathematical tool that does not resemble the true all-electron wavefunction. Outside, the wavefunction $\tilde{\psi}_{n\mathbf{k}}$ matches the true all-electron wavefunctions. In VASP, the $\tilde{\psi}_{n\mathbf{k}}$ is expanded in a plane-wave basis.

Full Potential Linearized Augmented Plane Wave (FLAPW)

The FLEUR code is an implementation of the full-potential linearized augmented plane wave (FLAPW) method [106]. We give here the basic details of FLAPW. For a complete description we refer to the review of S. Blügel and G. Bihlmayer Ref. [107].

In the LAPW method, the space is divided into non-overlapping muffin-tin (MT) spheres centered at each atom and the interstitial region (IR) between them. The core electrons are localized inside the MT region, while the valence electrons spread over the MT and IR. In the MT region, the wavefunctions are described by the spherical harmonics times a radial function, while in the IR a plane-wave basis is used. The radial function is the solution of the radial Schrödinger equation. To avoid the dependence on the energy E parameter, in LAPW, a linear approximation in E of the radial function is made, that depends on an orbital (l) dependent parameter E_l . Therefore, the valence electrons wavefunctions are:

$$\psi_{\mathbf{kG}}(\mathbf{r}) = \begin{cases} \frac{1}{\sqrt{V}} e^{i(\mathbf{k}+\mathbf{G})\cdot\mathbf{r}}, & \text{if } \mathbf{r} \in \text{IR} \\ \sum_{lm} (a_{\mathbf{kG}}^{lm} u(r; E_L) + b_{\mathbf{kG}}^{lm} \dot{u}(r; E_L)) Y_{lm}(\hat{\mathbf{r}}), & \text{if } \mathbf{r} \in \text{MT} \end{cases} \quad (2.40)$$

where $u(r, E_l)$ is the radial function and $\dot{u}(r, E_l)$ the first derivative with respect to the energy evaluated at the energy parameter E_l . $Y_{lm}(\hat{\mathbf{r}})$ is the spherical harmonic for angular momentum quantum number l and magnetic quantum number m . The coefficients $a_{\mathbf{kG}}^{lm}$ and $b_{\mathbf{kG}}^{lm}$ are obtained from the matching conditions of u and \dot{u} at the boundary of each MT sphere. The FLAPW approach is the combination of the potential without any shape approximations, i.e., keeping the full potential and the linearized functions of the LAPW basis.

Occupancy Matrix Control (OMC)

The DFT+ U functionals introduce an explicit orbital occupation dependence, since partial occupations are penalized in favor of integer ones (see Eq. (2.29) and Eq. (2.34)). The Hubbard corrections DC term is also occupation dependent and, moreover, not uniquely defined. In practice, this makes the KS equations self-consistency biased by the initial orbital occupation matrix. Different initial matrix \hat{n}^σ guesses may lead to metastable states instead of the true ground state configuration, as schematically shown in Fig. 2.2.

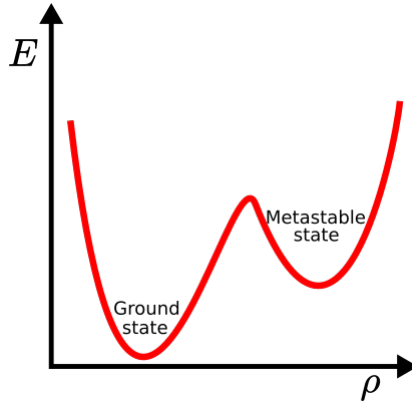


Figure 2.2: Representation of an energy curve vs the density. The local minimum is a metastable state of the system while the global minimum is the true ground state.

To search for energetically accessible metastable configurations, in this work we have used the occupancy matrix control (OMC) method developed by Allen

et al. [73] and implemented in VASP via Dudarev's DFT+ U correction. In an initialization run, the occupancy matrix provided by the user is kept fixed while the wavefunctions and charge density are allowed to relax. The resulting total energy of this calculation is meaningless as we have obtained it by imposing a constraint. With the resulting charge density and wavefunctions, we run again the calculation without applying OMC. To allow further relaxation of the occupations. States within a shallow minimum of energy landscape can relax to a more stable configuration, but those configurations located in a deep minimum will remain as metastable configurations. From the resulting energies, the lowest one can correspond to the actual ground state.

2.3 Spin-Orbit Coupling (SOC)

In this section, we will discuss the spin-orbit coupling (SOC) effect in the electrons of solids. Considering a non-relativistic limit of Dirac's equation, the Schrödinger equation along with other terms can be obtained. The latter terms are the relativistic corrections to the Schrödinger equation. One of those terms is the SOC. The SOC term can be expressed as:

$$H_{\text{SOC}} = \boldsymbol{\sigma} \cdot (-\nabla V(r) \times \mathbf{p}) = -\frac{1}{r} \frac{dV(r)}{dr} \boldsymbol{\sigma} \cdot (\mathbf{r} \times \mathbf{p}) = \xi(r) \boldsymbol{\sigma} \cdot \mathbf{L}, \quad (2.41)$$

where $\boldsymbol{\sigma}$ are the Pauli spin matrices, $V(r)$ the potential, \mathbf{L} the orbital moment and $\xi(r) = -\frac{1}{r} \frac{dV(r)}{dr}$. In Eq. (2.41), a spherically symmetric potential has been assumed, as SOC is an atomic property. The function $\xi(r)$ increases for heavy atoms as the Coulomb potential is proportional to Z , nuclear number. Integrating $\xi(r)$ over the radial function for each orbital and rewriting Eq. (2.41) in terms of the spin $\mathbf{S} = \boldsymbol{\sigma}/2$:

$$H_{\text{SOC}} = \lambda \mathbf{S} \cdot \mathbf{L}, \quad (2.42)$$

where $\lambda = \langle \xi \rangle / 2$ is the radially integrated spin-orbit constant. Note that the constant differs for different orbital shells of the atom. As a consequence of this relativistic term, there are splittings in the atomic energetic states. In solids, the inclusion of SOC can split energy bands with degeneracies if their orbital symmetry allows for it [108, 109].

In DFT, to account for relativistic effects instead of solving Dirac's equation, which would require a 4-component spinor, we consider the Schrödinger equation

that includes the relativistic terms. This Hamiltonian is known as the Pauli equation (without an external magnetic field). In this method, the needed spinor is reduced to a 2-component spinor [89]:

$$H_{\text{Pauli}} = H_{\text{NR}} + H_{\text{SR}} + H_{\text{SOC}} \quad (2.43)$$

where the H_{NR} is the non-relativistic term, as in the Schrodinger equation, and H_{SR} are the scalar-relativistic terms which are the relativistic corrections without the spin term⁶.

In magnetic systems, SOC is the origin of several effects, such as the antisymmetric magnetic exchange (the so-called Dzyaloshinskii-Moriya interaction), the anomalous Hall effect and the magnetocrystalline anisotropy. This Thesis focuses on the latter effect. SOC introduces a spin-orientation dependence in the total energy of the system and, hence, the existence of a preferred magnetization direction with respect to the lattice. This energy difference between directions is the magnetocrystalline anisotropy energy (MAE), as shown in Fig. 2.3.

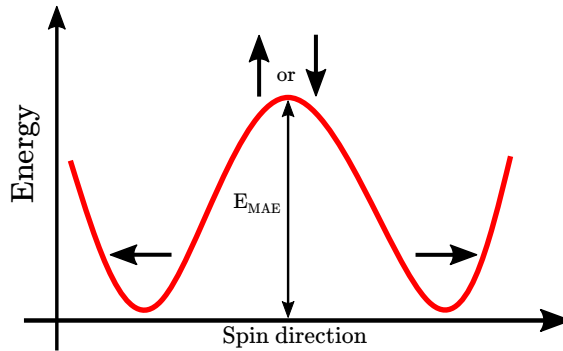


Figure 2.3: Scheme of the total energy dependence on the spin orientation and the MAE.

The MAE is usually small for fcc and bcc bulk systems, around $10 \mu\text{eV}$ or less [9], because the high symmetry reduces it to a λ^4 effect. For other bulk structures [110] and lower-dimensional systems, symmetries are reduced and higher values of the MAE are possible (of the order of λ^2 , i.e. $\sim 1 \text{ meV}$). In order to evaluate such values of the MAE a fine k-point mesh is needed, as well as, a precise Fermi level determination.

⁶The mass-velocity and Darwin terms.

To calculate the MAE, first, a scalar-relativistic self-consistent ground state is obtained [111]. In the following step, a fully-relativistic self-consistent DFT calculation is carried out, including SOC effects. The MAE is obtained by subtracting the two different total energies for two different spin orientations, \mathbf{a} , \mathbf{b} as seen in Fig. 2.3,

$$\text{MAE}_{\text{SCF}} = E_{\text{TOT}}^{\mathbf{a}} - E_{\text{TOT}}^{\mathbf{b}}. \quad (2.44)$$

As mentioned before, calculating the MAE needs a fine treatment of the SOC and a demanding convergence. Different approximations have been used to overcome this problem, such as those based on second-order perturbation theory [112, 113, 114, 54] and the force theorem (FT) method [65, 115]. In the following section, we describe the FT technique used in our work.

The non-self-consistent approach of the MAE: the force theorem

In this method, the SOC effect is added non-self-consistently to the already converged scalar-relativistic density. The FT approach can be considered because the SOC term is small compared to the other terms of the KS equation. Hence, its effect on the density of the system can be treated as a perturbation. The FT approximation is correct up to the $\Delta\rho'$ density term (the change in the density when SOC term is included). Terms of $(\Delta\rho')^2$ order have a minor effect due to cancellations between different orientations [115]. The cancellation of different terms allows to obtain the MAE as the difference of the band energies for two magnetization orientations.

$$\text{MAE}_{\text{FT}} = E_{\text{band}}^{\mathbf{a}} - E_{\text{band}}^{\mathbf{b}} = \sum_{n\mathbf{k}} [f^{\mathbf{a}}(\epsilon_{n\mathbf{k}}^{\mathbf{a}})\epsilon_{n\mathbf{k}}^{\mathbf{a}} - f^{\mathbf{b}}(\epsilon_{n\mathbf{k}}^{\mathbf{b}})\epsilon_{n\mathbf{k}}^{\mathbf{b}}] \quad (2.45)$$

where $\epsilon_{n\mathbf{k}}$ is the KS eigenenergy of band n at point \mathbf{k} and \mathbf{a}, \mathbf{b} the directions of the spins. $f^{\mathbf{a}, \mathbf{b}}$ accounts for the Fermi-Dirac distribution for each spin direction, included separately because the Fermi level varies with the magnetization directions. With the FT approach the computational cost of calculating the MAE is considerably reduced.

The SOC term can split band degeneracies depending on the spin orientation. In Fig. 2.4, we show schematically how band splittings due to SOC affect the MAE. In Fig. 2.4 (a) and (b) the bands are fully occupied. Splitting (a) is symmetric, thus, there is no net effect in the MAE. Splitting (b) is asymmetric, favoring the

easy-axis to be the z -axis. In Fig. 2.4 (c) and (d) the Fermi energy lies at the degeneracy point. In (c) one band becomes fully occupied while the other is unoccupied giving the largest contribution to MAE, in this case to the z -axis. The (d) splitting is not affected as the occupation is not modified.

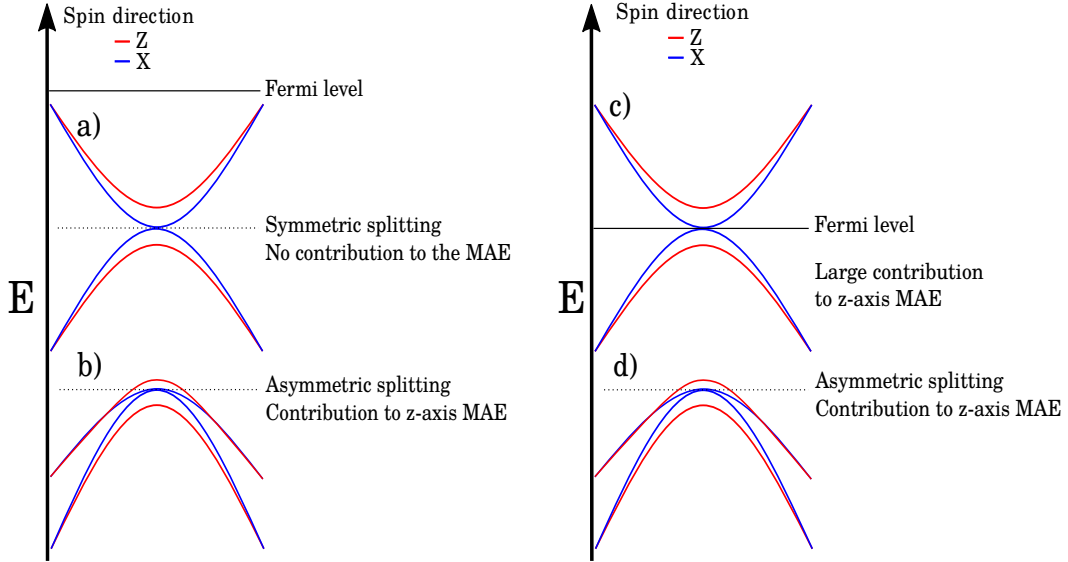


Figure 2.4: Scheme of band splittings induced by SOC and their effect on the MAE.

Making use of the FT method, we can define a MAE density in reciprocal space to understand the origin of the MAE in terms of the electronic structure details as described in Fig. 2.4:

$$\text{MAE density}(\epsilon, \mathbf{k}) = \sum_n \epsilon_{\mathbf{k}n}^{\mathbf{a}} g(\epsilon_{\mathbf{k}n}^{\mathbf{a}} - \epsilon) - \sum_{n'} \epsilon_{\mathbf{k}n'}^{\mathbf{b}} g(\epsilon_{\mathbf{k}n'}^{\mathbf{b}} - \epsilon) \quad (2.46)$$

where $g(\epsilon_{\mathbf{k}n}^{\mathbf{a}} - \epsilon)$ is a Gaussian or a Lorentzian centred at $\epsilon_{\mathbf{k}n}^{\mathbf{a},\mathbf{b}}$ of width σ , this allows us to estimate the MAE contribution of states near energy ϵ at point \mathbf{k} . With this equation, we can identify the band splittings that mainly contribute to the MAE [116].

2.4 Constrained Random Phase Approximation (cRPA)

In Section 2.2, we introduced the theoretical method to add the screened Coulomb interaction as a Hubbard-like term into the *ab initio* calculation, where U and J are parameters. These parameters are often unknown. Several methods have been developed to determine the value of U and J for different systems from first principles. In the constrained local density approximation (cLDA) [117, 118], the Hubbard- U is calculated from the second derivative of the total energy with respect to the occupation number of the localized states. The cLDA does not provide the matrix elements of the screened Coulomb matrix elements neither the frequency dependence of the screened Coulomb interaction (note that the response function of materials under time-dependent external fields is frequency-dependent). It is known that the cLDA overestimates the Hubbard- U value, compared to other methods [119]. Other techniques based on Slater integrals [67] and linear methods that compute the Hubbard- U parameter using response functions calculated by means of constrained DFT [120] have been derived.

The method used in this Thesis is the constrained random phase approximation (cRPA) [119, 121, 122, 123]. The starting point is the fundamental equation of the fully screened Coulomb interaction:

$$W(\mathbf{r}, \mathbf{r}') = \int d\mathbf{r}'' V(\mathbf{r}, \mathbf{r}'') \varepsilon^{-1}(\mathbf{r}', \mathbf{r}'') , \quad (2.47)$$

where V is the bare Coulomb interaction and ε the dielectric function. Within the RPA approximation [124] the dielectric function can be expressed as:

$$\varepsilon(\mathbf{r}, \mathbf{r}'; \omega) = \delta(\mathbf{r} - \mathbf{r}') - \int d\mathbf{r}'' V(\mathbf{r}, \mathbf{r}'') P(\mathbf{r}'', \mathbf{r}'; \omega) , \quad (2.48)$$

where P is the polarization. Note that the polarization induces a frequency dependence in the dielectric function. In the RPA linear response theory, the interacting polarization is approximated by the non-interacting one, which can be written as :

$$P(\mathbf{r}, \mathbf{r}'; \omega) = \sum_{\sigma} \sum_{n\mathbf{k}}^{\text{occ}} \sum_{n'\mathbf{q}}^{\text{unocc}} \psi_{n\mathbf{k}}^{\sigma*}(\mathbf{r}) \psi_{n'\mathbf{k}+\mathbf{q}}^{\sigma}(\mathbf{r}') \psi_{n'\mathbf{k}+\mathbf{q}}^{\sigma*}(\mathbf{r}) \psi_{n\mathbf{k}}^{\sigma}(\mathbf{r}') \quad (2.49)$$

$$\left(\frac{1}{\omega + \epsilon_{n\mathbf{k}}^{\sigma} - \epsilon_{n'\mathbf{k}+\mathbf{q}}^{\sigma} + i0^+} - \frac{1}{\omega - \epsilon_{n\mathbf{k}}^{\sigma} + \epsilon_{n'\mathbf{k}+\mathbf{q}}^{\sigma} - i0^+} \right) ,$$

where $\psi_{n\mathbf{k}}^\sigma$ and $\epsilon_{n\mathbf{k}}^\sigma$ are the KS eigenfunctions and eigenvalues of the system, respectively, the sum for n, \mathbf{k} states runs over the occupied states and that for $n', \mathbf{k} + \mathbf{q}$ over the unoccupied states, and σ is the spin.

In the cRPA, we split the Hilbert space into two separate sets, one composed of the localized states (l) and the other of the rest of the states (r). This results in the separation of the full polarization into transitions inside the localized subspace, P_l and the other transitions, P_r :

$$P = P_l + P_r \quad (2.50)$$

The P_r subspace includes also transitions that end or start in the l subspace⁷. In Figure 2.5, the division of the space is illustrated for the SrVO₃ case. In SrVO₃, the Hubbard- U is calculated for the $t2g$ subspace -the l subset- formed by the orbitals d_{xz} , d_{yz} and d_{xy} .

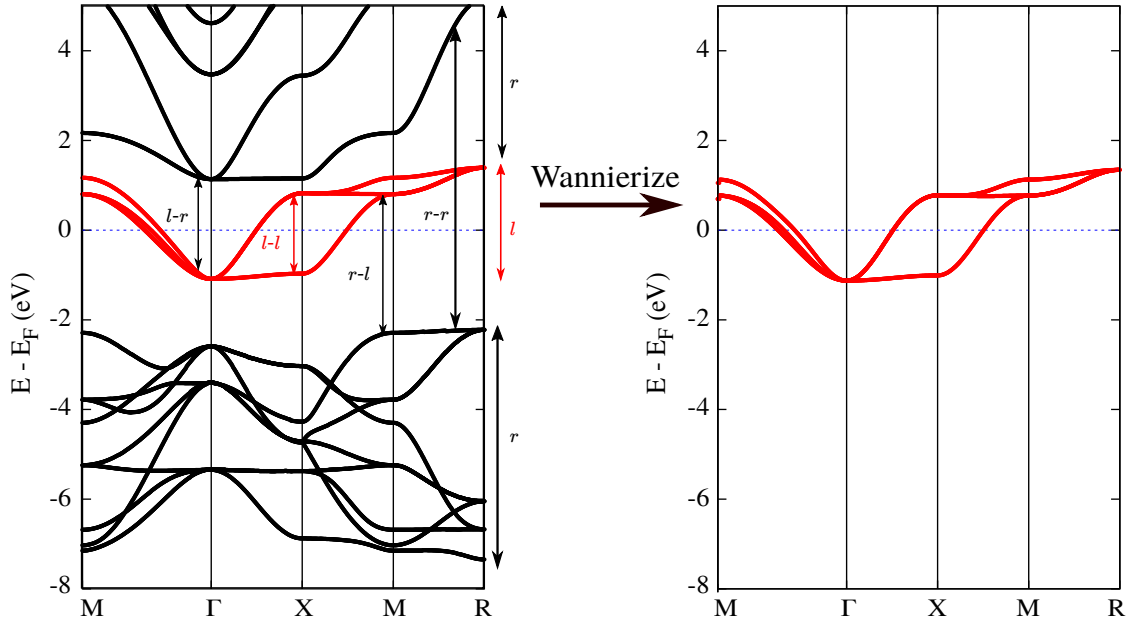


Figure 2.5: Left: SrVO₃ bandstructure with the cRPA space division. The red bands comprise the $t2g$ localized states (l -subspace). The black bands are the r -subspace. The transitions between the states are also shown. Right: Band structure interpolation of the localized subspace spanned by maximally localized Wannier functions.

⁷These contributions are suppressed in the cLDA [121].

Inserting Eq. (2.50) into Eq. (2.48) and combining them with Eq. (2.47), the Coulomb interaction can be rearranged in the following manner⁸ [122]:

$$\begin{aligned} W &= [1 - V(P_l + P_r)]^{-1} V = [1 - (1 - VP_r)^{-1} VP_l]^{-1} (1 - VP_r)^{-1} \\ &= (1 - W_r P_l)^{-1} W_r, \end{aligned} \quad (2.51)$$

where we have defined an interaction, W_r , that excludes the $l-l$ screening channels:

$$W_r = (1 - VP_r)^{-1} V. \quad (2.52)$$

So, W_r is an effective interaction that is screened further when adding the transitions between the localized orbitals, resulting in the fully screened interaction.

Therefore, W_r can be interpreted as an effective interaction that acts on the localized subset, i.e., it is equivalent to the Hubbard- U parameter:

$$U(r, r'; \omega) = W_r(r, r'; \omega) = \int d\mathbf{r}'' [\delta(\mathbf{r} - \mathbf{r}') - V(r, r'') P_r(r', r''; \omega)]^{-1} V(r, r''). \quad (2.53)$$

The latter equation can be solved by any KS system solver. As the Coulomb screened is localized in the atom, to obtain the matrix elements centered in the atom \mathbf{R} , $U_{n_1 n_2 n_3 n_4; \mathbf{R}}(\omega)$, it is natural to choose a localized basis set, where n_i are the orbitals running through $n_l = -l, \dots, l$. The calculation of $U_{n_1 n_2 n_3 n_4; \mathbf{R}}(\omega)$ is straightforward when the strongly correlated states and the other bands are separated. As an example, in Figure 2.5 the bands with $t2g$ orbital character are isolated from the other bands. However, when localized orbitals are hybridized with other orbitals, separating the polarization into two terms is a challenging problem.

Different methods have been proposed to tackle the problem of entangled bands. These methods use maximally localized Wannier functions (MLWFs). The MLWFs built a real-space localized basis from unitary transformations on the Bloch states. The use of the MLWFs was introduced by Miyake *et al.* in Ref. [125]. Still, this technique is not capable of providing a well-defined polarization for each set, as hybridization between the l subspace and r subspace is switched off. Hence, the electronic structure can be modified in the case of strong hybridization.

In this work, we have used the method derived by Şaşıoğlu *et al.* [126], the so-called projection method, which is a parameter-free procedure. The MLWFs span

⁸For the sake of simplicity we use a matrix notation.

the localized orbitals as:

$$w_{m\mathbf{R}}^\sigma(\mathbf{r}) = \frac{1}{N_k} \int d\mathbf{k} e^{-i\mathbf{k}\cdot\mathbf{R}} \sum_{\mathbf{kn}} T_{mn\mathbf{k}}^\sigma \psi_{n\mathbf{k}}^\sigma(\mathbf{r}), \quad (2.54)$$

where $w_{m\mathbf{R}}^\sigma$ are the MLWF centered at the atomic position \mathbf{R} , N_k the number of k -points and $T_{mn\mathbf{k}}^\sigma$ is a unitary matrix. The MLWFs construction will be addressed in the next section.

It can happen that in order to built adequate MLWFs of the localized space, states from the r space need to be considered. In order to obtain adequate P_r and P_l , transitions that take place between the $l-l$ states need to be singled out from the total polarization. The total probability for an electron to be in the localized set before and after the transition $\psi_{n\mathbf{k}}^\sigma \rightarrow \psi_{n\mathbf{k}+\mathbf{q}}^\sigma$ is $p_{\mathbf{kn}}^\sigma p_{\mathbf{k}+\mathbf{q}n'}^\sigma$ where:

$$p_{\mathbf{kn}}^\sigma = \sum_m |T_{mn\mathbf{k}}^\sigma|^2. \quad (2.55)$$

Therefore, for entangled bands we have $p_{\mathbf{kn}}^\sigma p_{\mathbf{k}+\mathbf{q}n'}^\sigma < 1$ and for disentangled bands $p_{\mathbf{kn}}^\sigma p_{\mathbf{k}+\mathbf{q}n'}^\sigma = 1$. Then, P_l is constructed as:

$$P_l(r, r'; \omega) = \sum_\sigma \sum_{n\mathbf{k}}^{\text{occ}} \sum_{n'\mathbf{q}}^{\text{unocc}} (p_{\mathbf{kn}}^\sigma p_{\mathbf{k}+\mathbf{q}n'}^\sigma)^2 \psi_{n\mathbf{k}}^{\sigma*}(\mathbf{r}) \psi_{n'\mathbf{k}+\mathbf{q}}^\sigma(\mathbf{r}') \psi_{n\mathbf{k}}^\sigma(\mathbf{r}') \psi_{n'\mathbf{k}+\mathbf{q}}^{\sigma*}(\mathbf{r}) \quad (2.56)$$

$$\left(\frac{1}{\omega + \epsilon_{n\mathbf{k}}^\sigma - \epsilon_{n'\mathbf{k}+\mathbf{q}}^\sigma + i0^+} - \frac{1}{\omega - \epsilon_{n\mathbf{k}}^\sigma + \epsilon_{n'\mathbf{k}+\mathbf{q}}^\sigma - i0^+} \right).$$

Combining this equation with Eq. (2.50), the polarization for the rest of space P_r is obtained and, from this, $U(\mathbf{r}, \mathbf{r}'; \omega)$. The screened Coulomb matrix elements in the MLWFs basis are given by:

$$U_{m_1 m_2 m_3 m_4; \mathbf{R}}(\omega) = \langle m_1 m_2 | U | m_3 m_4 \rangle \quad (2.57)$$

$$= \int \int d\mathbf{r} d\mathbf{r}' w_{m_1 \mathbf{R}}^{\sigma*}(\mathbf{r}) w_{m_3 \mathbf{R}}^\sigma(\mathbf{r}) U(\mathbf{r}, \mathbf{r}'; \omega) w_{m_2 \mathbf{R}}^{\sigma'}(\mathbf{r}') w_{m_4 \mathbf{R}}^{\sigma'}(\mathbf{r}').$$

The effective Hubbard- U and J parameters are calculated by averaging the matrix elements in the static limit, $\langle U(\omega \rightarrow 0) \rangle$. Different parametrizations exist to do this. The Kanamori parametrization calculates parameters adapted for $t2g$ and eg ($d_{x^2-y^2}$ and d_{z^2} orbitals) [127]. The Slater parametrization was already defined in Eq. (2.31) and Eq. (2.32):

$$U_l = \frac{1}{(2l+1)^2} \sum_{m=-l}^l \sum_{m'=-l}^l U_{mm'mm';0}(\omega=0) \quad (2.58)$$

$$J_l = U_l - \frac{1}{2l(2l+1)} \sum_m^l \sum_{m'}^l [U_{mm'mm';0}(\omega=0) - U_{mm'm'm;0}(\omega=0)], \quad (2.59)$$

where $l = 2$ for the d shell. U_l accounts for the on-site intraorbital interactions and J_l is the on-site inter-orbital exchange parameter. The Coulomb matrix elements spin dependence is small according to calculations [126].

In this work, cRPA calculations have been performed using the SPEX code [128] where the projection method is implemented. SPEX uses previously converged ground-state *ab initio* wavefunctions from the FLEUR code and makes use of the Wannier90 [129] library to construct MLWFs. The SPEX code has the cRPA method implemented by means of the mixed-product basis (MPB)[130]. The polarization function and Coulomb matrix elements involve the calculation of products of wavefunctions, as they describe the initial and final states between two electrons. Each product arising from initial and final state pairs is transformed to the MPB, which allows an efficient numerical evaluation of the total polarization and the Coulomb matrix elements using the FLAPW basis provided by FLEUR. The MPB allows a mathematically exact treatment of the divergence of the Coulomb interaction at $\mathbf{k} \rightarrow 0$.

In Figure 2.6 a simplified workflow to compute the Hubbard- U parameters is shown. Two key factors to obtain well converged Hubbard- U parameters. First, proper convergence in the DFT+ U calculation is needed. Second, the MLWFs need to be properly localized and centered. Only then, we can calculate the polarizations (P , P_l and P_r) and screened matrix elements (U and J). All these values are computed in the same run of SPEX.

2.5 Maximally Localized Wannier Functions

Bloch-like wavefunctions can be expanded into a real-space localized basis, as proposed by Wannier [131]. We give below a summary of the construction of the Wannier functions (WF). For a detailed description, we refer to the review Ref. [132]. The WF can be written as:

$$|\mathbf{R}n\rangle = \frac{1}{\sqrt{N}} \sum_{\mathbf{k}} e^{-i\mathbf{k}\cdot\mathbf{R}} |\psi_{\mathbf{k}n}\rangle, \quad (2.60)$$

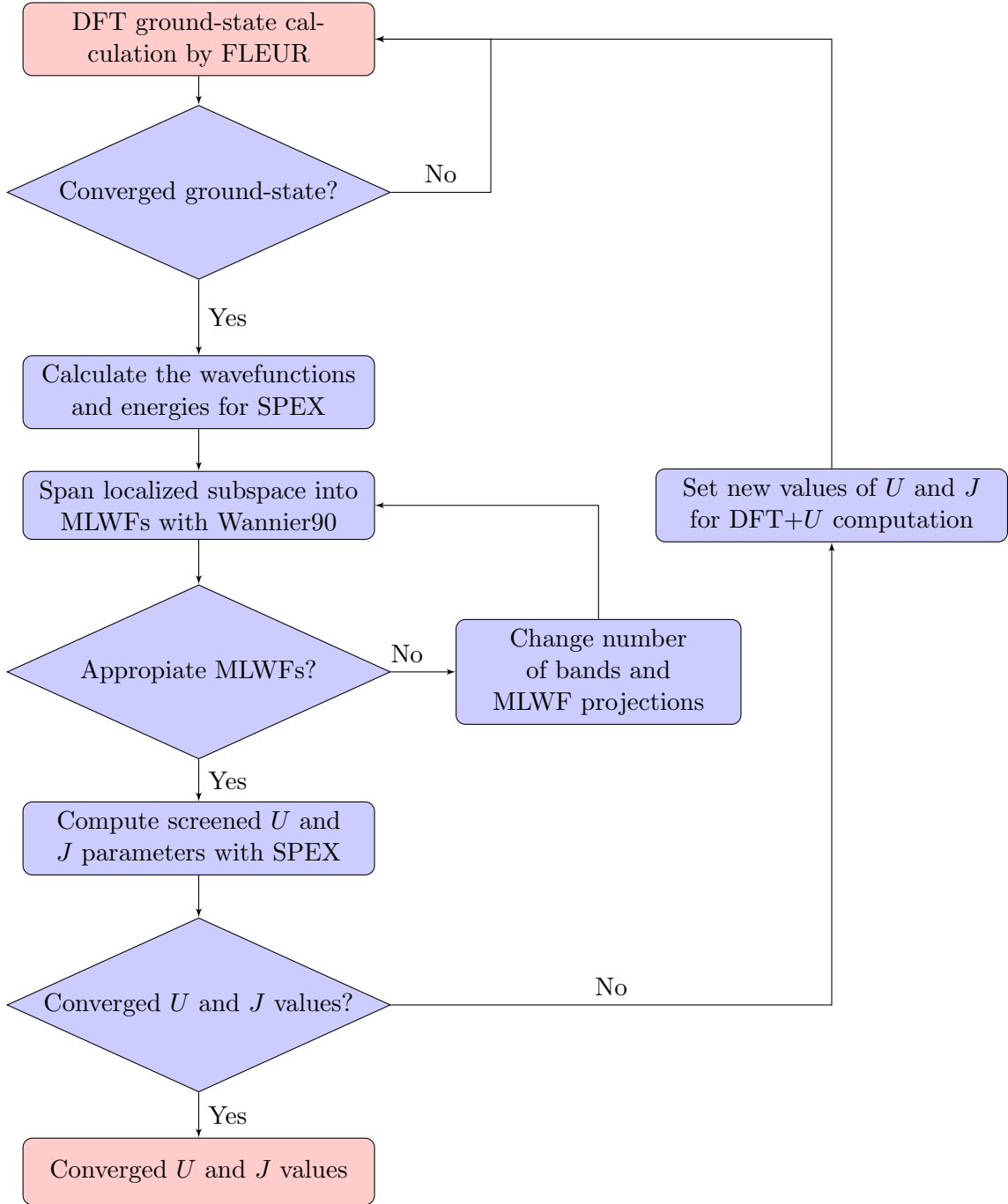


Figure 2.6: Scheme of the work flowchart to calculate the values of the U and J combining FLEUR, SPEX and Wannier90.

where N is the number of k -points in the 1BZ and \mathbf{R} a lattice vector. The coordinate representation is obtained as $\langle \mathbf{r} | \mathbf{R}n \rangle = w_{\mathbf{R}n}(\mathbf{r})$. The inverse transformation from WF to Bloch states is:

$$|\psi_{\mathbf{k}m}\rangle = \frac{1}{\sqrt{N}} \sum_{\mathbf{R}} e^{i\mathbf{k}\cdot\mathbf{R}} |\mathbf{R}m\rangle . \quad (2.61)$$

Eq. (2.60) and Eq. (2.61) constitute a unitary linear transformation between the WFs and Bloch functions. Thus, both are valid to describe electronic bands. Bloch functions show a "gauge freedom" that makes them invariant to unitary transformations. The generalized gauge freedom for a multiband case of M bands is expressed as:

$$|\psi'_{\mathbf{k}m}\rangle = \sum_{n=1}^M T_{mn\mathbf{k}} |\psi_{\mathbf{k}n}\rangle , \quad (2.62)$$

where $T_{mn\mathbf{k}}$ is a unitary matrix of dimension $M \times M$. When a multiband manifold is considered states can be degenerate at band crossings. At these points, the Bloch states are not analytic. Hence, constructing WFs from degenerate bands would result in poor localization and it is necessary to include the unitary matrix transformation. To solve the latter problem, the non-uniqueness of the WFs is used. The T matrix induces unitary rotations to obtain smooth wavefunctions at the degenerate points, resulting in well-localized WFs. Although, the trace is preserved, $|\psi'_{\mathbf{k}m}\rangle$ may not be an eigenstate, and the index m is no longer a valid band index. Inserting Eq. (2.62) into Eq. (2.60) gives the general WF construction:

$$|\mathbf{R}m\rangle = \frac{1}{\sqrt{N}} \sum_{\mathbf{k}} e^{-i\mathbf{k}\cdot\mathbf{R}} \sum_{n=1}^M T_{mn\mathbf{k}} |\psi_{\mathbf{k}n}\rangle . \quad (2.63)$$

The unitary matrix rotation has to be optimized to obtain "maximally localized" WFs. In this work we use the technique derived by Marzari *et al.*[133], whose localization functional is:

$$\Omega = \sum_m [\langle 0m|r^2|0m\rangle - \langle 0m|\mathbf{r}|0m\rangle] = \sum_m [\langle r^2 \rangle_m - \langle \mathbf{r}_m \rangle^2] . \quad (2.64)$$

It measures the sum of the quadratic spreads of the WFs centers located at the initial unit cell. Bount *et al.*[134] proved that the matrix elements for the position operator could be obtained by means of derivatives with respect to the wave vector \mathbf{k} , which can be calculated using finite differences. All the needed information is given by the overlap between neighboring Bloch states,

$$M_{mn}^{\mathbf{k},\mathbf{b}} \equiv \langle \psi_{m'\mathbf{k}} | \psi_{m\mathbf{k}+\mathbf{b}} \rangle . \quad (2.65)$$

At each iteration, the overlap and the transformation matrix are updated in order to minimize Ω . This method can be extended to include non-isolated bands, i.e., entangled bands [135].

Chapter 3

Magnetic properties of planar free-standing transition metal oxide chains

I'm not so good with the advice... Can I interest you in a sarcastic comment?

Chandler Bing, *Friends*

3.1 Introduction

Reduction of coordination in low-dimensional systems results in less atoms forming bonds, enabling the emergence of magnetism in materials that are non-magnetic in bulk [29, 9, 136].

Theoretical methods, e.g., DFT, have made it possible to study different low-dimensional systems, from 2D [137] to 1D systems [48, 138] and adatoms (0D) [139, 140]. Typically, reducing the dimension results in larger spin and orbital moments, the magnetic anisotropy being enhanced as well. The magnetic anisotropic energy (MAE) is a necessary property for low dimensional systems to allow a long-range magnetic order at finite temperature [30]. Furthermore, enhancement of

spin-orbit effects and the sizeable energetic difference between the easy- and hard-axes of magnetization, i.e., magnetocrystalline anisotropy, make low-dimensional systems suitable¹ for spintronic devices [142, 143].

The Hubbard Hamiltonian is used to describe the interaction between the localized electrons within certain orbitals, for instance, electrons in the $3d$ orbital of transition metals. The larger the Hubbard- U parameter the larger localization of electrons. Localization of electrons favors larger magnetic moments. Therefore, the U parameter value can induce the stabilization of magnetic states and its variation can alter the spin state.

In this chapter, we study the ground-state magnetic properties of transition metal-oxide (TMO) chains XO_2 , where $X = \text{Ni, Co, Fe, and Mn}$ [23]. These chains can be grown on Ir and Pt substrates [74]. Spin-polarized STM (SP-STM) experiments have determined some of their magnetic properties [74]. Combining SP-STM data with DFT calculations, the presence of non-collinear spins between adjacent MnO_2 chains has been observed. The non-collinear spin texture results from an antisymmetric exchange interaction mediated by the substrate, indicating the presence of a RKKY interaction[144]. The experimental data do not always agree with the theoretical calculations. For instance, $\text{CoO}_2/\text{Ir}(100)$ is predicted to show a FM coupling [23], while no such magnetic contrast is observed with SP-STM[74]. Measuring the magnetic properties is a difficult task, hence, theoretical calculations are needed. In particular, DFT allows us to understand the magnetic properties in terms of the electronic structure of the chains. There, we study the spin states of the TM atoms dependence on the intrachain interaction, i.e., U . We calculate the magnetic coupling between the X atoms and obtain the MAE of each chain. The anisotropy is calculated using two methods: treating SOC in a self-consistent manner and the FT approach (see Section 2.3 for the background of these two techniques), to test the applicability of the latter method in this family of systems.

The chapter is structured as follows: in Section 3.2 the geometry of the planar unsupported chain. Then, in Section 3.3, we show the obtained spin states for each metal atom. Next, in Section 3.4, we describe the exchange coupling between the metal atoms. In Section 3.5, we compute the MAE and analyze the obtained easy-axes in terms of the resulting band structures. Finally, in Section 3.6, we give the conclusions based on the obtained results.

¹Particularly, when the out-of-plane direction is the easy-axis[141].

3.2 Structure model

The one-dimensional XO_2 chains, where $X=$ Ni, Co, Fe, Mn, form in an Ir(100) surface. Structural analyses carried out with LEED-IV and STM show defect-free chains with 500 atom lengths arranged in periodically ordered (3×1) domains orientated along the $[110]$ and $[1\bar{1}0]$ crystallographic directions. The procedure to grow the chains is given by Ferstl *et al.*[23]: the chains are formed on Ir(100)- (2×1) -O or on metastable Ir(100)- (1×1) by depositing 0.33 of a monolayer of each transition metal atom followed by an annealing in a 1×10^{-7} mbar O_2 atmosphere. In Fig. 3.1 the structure of the system is shown.

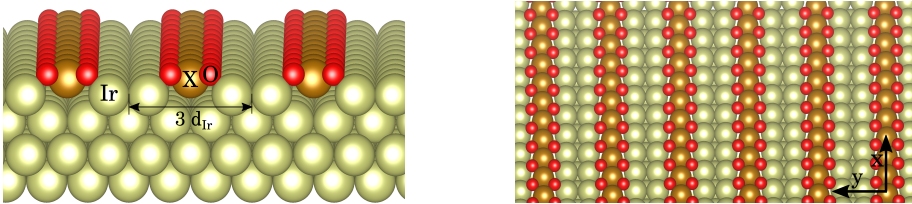


Figure 3.1: Left: side view of the structure of the XO_2 chains. Chains are separated by $3d_{Ir}$, where $d_{Ir} = 2.71\text{\AA}$ is the Ir(100) lattice constant. Right: top view.

In our first calculations, instead of the whole system, we consider the ideal case of a planar free-standing chain (see 3.2). The chains are isolated from the Ir substrate and the oxygens atoms are placed between the transition metal atoms coplanarly.

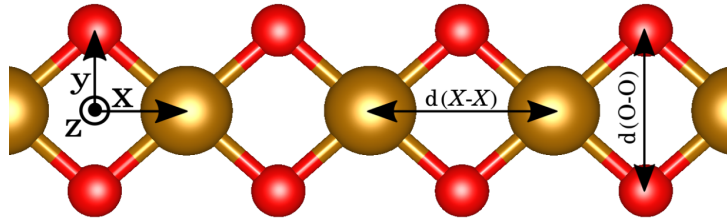


Figure 3.2: Planar free-standing chain geometry.

3.3 Planar free-standing chain: Spin phase diagrams

DFT calculations were performed using the VASP code, with the PBE exchange-correlation functional [84] and Dudarev's formulation of the DFT+ U functional

[102] where the interaction parameter is given by $U - J$, applied to the d -orbital. In all calculations, J is set to 0. We used a plane-wave energy cut-off of 450 eV with a Γ -centered $10 \times 1 \times 1$ k -point grid. To avoid interaction between different chains, we set 10 Å of vacuum between the chain's periodic replicas. The total energy convergence threshold is set at 10^{-6} eV. The geometry relaxation is performed until the forces are less than < 0.01 eV/Å. We optimize the distance between the X - X and O - O atoms to obtain the relaxed ground state.

In Fig. 3.3, the resulting spin values for different X - X and O - O distances are shown as spin state phase diagrams for $U - J = 0, 1.5$ and 5 eV. The spin values at the ground state for each U parameter are tabulated in Table 3.1. Note that the spin states differ from an integer or half-integer value because in DFT the occupation matrix elements are fractional². The fractional occupations indicate that the m_l orbitals of the d shell are forming bonds, instead of being empty or fully occupied as in the isolated atom case (see Section 2.2).

A non-magnetic state appears in all chains when the Hubbard U parameter is set to 0 eV. Generally, multiple spin states are accessible by modifying only the value of U . Increasing the value of the U increases the spin value. In the case of Ni, two states are accessible. The equilibrium geometry at $U = 0$ eV lies at the boundary between the non-magnetic and the magnetic state, implying that a small distortion could drive it either to magnetic polarization or quenching. For finite U values, the Ni atom stabilizes in a magnetic state with $S = 1/2$. The Co atom lies in a magnetic state for all U values. For $U = 0$ eV and $U = 1.5$ eV, the Co atom is in a $S = 1$ state and for $U = 5$ eV the spin state is at the transition between $S = 1$ and $S = 3/2$. Fe and Mn atoms are both in magnetic states with $S = 3/2$ for $U = 0$ eV and $U = 1.5$ eV. For $U = 5$ eV both atoms show a spin state $S = 2$.

U (eV)	NiO ₂	CoO ₂	FeO ₂	MnO ₂
	S^{Ni}	S^{Co}	S^{Fe}	S^{Mn}
0	0.29	0.98	1.52	1.47
1.5	0.47	1.05	1.63	1.61
5	0.55	1.26	1.83	1.88

Table 3.1: Spin states of the metal atoms in the equilibrium geometry for different Hubbard- U parameters.

²In the analysis, we will mention the closest spin value.

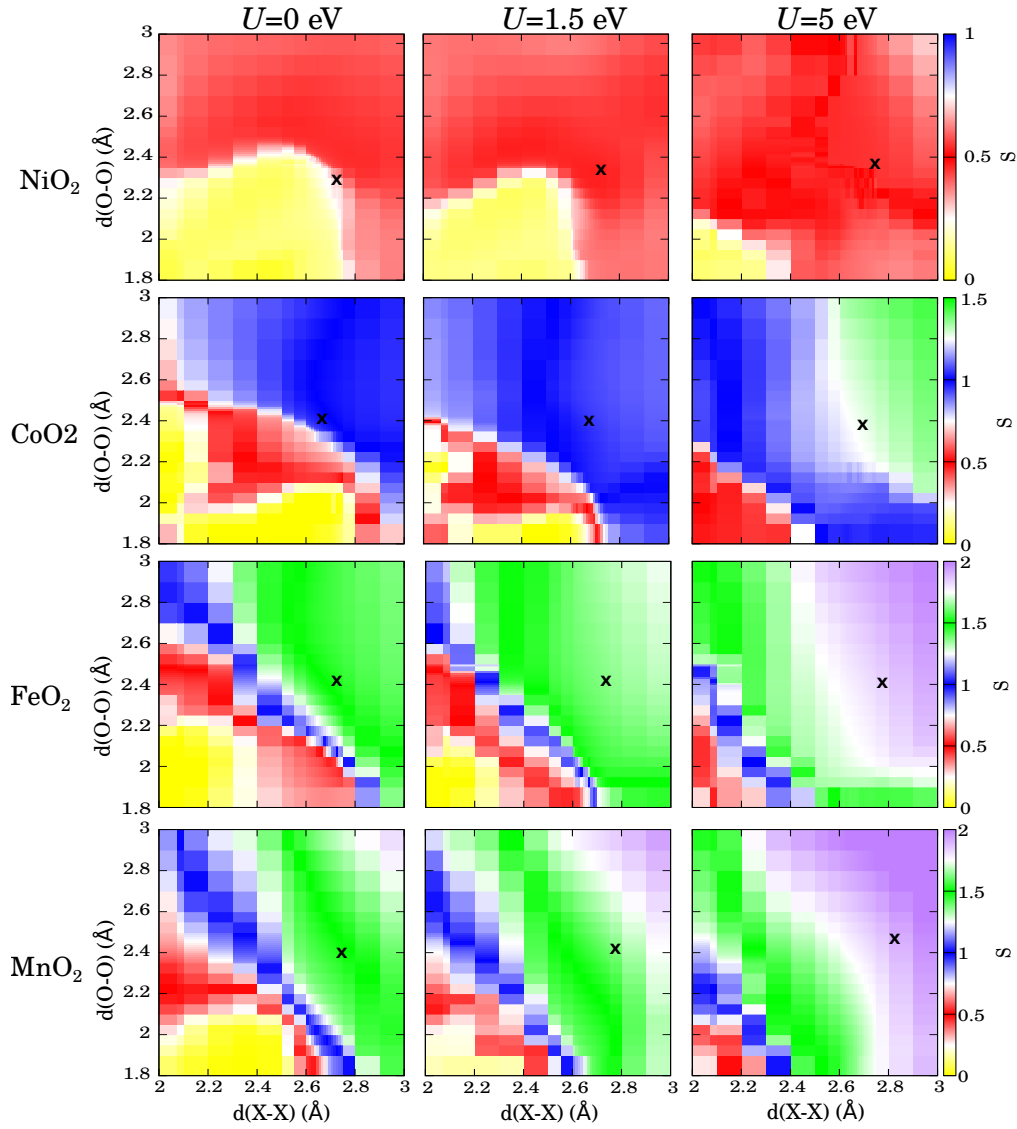


Figure 3.3: Spin values for different planar chain geometries. The distance between metal atoms, $d(X-X)$, and oxygen atoms, $d(O-O)$ is varied for three U values. Colors show different spin values and white spaces indicate a spin state transition. The black cross indicates the ground state configuration in each case.

Table 3.2 shows the equilibrium $X-O$ bond lengths. They are weakly affected by the increase of the Hubbard- U parameter. The maximum change is 5% for the MnO₂ between the $U=0$ and 5 eV, while in the other chains, it is less than 2%.

U (eV)	NiO ₂	CoO ₂	FeO ₂	MnO ₂
	$d_{\text{Ni-O}}$ (Å)	$d_{\text{Co-O}}$ (Å)	$d_{\text{Fe-O}}$ (Å)	$d_{\text{Mn-O}}$ (Å)
0	1.77	1.78	1.82	1.82
1.5	1.79	1.79	1.82	1.83
5	1.80	1.79	1.83	1.87

Table 3.2: Equilibrium X -O bond lengths at each ground state given by the U values.

3.4 Magnetic coupling in planar free-standing chains

The magnetic order of the ground state of each chain has been calculated for the Hubbard- U parameter given in the literature $U = 1.5$ eV [23, 74, 144]. The low value of U is used to consider the screening effects of the Ir substrate in the chains. The supercell is doubled and the transition metals' magnetic moments are set parallel, i.e., a ferromagnetic (FM) state or anti-parallel, i.e., antiferromagnetic (AFM) state. To consider possible effects in the total energy due to strain, the AFM doubled cell has been relaxed for each magnetic configuration. In Table 3.3, we give the bond-length at each magnetic coupling. The largest difference between the AFM and FM states bond-length is 0.02 Å for the CoO₂. Therefore, setting either magnetic coupling affects slightly the bond length.

We describe the magnetic exchange of the chains with a Heisenberg model:

$$H = - \sum_{\langle ij \rangle} \mathcal{J}_{ij} \mathbf{S}_i \cdot \mathbf{S}_j , \quad (3.1)$$

where $\langle ij \rangle$ indicates that the sum is over pairs of nearest neighbors. \mathbf{S}_i is the spin for the transition-metal atom in site i and \mathcal{J}_{ij} the magnetic exchange coupling parameter between spins at sites i and j . The sign of the exchange coupling determines if the coupling is FM, $\mathcal{J} > 0$, or AFM, $\mathcal{J} < 0$. In DFT calculations, the exchange coupling parameter is obtained from the difference of total energies of the AFM and FM magnetic configuration, calculated in a doubled cell:

$$\mathcal{J} = \frac{E_{\text{AFM}} - E_{\text{FM}}}{2S^2} \quad (3.2)$$

The interaction between the TM atoms is mediated by the oxygen atoms. This type of indirect interaction is known as the superexchange interaction [145, 146]. In Table 3.3, we summarize the results obtained by doubling the cell. The X -O bond lengths at the AFM and FM states differ less than 2%. The energy difference,

$\Delta E = E_{\text{AFM}} - E_{\text{FM}}$, establishes that for the NiO₂, CoO₂ and FeO₂ the preferred magnetic coupling is AFM, while MnO₂ is FM. In the FM state, the oxygen atoms are polarized parallel to the X atoms spin except in the MnO₂, where they are set antiparallel. In a naive reasoning, the O atom's spin inversion in the latter chain determines the Mn atom coupling, setting the order of Mn \uparrow -O \downarrow -Mn \uparrow . In the AFM state, the O atoms do not show any polarization as the oxygen atoms lie in the center plane between the two metal atoms with opposite polarizations.

$X\text{O}_2$	$d_{X\text{-O}}$ (Å)	μ_S^X (μ_B)	μ_S^O (μ_B)	ΔE (meV)	\mathcal{J} (meV)
NiO ₂ (AFM)	1.78	0.89	0.00	-42	-95
NiO ₂ (FM)	1.79	0.95	0.43		
CoO ₂ (AFM)	1.77	2.01	0.00	-350	-159
CoO ₂ (FM)	1.79	2.12	0.36		
FeO ₂ (AFM)	1.81	3.11	0.00	-476	-90
FeO ₂ (FM)	1.82	3.26	0.24		
MnO ₂ (AFM)	1.82	2.86	0.00	562	108
MnO ₂ (FM)	1.83	3.23	-0.18		

Table 3.3: Obtained data for the AFM and FM magnetic orders. The relaxed bond-lengths between TM and O atoms, spin magnetic moments of the TM atom μ_S^X and oxygen atom μ_S^O are given for both magnetic states. The calculations were performed for the 2×1 supercell with $U = 1.5$ eV.

In Fig. 3.4, we show the projected density of states (DOS) of the $X\text{O}_2$ onto the $X(d)$ and $O(p)$ orbital for each magnetic state. We make the important observation that the AFM chains (NiO₂, CoO₂, and FeO₂) are insulators, while MnO₂, which favors a FM state, is *half-metallic*³. In CoO₂ and FeO₂, the AFM state shows a larger gap than the FM state, the larger gap the lower the total energy. For MnO₂, the insulating behavior of the minority spin in the FM state implies a lowering of the total energy compared to the metallic AFM state. Now, looking at the total energy difference between the magnetic states in Fig. 3.4, we see that the difference increases from NiO₂ to MnO₂. Being the largest difference between the metallic AFM vs. half-metallic FM state of the MnO₂ chain.

³In a half-metallic compound, one spin channel is metallic while the other presents a gap.

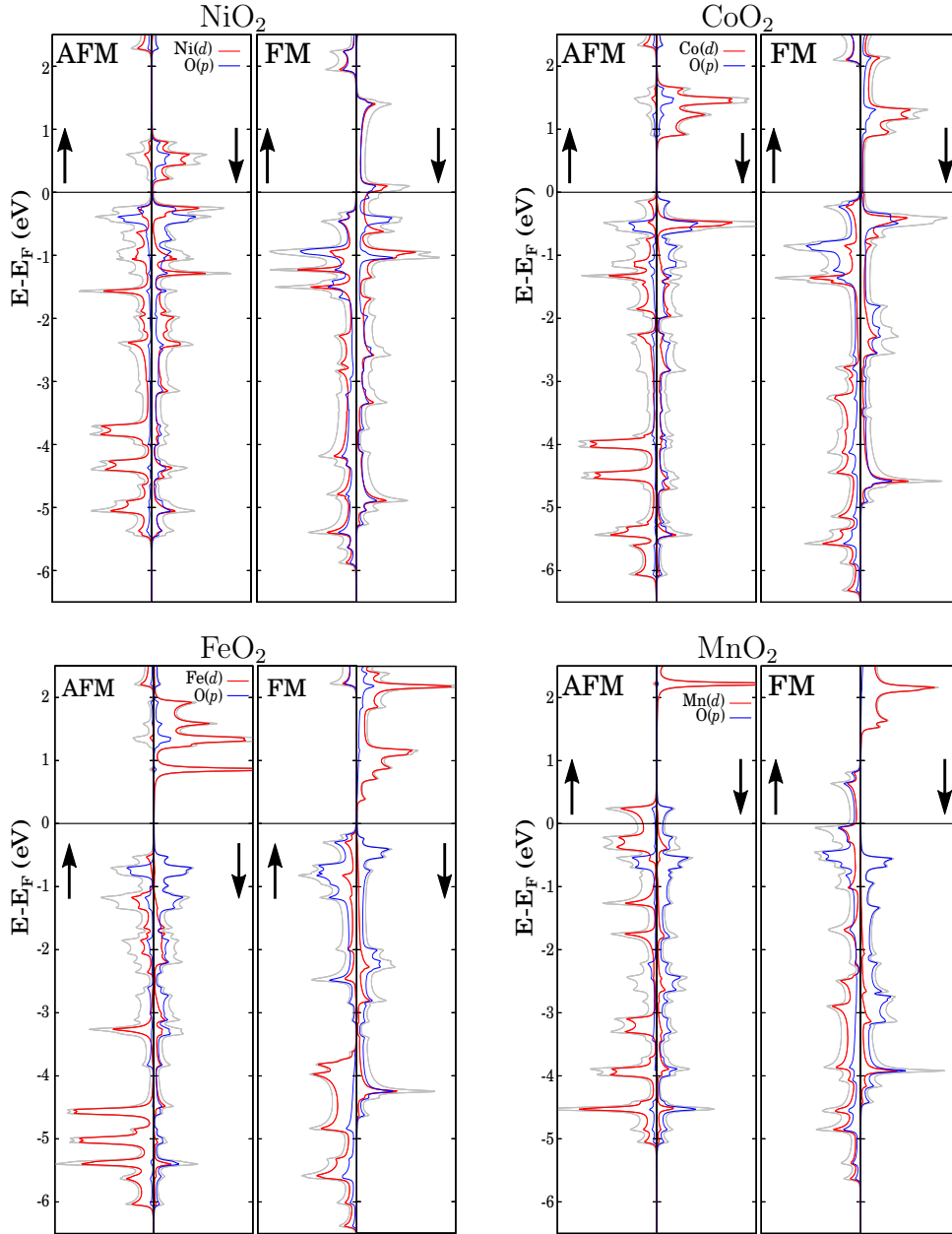


Figure 3.4: Projected density of states. The solid gray indicates the total DOS, red and blue are the projections on the $X(d)$ and $O(p)$ orbitals, respectively. Only the projections on atoms in one half of the (2×1) cell are plotted.

3.5 Magnetic Anisotropic Energy in planar free-standing chains

We have calculated the MAE for the planar free-standing chains with $U = 1.5$ eV with two methods: SCF and the FT approach. In the latter one, the SOC term

is added non-self-consistently to a converged spin-polarized electron density, while in the former SOC is considered in a self-consistent manner (see Section 2.3). We have calculated the MAE for several plane-wave energy cut-offs and k -point grids to obtain properly converged values. The total energy convergence threshold for both calculation setup is 10^{-8} eV. We give in Appendix A the convergence tests of the MAE.

	MAE^{FT} (meV)	MAE^{SCF} (meV)	Easy-axis
NiO ₂	-2.04	-6.43	y
CoO ₂	-0.51	-0.84	y
FeO ₂	0.81	1.13	z
MnO ₂	0.54	0.96	z

Table 3.4: We show the MAE values between the *hardest*- and easiest-axis of each chain, which is the $y - z$ difference. The MAE is obtained using the SCF and FT techniques.

In Table 3.4, we summarize the obtained MAE and the easy axes of magnetization. For the NiO₂ and CoO₂, we obtain that the easy-axis is the y -axis, i.e., across the chain axis (see Fig. 3.2 for the orientations). The FeO₂ and MnO₂ chains have the easy axis along the z -axis direction. The FT approach and calculations including SOC self-consistently agree in the prediction of the easy axis. The MAE values differ between both techniques, but overall the agreement is acceptable, except in the case of the NiO₂ where the self-consistent MAE is three times larger than the FT one. To understand this, we calculate the band structure of NiO₂ in both approaches (see Fig. 3.5). The main difference between the band structures is seen around the Fermi level, at $k \approx 0.25$, where for SCF a band becomes fully occupied, but it is still partially unoccupied for the FT. This significant change in the contributing eigenenergies at the Fermi level can result in a substantial difference in the MAE (see Fig. 2.4), as seen in Table 3.4. In the NiO₂ case, the FT method fails to describe the SOC effect correctly in the system. Hence, the converged wavefunctions may differ between the two methods. The FT has been successfully applied to bulk systems [116], but it is less accurate for lower dimensional systems [147, 148], because the wavefunction is less constrained by symmetries than in bulk materials and can have larger variations when allowed to relax in the presence of a SOC term in the Hamiltonian.

The NiO₂ chain also shows magnetic anisotropy for $S = 1/2$. It has been stated that systems with $S = 1/2$ should not show any magnetic anisotropy [149, 150]. The hybridization between orbitals modifies the orbital shapes and can cause par-

tial fillings in the orbitals used in DFT, such as the X -O bonds do in our system. That is to say, DFT results are not to interpret with a single-ion perspective.

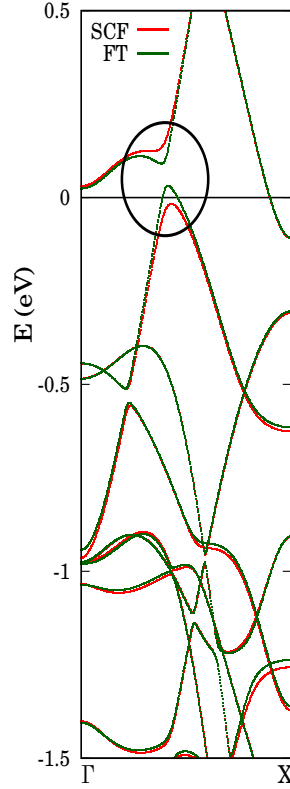


Figure 3.5: Band structure of the NiO_2 chain where SOC is introduced in a self-consistently (green, SCF) and non-SCF (red, FT). The circle highlights the feature that explains the MAE difference.

In Table 3.5, we give the orbital moments. The orbital moment projection of each chain, μ_i^i , is defined by projecting \mathbf{L} on the \mathbf{S} vector, at each calculation, where \mathbf{S} is aligned to different magnetization axes $i = x, y, z$. The orbital moments calculated in the FT approach are lower than in the SCF ones. In the latter, the charge density is allowed to be modified contrary to the FT. Therefore, larger orbital moments are obtained for the SCF than for the FT method. In all calculations, the \mathbf{L} and \mathbf{S} vector remain colinear after the energy minimization procedure.

The NiO_2 and CoO_2 orbital moments along the easy axis are ten times larger than the ones obtained for FeO_2 and MnO_2 . The difference in the orbital moments comes from the minority d orbital configuration. Empty and full orbitals do not contribute to the orbital moment. Comparing the minority spin orbital

	SCF			FT			Easy-axis
	$\mu_l^x (\mu_B)$	$\mu_l^y (\mu_B)$	$\mu_l^z (\mu_B)$	$\mu_l^x (\mu_B)$	$\mu_l^y (\mu_B)$	$\mu_l^z (\mu_B)$	
Ni	0.088	0.215	0.032	0.066	0.106	0.024	y
Co	0.097	0.121	0.018	0.065	0.072	0.014	y
Fe	0.031	0.020	0.008	0.030	0.017	0.006	z
Mn	-0.020	-0.012	-0.022	-0.016	-0.011	-0.017	z

Table 3.5: Orbital moments of each metal atom when SOC is included.

occupations, we see that the NiO₂ and CoO₂ chains have partially filled orbital occupancies, except the full d_{z^2} , that contribute to the orbital moment, while in the FeO₂ and MnO₂, all orbitals except the partially filled d_{xy} are almost empty.

P. Bruno, using a second-order perturbative analysis, established that the MAE and orbital magnetic moment anisotropy, $\mu_l^\perp - \mu_l^\parallel$, were proportional to each other by a constant $C > 0$ [114, 54]. This relation is valid if spin-flips are neglected and the majority spin band is completely filled. Bruno's relation allows us to understand the MAE in terms of the orbital moments direction of the magnetic atom. The orbital moment of each chain is larger at the easy-axis of each chain, fulfilling Bruno's relation, except in the FeO₂ chain. Here, considering that the majority spin shows a partially filled d_{xy} the requirements to fulfill Bruno's relation are not completely met.

The orbital moment direction depends on the occupation of the d orbitals. According to Stöhr [55], the electron residing in a certain orbital is able to "hop" between the lobes of the orbital. As shown in Fig. 3.6(a) for the d_{xy} case, the hopping in the xy plane of the electrons sets the orbital moment direction. Therefore, the d_{xy, x^2-y^2} orbitals contribute to μ_l^\perp , and the $d_{xz, yz}$ orbitals to μ_l^\parallel .

In the MnO₂ chain, the only contribution to the orbital moment is the partially filled d_{xy} orbital, which sets the orbital moment in the z -axis. In the NiO₂ and CoO₂ chains, except the full d_{z^2} the rest of the orbitals contribute to the orbital moment, thus, the preferred orbital moment orientation can not be easily predicted. However, considering that the TM atoms bind with the coplanar oxygen atoms, because of the crystal field and hybridization with the atom, the d_{xy, x^2-y^2} orbitals are perturbed, resulting in a quenched out-of-plane orbital moment (see Fig. 3.6(b)). The $d_{xz, yz}$ orbitals are not too affected by the oxygen atoms. Hence, the orbital moment has a larger contribution in the xy -plane, setting the in-plane orbital moment. The O and TM atoms do not form a perfect square, resulting on

a larger orbital moment projection on the y -axis, as in the NiO_2 and CoO_2 chains.

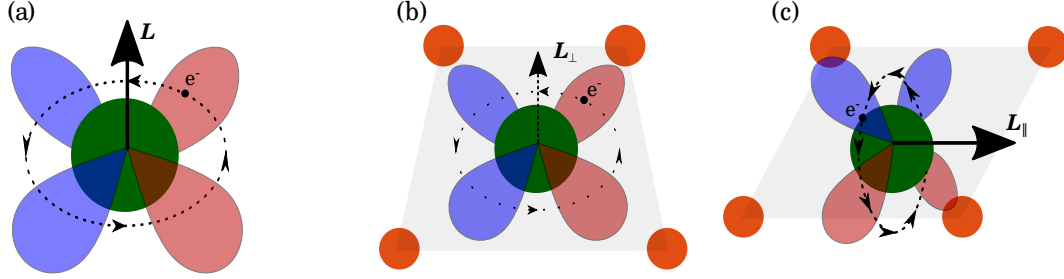


Figure 3.6: (a) The hopping electron is the origin of the out-of-plane orbital moment. (b) The out-of-plane orbital moment (L_{\perp}) is quenched because of the O atoms, while (c) the in-plane moment (L_{\parallel}) is almost non-affected.

MAE density for $X\text{O}_2$ chains

We have analyzed the band-resolved MAE and have used the orbital-projected band structure to identify the orbital character of the band splittings by SOC that mainly contribute to the MAE. The band degeneracy breakings can be accounted for by the matrix elements $\langle \psi_l^{\sigma} | \mathbf{l} \cdot \mathbf{s} | \psi_l^{\sigma'} \rangle$ using the one-electron wavefunctions (ψ_l^{σ}) with d orbital character ($l = 2$) of spin σ [108, 109].

$\langle n \mathbf{l} \cdot \mathbf{s} m \rangle$	$ x^2 - y^2\rangle$	$ xz\rangle$	$ z^2\rangle$	$ yz\rangle$	$ xy\rangle$
$\langle x^2 - y^2 $	0	$i\hat{s}_y$	0	$i\hat{s}_x$	$-2i\hat{s}_z$
$\langle xz $	$-i\hat{s}_y$	0	$i\sqrt{3}\hat{s}_y$	$-i\hat{s}_z$	$i\hat{s}_x$
$\langle z^2 $	0	$-i\sqrt{3}\hat{s}_y$	0	$i\sqrt{3}\hat{s}_x$	0
$\langle yz $	$-i\hat{s}_x$	$i\hat{s}_z$	$-i\sqrt{3}\hat{s}_x$	0	$-i\hat{s}_y$
$\langle xy $	$2i\hat{s}_z$	$-i\hat{s}_x$	0	$i\hat{s}_y$	0

Table 3.6: Matrix elements of the $\mathbf{l} \cdot \mathbf{s}$ operator for the d orbitals, given in Ref.[108, 109].

We show in Fig. 3.7 the electronic structure for each chain including SOC in the FT approach for all chains. We compare the band splittings that occur with the magnetization along the y - (blue) or z -axis (red) and mark with circles the band splittings that have the largest contribution to the easy-axis determination according to the MAE density (Fig. 3.7 panels (d)).

In NiO_2 , four main splittings can be identified that contribute to the y -axis (blue), as shown in Fig. 3.7. These splittings occur between the spin majority d_{yz}

and minority d_{z^2} orbitals crossing. In the bottom left, the splitting is given by minority d_{xy} and $d_{x^2-y^2}$, and in the bottom right, the splitting is between majority d_{xy} and $d_{x^2-y^2}$. In CoO_2 (Fig. 3.7) two splittings are the main contribution to the y -axis. The top splitting is between the majority d_{xz} and minority d_{z^2} . Other split bands are the minority $d_{x^2-y^2}$ and the majority d_{xz} . For the FeO_2 , the easy-axis is the z -axis. Only the crossing of majority d_{xz} and d_{z^2} orbital has an appreciable contribution to anisotropy along the z -axis at $E - E_F = -3$ eV. In the MnO_2 , the MAE density shows two red spots that lie deep in the energy, i.e., $E - E_F = -3$ and -4 eV, where the splitting is between the $d_{z^2,\uparrow}$ and the $d_{xz,\uparrow}$ setting the easy-axis along the z -axis. Second-order perturbation analysis of the SOC set that the main contribution to the MAE is due to splittings near Fermi level, but in all of our chains, there are splittings lying deeper than the Fermi level in energy, which show an appreciable contribution to the MAE.

Apart from the key factor that the split bands have different orbital characters, another essential element is the occupation of the d orbital. The FeO_2 chain has one electron less compared to the CoO_2 chain so that an occupied minority d_{z^2} band in CoO_2 crossing becomes unoccupied in FeO_2 . These bands show a split that contributes to the y -axis in the CoO_2 , but not in FeO_2 . These two splittings involve bands with the same orbital character: majority d_{xz} and d_{z^2} . The latter atoms, FeO_2 and MnO_2 , have a similar d orbital filling that makes them follow the same trend having the same easy-axis with the same orbital character band splittings, even if the magnetic ground state coupling differs.

3.6 Conclusions

To summarize, we have studied the magnetic properties of ideal isolated and planar XO_2 ($X=\text{Ni, Co, Fe, Mn}$). We have obtained the spin phase diagram in the configuration space for a range of variations of the bond lengths and different selected Hubbard- U values. The chains show up to four different spin states.

For $U=1.5$ eV, NiO_2 , CoO_2 and FeO_2 , the preferred magnetic ordering is AFM while the MnO_2 is in a FM state. Band structure calculations indicate that chains preferring the AFM coupling are insulators, and the MnO_2 chain, FM shows a half-metallic state and metallic in the AFM i.e., the band gap reduces the total energy.

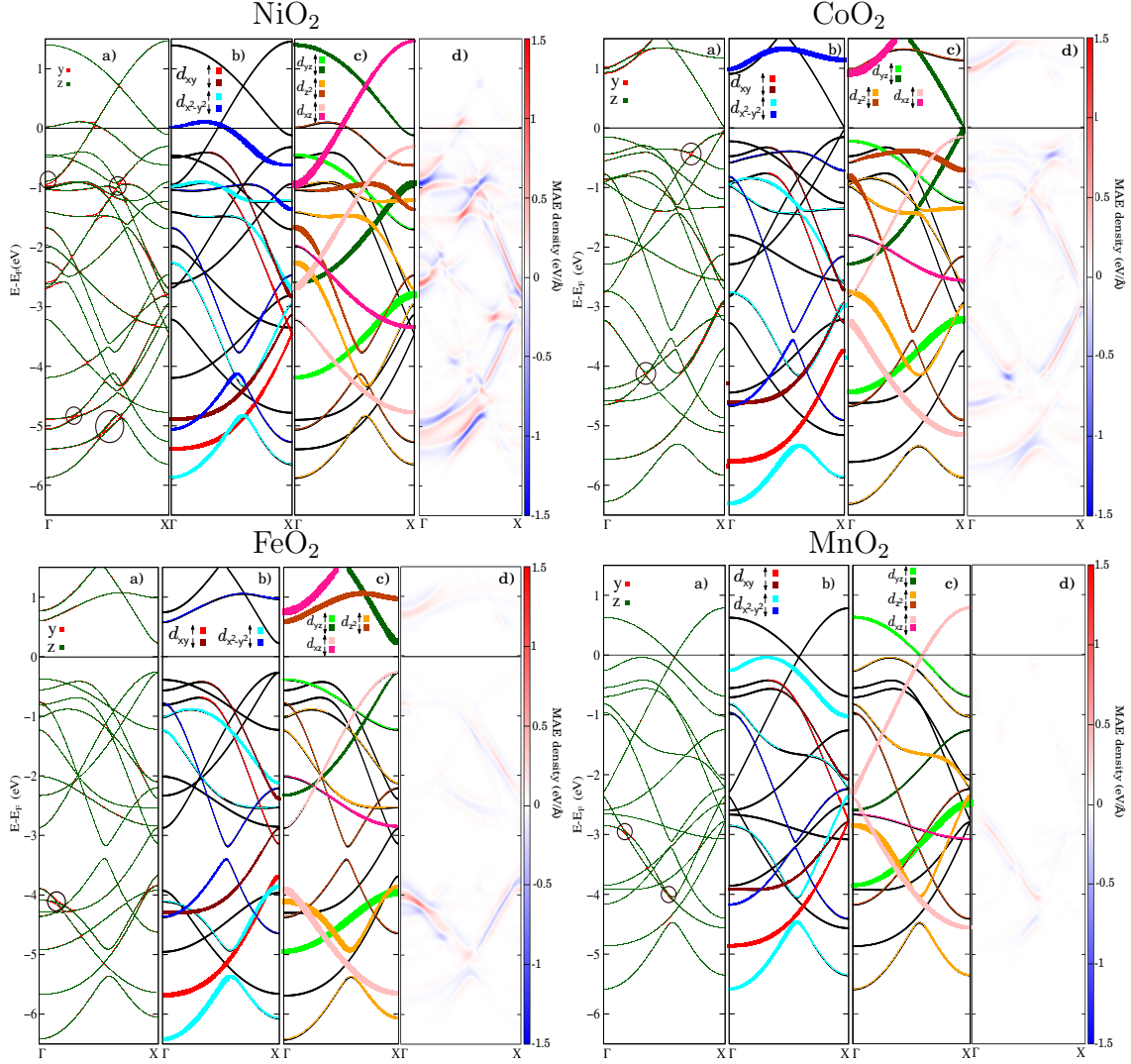


Figure 3.7: In all panels: (a) Electronic structure with SOC when the magnetization is aligned to the y -axis (red) or z -axis (green). The projected density is separated into in-plane orbitals (b) and out-of-plane orbitals (c). (d) MAE density, the contribution of each colored points is as follows: red for z -axis and blue for y -axis, the density varies from -0.8 eV/\AA (most saturated blue) to 0.8 eV/\AA (most saturated red).

Finally, the magnetic anisotropic energy has been obtained. We have found that NiO_2 and CoO_2 show an in-plane easy-axis perpendicular to the chain axis. The FeO_2 and MnO_2 show an out-of-plane easy-axis. The self-consistent and force theorem calculation methods agree on the sign prediction, but the magnitudes differ significantly for NiO_2 , where the FT approach fails to describe SOC effects adequately for band splittings at the Fermi level. The other chains show good

agreement. This study has shown that the easy-axis variation of the chains can be related to the occupancy of specific d orbitals. In particular, CoO_2 shows an occupied d_{2^2} band that contributes to the in-plane easy-axis. This latter band is unoccupied for FeO_2 and MnO_2 , resulting in an out-of-plane easy-axis.

Chapter 4

Electronic correlation and multiplet effect in TMO chains

*I wish I could,
but I don't want to.*

Phoebe Buffay, *Friends*

4.1 Introduction

Strong Coulomb interaction can give rise to high- T_C superconductivity [151], colossal magnetoresistance [152], ferroelectricity etc. [153, 154, 155]. Magnetic materials with d and f orbitals localized in the atom show the need to include interactions within these orbitals.

The study of correlated materials is a challenging research area, as it implies a many-body problem. Experiments have shown that some transition metal compounds have an insulating character, while the orbital shell is incomplete, a hint of a metallic behavior [92]. N.F. Mott [91] described the insulator state in the correlated materials using the Hubbard Hamiltonian [71]. Not all strongly correlated materials display an insulating behavior; compounds that show a metallic behavior do exist, e.g., V_2O_3 at high-temperature [156]. The latter systems are out of the scope of the description given by the Mott-Hubbard theory. Zaanen, Sawatzky and Allen developed a model (ZSA model) where the insulator gap and

metallic behavior could be described in terms of the charge transfer energy (Δ_{CT}), the bandwidth (W) resulting from hybridization and intraorbital Coulomb interactions modeled by a Hubbard- U parameter. Within this theory, both metallic and insulating states can be obtained in compounds with elements with strong electronic interactions (see Fig.3 in [157]). The ZSA model allows to distinguish two types of insulating states: the Mott insulator where the band gap is determined by U (e.g. MnO [158]) and the charge-transfer (CT) insulator where the gap is defined by Δ_{CT} (e.g., NiO [158, 159]).

The Hubbard- U describes the effective screening due to the surrounding environment inside the localized orbitals. Thus, its effective value will be dependent on hybridization. As the number of atoms surrounding the correlated atom increases, the effective screening is enhanced. Therefore, dimensionality can drastically change the value of U [127]. The Coulomb interaction can be strongly damped in bulk and interfaces where the U value can drop from tens of eV to a few eV [160, 161]. Coulomb interaction in finite-size low dimensional clusters can even show non-conventional phenomena, such as antiscreeing, i.e., the induced polarization from the other systems increases the electron interaction [162, 163].

DFT is a one-electron framework where interactions within orbitals cannot be adequately described. For instance, it predicts an incorrect metallic behavior in FeO and CoO compounds [164, 158]. The DFT+ U technique can provide better results for systems with localized states (see Section 2.2 for a more detailed discussion). Other theoretical methods that go beyond DFT have been developed to treat many body-interactions, such as, GW[165, 166], LDA++[167], MP2[168], RPA[169] and DMFT [170, 171, 172], but these methods can be computationally demanding. The DFT+ U is a computationally inexpensive technique compared to the latter methods, so it can be used as a first step before going beyond-DFT methods. However, in order to use DFT+ U an adequate value of U needs to be set in order to obtain accurate properties of materials, for instance, in the direct exchange and superexchange the magnetic exchange constant (\mathcal{J}) is inversely proportional to the U parameter [145, 10]. The value of U can be obtained by combining Auger spectroscopy and X-ray photoemission spectroscopy [173, 174] using Herring's definition. According to Herring [175, 176] the U parameter is the sum between the ionization energy and electron affinity: $U = [E(d^{n+1}) - E(d^n)] + [E(d^{n-1}) - E(d^n)]$. Another possibility is to calculate suitable U and J by *ab initio* methods. Different first-principles methods have been developed for this, such as the constrained LDA (cLDA) method [117, 177], and others based on linear response theory [120]

or the constrained random-phase approximation (cRPA) [122, 119, 123]. In this Thesis, we use the cRPA to calculate the U and J parameters (see Section 2.4 for a detailed explanation of the method) in collaboration with G. Bihlmayer and C. Friedrich from the Peter Grünberg Institute and Institute for Advanced Simulation in Forschungszentrum Jülich and JARA.

In the previous chapter, we have studied the magnetic properties of the planar free-standing XO_2 chains. Fig. 3.3 shows that the modification of the U parameter does not alter the bond length, but it can trigger a spin state transition. A change in the Hubbard- U value can drive the NiO_2 chain from a non-magnetic to a magnetically polarized state. The dependence of the magnetic properties on the Hubbard- U show that adequate U and J parameters are needed. In this chapter, we calculate the U and J values for the ideal case of the planar isolated chain and the chain with substrate. In the $XO_2/Ir(100)$ system, the inclusion of the Ir atoms induces effects, such as, charge transfer to the TM atom and hybridization with the chains orbitals can modify the electron-electron interaction. Apart from the electronic structure screening, the cRPA allows to modify the source of the screening by varying the correlated space allowing to estimate the source of the screening.

This chapter is organized as follows: in Section 4.2, we describe the relaxation of the chain plus substrate system and the cRPA calculation setup. In Section 4.3, the ideal planar free-standing screened Coulomb interaction is calculated. The non-planar case is studied for the MnO_2 chain. Section 4.4 is devoted to the supported chains, where the effects of the Ir layers in the U and J are analyzed. Finally, in Section 4.5, we draw the conclusions of our research.

4.2 Computational details

$XO_2/Ir(100)$ geometry

The relaxed geometry of the planar free-standing chains has been obtained in the previous chapter (see Table 3.2). In this chapter, we will compare the ideal and supported cases. Therefore, we relax the geometry including the Ir substrate. The equilibrium geometry for the $XO_2/Ir(100)$ - 3×1 system is obtained considering five Ir layers, where the last layer is kept frozen during relaxation. We set the same convergence parameters as in the previous chapter (see Section 3.2), except for the k -grid, where we set $10 \times 3 \times 1$. The relaxed geometry is given in Table 4.1 for

$U = 1.5$ eV.

	NiO ₂	CoO ₂	FeO ₂	MnO ₂
z_O	1.32	1.34	1.31	1.39
z_X	1.19	1.17	0.89	1.12
d_{X-O}	1.85	1.90	1.96	1.90
d_{O-O}	2.56	2.64	2.63	2.62
Δ_{12}	1.87	1.84	1.84	1.84
Δ_{23}	1.98	1.99	1.99	1.99
Δ_{34}	1.84	1.84	1.84	1.84

Table 4.1: All lengths are given in Angstroms. The distance between the metal atoms is fixed by the Ir(100) lattice parameter $d_{\text{Ir-Ir}} = 2.71$ Å. The d_{X-O} and d_{X-X} are the interatomic lengths. The height (z) of the X and O atoms is measured from the topmost Ir layer. Δ is the averaged interplanar distance between the Ir layers. Bucklings and lateral displacements of individual Ir atoms, not shown, are of the order of 0.1 Å for the topmost layer and below 0.05 Å elsewhere.

cRPA calculations

The cRPA calculations were done using the SPEX code [128]. SPEX needs previously converged wavefunctions, obtained from DFT calculations done by the FLEUR code, based on the FLAPW method (see Section 2.2). In FLEUR, we use the GGA+ U with the PBE exchange-correlation functional. The + U correction is implemented as described by Shick *et al.* [98] within the fully-localized limit [100] to account for the double-counting correction. The specific setting of the convergence parameters of each chain is specified in Appendix B. In the unsupported case, we maintain the geometry obtained in the previous chapter with the same k -grid sampling. The supported system is sampled with a $10 \times 3 \times 1$ k -grid centered at Γ . Partial occupations and Fermi level have been determined by a Fermi-Dirac smearing with a 0.015 H width.

In SPEX, the polarization involves a summation over empty states. We use a total of 150 bands to calculate a converged sum. The convergence parameters of the cRPA method are specified in Appendix B. Maximally localized wannier functions (MLWFs) are used to build real-space localized states (see Section 2.5 for a theoretical background of the MLWFs) [132]. For the MLWFs construction

and cRPA calculations, a $10 \times 3 \times 3$ k -grid has been used ¹.

The screened Coulomb interaction is calculated for the $X(d)$ orbital. Therefore, the space spanned by the MLWFs should only contain the d orbital. In the unsupported case, the X and O atoms are hybridized (in Fig. 4.1 a small weight of $Mn(d)$ orbitals can be appreciated in the bands near Fermi level, which have a main $O(sp)$ orbital character). To avoid losing any contribution of the d orbital and obtain well-localized MLWFs, the localized space includes both X and O atomic orbitals. We consider 11 bands for the NiO_2 , CoO_2 , FeO_2 chains. The MLWFs are constructed with projections onto the $X(d)$ orbital, as well as $O(s, p_x, p_z)$ orbitals. In the MnO_2 chain there are degenerate states, around 6 eV, (see Fig. 4.1) that need to be included to obtain well-localized MLWFs. Therefore, in the case of MnO_2 , 13 bands that include the $O(p_y)$ orbitals are considered.

Because of the short screening length in metals, we consider that two layers will be sufficient to account for the screening due to the Ir substrate (to validate the latter assumption, we have also made a calculation using 3 layers, see Appendix B.2). Therefore, unless specified, only two layers are used in cRPA and FLAPW calculations. Fig. 4.1 shows a strong hybridization between chain and substrate. Hence, the Ir atomic orbitals are also included to construct the MLWFs. 41 bands are used with projections onto the p, d on the X atom, s, p on O atom and sp^3d on Ir atom. When Bloch states are projected onto the MLWFs basis, we ensure that the eigenstate character is approximately preserved. We calculate the projected electronic structure with FLEUR for the Bloch states and with SPEX for the MLWFs. In Fig. 4.1, we show the band structure for the unsupported and supported MnO_2 chains obtained with FLEUR and band interpolation done with MLWFs. The MLWFs orbital characters of the bands nicely match with the ones obtained by FLEUR.

The U values are obtained by calculating how the polarization of the rest of the space² affects the bare Coulomb potential of the localized set. The localized space correlation is eliminated from the total polarization. In our system, the localized set is composed of a larger space than only the $X(d)$ orbitals. This requires that the projection of the d orbitals onto the MLWFs have to be singled out from the other contributions. The projection method allows to isolate the subset formed by

¹The k -points along the z axis are considered for the construction of the MLWFs. Setting $10 \times 1 \times 1$ or $10 \times 3 \times 1$ resulted in an impossibility to obtain adequate MLWFs, because of the lack of points in the y and z -axes needed to evaluate the derivatives using finite differences.

²States not included in the correlated space.

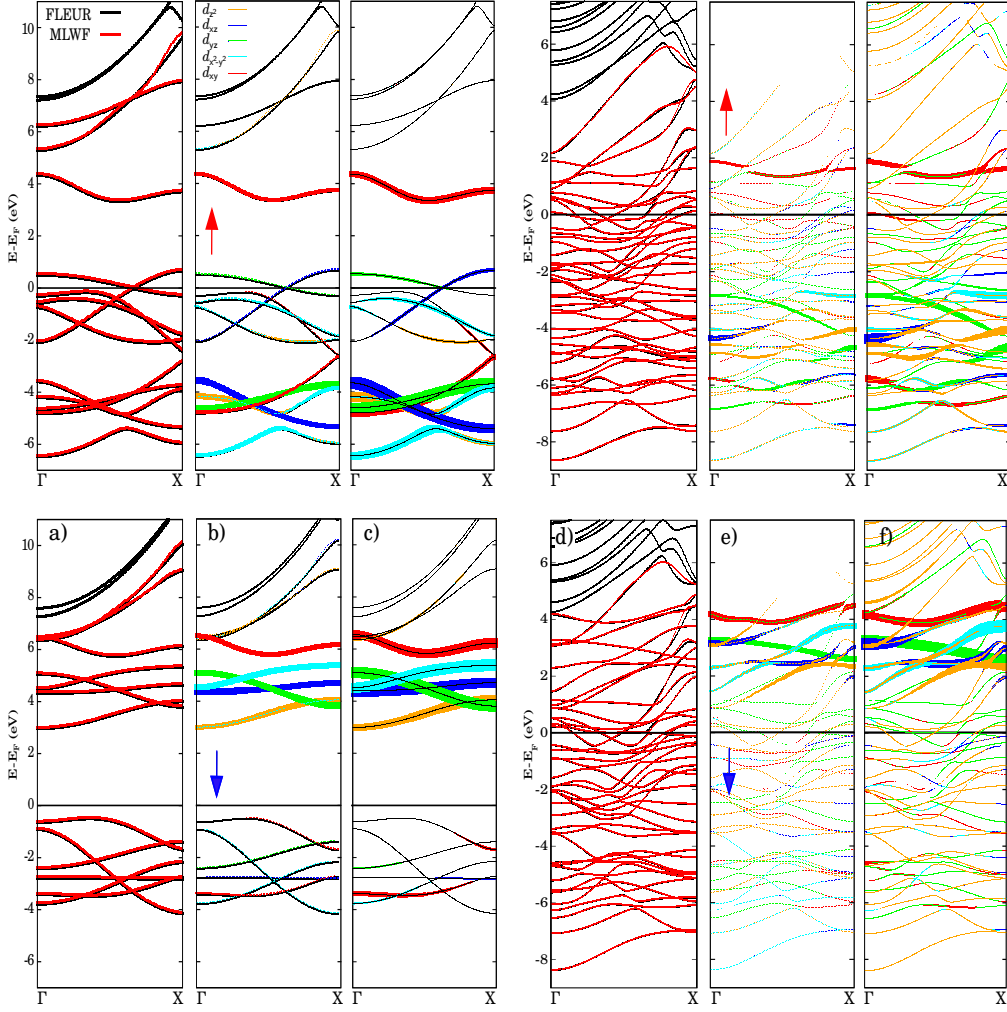


Figure 4.1: Panels (a), (b) and (c) correspond to planar free-standing chain and panels (d), (e) and (f) to the supported case. Panels (a) and (d) show the bands obtained by FLAPW (black) and MLWFs (red) interpolation. The (b) and (e) are the orbital weighted bands for the MLWFs, and the (c) and (f) for the FLEUR calculation. The size of the curves is proportional to the magnitude of the projection. Arrows indicate spin up/majority (red) and spin down/minority (blue).

the $X(d)$ -like MLWFs from the whole localized set and obtain the localized subset polarization using Eq. (2.57). In Fig. 4.2, we show the MnO_2 band structure along with the probability ($p_{\mathbf{k}m}$) of the electron to be in a certain m state at a given k -point using Eq. (2.55) for the whole localized space and for the d orbitals subset. In Fig. 4.2 we use squares to visualize the probability: when the whole localized set is considered, the squares have all the same size ($p_{\mathbf{k}m} = 1$), while when calculating $p_{\mathbf{k}m}$ for the d subset the size is smaller ($p_{\mathbf{k}m} < 1$) for bands with Mn and O orbitals

mixed character.

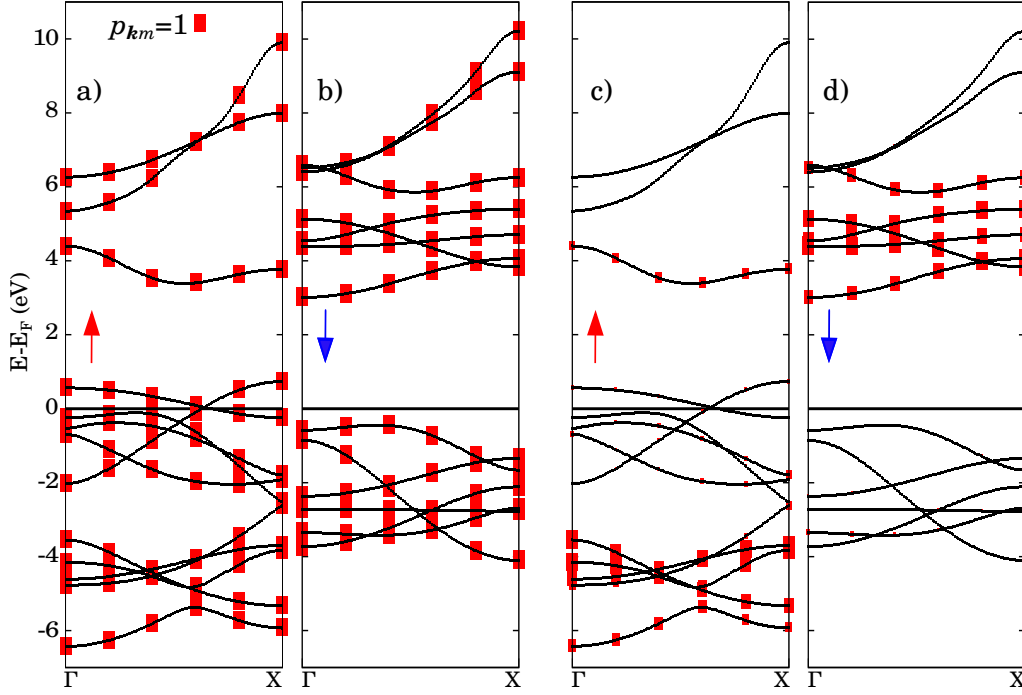


Figure 4.2: Probability $p_{\mathbf{k}m}$ of the localized space in MnO_2 chain. Pannels (a) and (b), show the probability when the whole localized set of 13 bands is considered, pannels (c) and(d) when d orbitals formed subset is chosen. The size of the square indicates the value of the probability ($p_{\mathbf{k}m}$). Bands are obtained by MLWFs interpolation. Arrows indicate spin up/majority (red) and spin down/minority (blue).

The U and J values are obtained by spherical averaging of the interaction matrix elements in the static limit $U_{mm'nn'}^{\alpha\beta}(\omega \rightarrow 0)$, previously defined in Eq. (2.59). We follow the workflow of Fig. 2.6 with the convergence criterion of $\Delta U = |U_{\text{new}} - U_{\text{old}}| < 0.05$ eV.

4.3 Planar free-standing XO_2 chains

The isolated chain model allows to study the screened Coulomb interaction arising only due to the bonding to O atoms. We set $U_0 = 5.5$ eV and $J_0 = 0.0$ eV as initial guess values to calculate the one-electron wavefunctions in FLEUR. With them, obtain the new U and J values with SPEX.

The U and J values are calculated for the spin channels $\uparrow\uparrow$, $\uparrow\downarrow$ and $\downarrow\downarrow$. Note that $\uparrow\downarrow$ will yield the same result as $\downarrow\uparrow$ ³. About 4-5 cycles are needed to obtain convergence. In Table 4.2, we give the results for the $\uparrow\uparrow$ channel. We find that the U and J values are rather insensitive to the selected spin channels (we tabulate the value of U and J for different spin channels in Appendix B). To check if the obtained values depend on our initial guess we have also considered other starting values, namely, $U_0 = 3.5$ and 7.5 eV, which tend to converge to the same U and J , except the NiO_2 , which will be discussed separately. The interorbital interaction, J , does not show a significant variation. Differences are ≤ 0.2 eV for the different compounds. The Hubbard parameters can be interpreted with the Slater integrals, where the intraorbital parameter is $U = F^0$ and, for the d orbital, the interorbital exchange is $J = \frac{1}{14}(F^2 + F^4)$ [175, 178, 96]. The F^2 and F^4 are slightly affected by screening effects, maintaining an almost constant J value [175, 179, 161].

The U values of CoO_2 , FeO_2 and MnO_2 range from 5.73 eV to 7.67 eV (see Table 4.2). The FeO_2 one shows the highest value compared to the other chains. Electronic structure calculations show that this system is an insulator while the others are half-metallic (see Fig. 4.3). Metals have a shorter screening length than insulators, agreeing with FeO_2 showing a larger U value.

XO_2	U	J	\tilde{U}
Ni (C1)	6.59	1.17	8.45
Ni (C2)	2.41	1.01	7.03
Mn	6.21	1.04	6.57
Co	5.73	1.11	8.62
Fe	7.67	1.13	9.06

Table 4.2: Converged U and J values ($\uparrow\uparrow$ spin channel) for the planar free-standing XO_2 chains. The \tilde{U} is the result when the shell-folding method is used. All units in eV.

The NiO_2 shows a distinct behavior from the rest. Two different $\text{Ni}(d)$ orbital configurations are converged depending on the starting U_0 . We label them C1 and C2. These configurations are maintained throughout consecutive FLAPW and cRPA cycles. If $U_0 \geq 4$ eV the resulting orbital configuration will be C1, and for $U_0 < 4$ eV C2 configuration is favored, with converged U values of $U = 6.59$ eV and $U = 2.41$ eV, respectively. The difference between C1 and C2 is the

³The average U value is the same, since matrices are conjugated transposes: $U_{mn;\uparrow\downarrow}^{\uparrow\downarrow} = (U_{\downarrow\uparrow;mn}^{\downarrow\uparrow})^\dagger$.

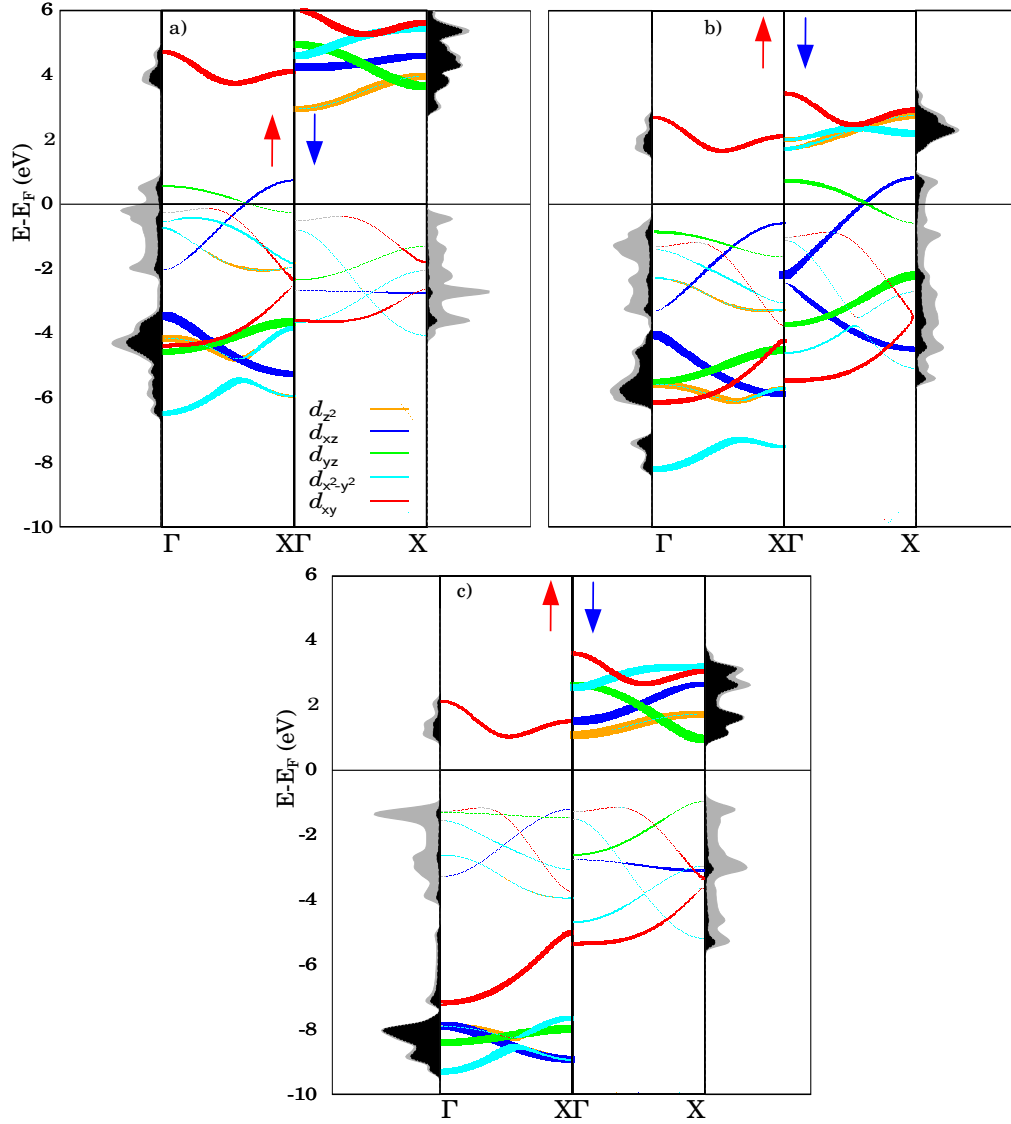


Figure 4.3: In each panel, central subpanels show the electronic structure of the planar unsupported chain, and on the sides the PDOS. (a) MnO_2 , (b) CoO_2 and (c) FeO_2 . Arrows indicate spin majority (red) and spin minority (blue). The d orbital character of the bands is plotted with a color code, where the thickness is proportional to the magnitude of the projection on each d orbital. d orbital PDOS is plotted in black, while full bands and the total DOS are plotted in gray.

occupation of the $\text{Ni}(d)$ orbital (see Fig. 4.5 for the band structure and PDOS for the C1 and C2 configurations). DFT+ U calculations show that the spin magnetic moment of each configuration is $\mu_{\text{Ni}}^{\text{C1}} = 1.23 \mu_B$ and $\mu_{\text{Ni}}^{\text{C2}} = 0.55 \mu_B$, respectively. C1 and C2 configurations can be considered as two multiplets of $S = 1/2$, i.e., two states with the same spin state but different orbital occupation configuration.

Nevertheless, the difference between the bare Coulomb parameters⁴ is just $V^{C1} - V^{C2} = 25.02 - 24.81 = 0.21$ eV, a 0.8% relative variation on the averaged matrix elements. A large variation on the bare Coulomb potential would indicate that the shape of the orbitals is altered depending on the configuration. A real space representation of the Wannier orbitals, shown in Fig. 4.4, assures that both C1 and C2 present almost no difference. The slight variations between the MLWFs can result in a small difference on the bare Coulomb parameters, but they can not explain the large variation of U . C1 and C2 screening difference is the result of the different Ni(d) orbital occupancy and, consequently, different electronic structures (see Fig. 4.5).

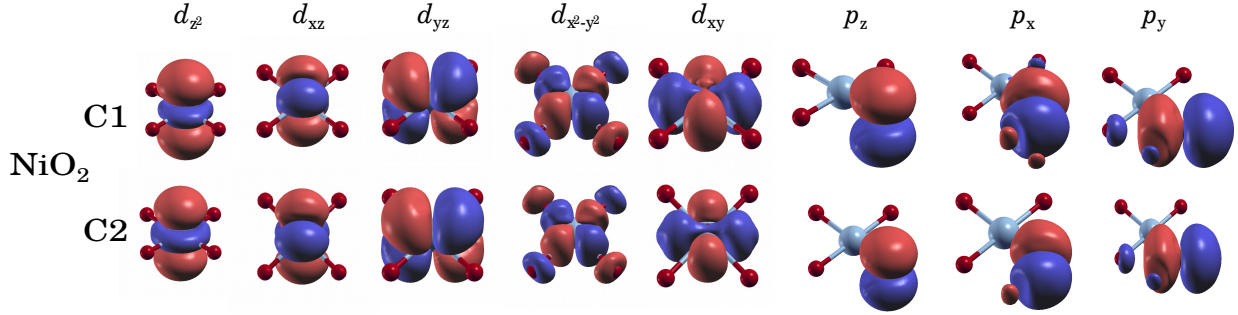


Figure 4.4: Real space representation of the unsupported chains MLWFs of the spin minority Ni(d) and O(p) orbitals.

To obtain insight into the effective screening, we modify the subset where the screened interaction is calculated. In Fig. 4.6, we show the matrix elements U_{mn} ⁵ for the $\uparrow\uparrow$ spin channel. We recall that the subset correlation is excluded. In consequence, if we include O(s) [O(p)], the origin of the effective screening will be due solely to O(p) [O(s)]. Only bands that lie deeply in energy have $X(s)$ and $X(p)$ orbital weight in the muffin-tin. Therefore, we assume that the screening effects from these orbitals are negligible.

The matrix elements shown in panels (a) and (d) in Fig. 4.6 consider only the d orbitals subset, hence, screening is due to O(sp). In the following panels, the combined effect of O(s) and O(p) is separated. For (b) and (e) is due to O(p), for panels (c) and (f) only to O(s). As a reference, we also show the bare Coulomb matrix elements of Ni(d), O(s) and O(p) of C1. When the O(p) orbital is considered as the

⁴Average of the electron interaction without screening: $V_{m_1 m_2 m_3 m_4} = \langle m_1 m_2 | \frac{1}{|\mathbf{r} - \mathbf{r}'|} | m_3 m_4 \rangle$.

⁵We use contracted indices notation: $U_{mn;mn} \rightarrow U_{mn}$.

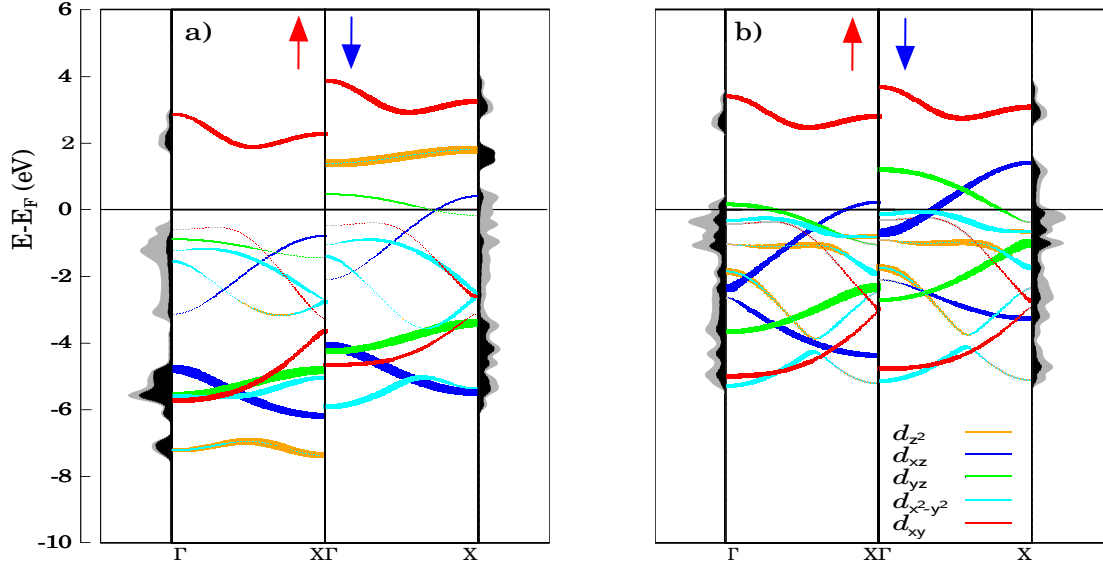


Figure 4.5: Same information as in Fig. 4.3. The free standing NiO_2 is shown in panels (a) C1 and (b) C2.

origin of the screening, and similarly with the $O(sp)$ combined effect, the averaged $U(d, d)$ ⁶ parameter is 6.70 eV in C1 and 2.61 eV in C2. Nevertheless, $O(s)$ is not to be overlooked, as the $O(s)$ reduces the U from 25 eV to 15 eV in the C1 state and to 10 eV in the C2. From these results, we can conclude that the combined effect of $O(sp)$ on $Ni(d)$ is not a sum of the individual terms of the $O(s)$ and $O(p)$ orbitals. The $O(p)$ orbital is the main source of the screening on the d orbital for C1 and C2. Still, in C2, the $O(p)$ orbital shows a larger efficiency in the screening. This indicates that $Ni(d)$ - $O(p)$ interaction differs for the C1 and C2 configurations.

The PDOS and band structure (see Fig. 4.5) of the chain shows features arising from the different $d - p$ bonding of each multiplet state. According to Eq. (2.57), in the static limit ($\omega \rightarrow 0$) the main contribution to the polarization are the states around the Fermi level [127]. Therefore, the larger the density of states at Fermi level, $\rho(E_F)$, the more effective the screening. The multiplets show different electronic structures: C1 presents a half-metallic state, where the band-gap is at majority spin, and d_{xz} and d_{yz} states are fully occupied, while C2 is metallic. These findings agree with the obtained results, where C1 has a larger U than the metallic C2. In addition, the C2 configuration presents sharp peaks around the Fermi level. The band narrowing in C2 enhances the electronic polarization, which in turn can reduce the U value even more [127].

⁶With $U(d, d)$ we refer to the matrix block formed by the d orbital.

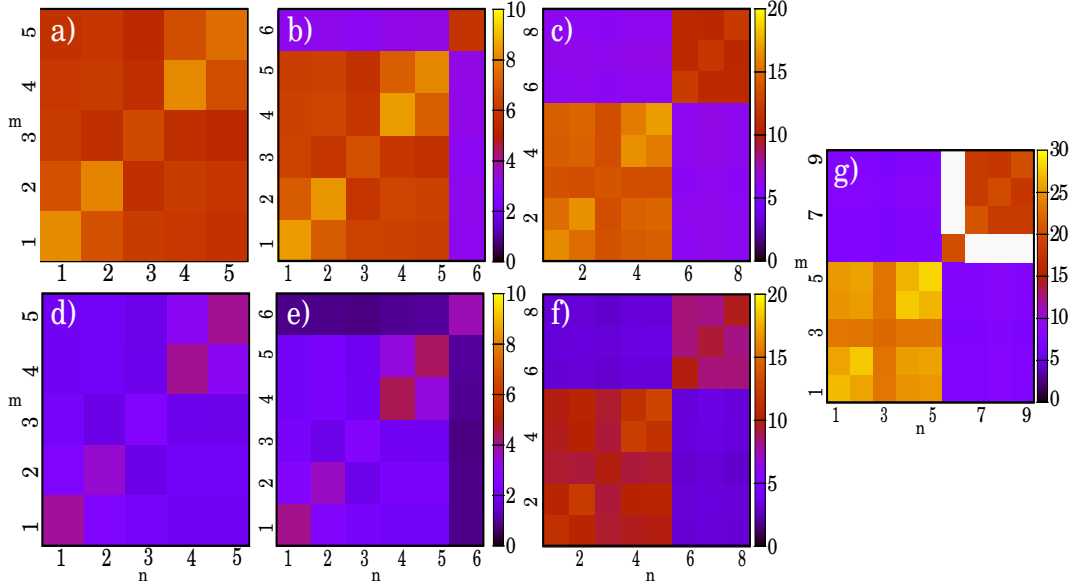


Figure 4.6: $U_{mn}^{\uparrow\uparrow}$ matrix elements for the screened orbitals. The indices indicate the orbitals, ordered as 1- d_{z^2} , 2- d_{xz} , 3- d_{yz} , 4- $d_{x^2-y^2}$, 5- d_{xy} for the Ni and 6- p_z , 7- p_x and 8- p_y for the O atom. In panels (a) and (d) the subset is formed with Ni(d), in (d) and (e) with the Ni(d) and O(s) and in (e) and (f) with the Ni(d) and O(p). As a reference the bare Coulomb matrix (C1 configuration) is included (panel g). Color code units in eV

Bands with d_{xy} character show a similar splitting and localization in energy in both multiplets. The main difference between C1 and C2 is at bands with d_{z^2, x^2-y^2} character⁷. According to Table 4.3 in C1 the $d_{z^2, \downarrow}$ is empty. In C2 the d_{z^2, x^2-y^2} orbitals are fully occupied. In the C2 configuration, the Ni and O atom orbitals are more hybridized around the Fermi level than in C1, where there is almost no mixing between Ni(d) and oxygen orbitals in the majority spin (see PDOS in the Fig. 4.5). The change in the hybridization suggests that the Ni(d) and O(p) interact in a different manner in the C1 and C2 configurations. The ligand field difference of C1 and C2 is reflected in the charge transfer between O and Ni atom: in C2 PDOS peaks at $E_F - 1$ eV indicate a $d-d$ character band gap (meaning that $U < \Delta_{CT}$), while in the C1 the band gap is formed between Ni(d) – O(p) orbitals (i.e., $U > \Delta_{CT}$) [157].

⁷The chain symmetry favors the formation of the sp^3d^2 hybrid orbital, where d_{z^2} and $d_{x^2-y^2}$ orbitals are hybridized.

Next, we estimate the correlation energy with:

$$E_U = U \sum_i n_i^\uparrow n_i^\downarrow \quad (4.1)$$

where $n_i^{\uparrow(\downarrow)}$ are the individual orbital occupations in Table 4.3. The latter estimation shows the trend of the U values depending on the orbital occupation. The results for $\sum_i n_i^\uparrow n_i^\downarrow$ and E_U are given in Table 4.4⁸. C2 shows a larger $\sum_i n_i^\uparrow n_i^\downarrow$ than C1, suggesting that U should be lowered in order to minimize the energy, in agreement with our results. Note, however, that Eq. (4.1) results can not be used as a criterion to define which configuration is more stable, as DFT+ U total energies for different U values can not be compared. Only for $U \simeq 6$ eV and $J \simeq 1$ eV both configurations have been converged, resulting in a C1 ground state while C2 is a metastable state separated by 0.33 eV.

	Spin	d_{z^2}	d_{xz}	d_{yz}	$d_{x^2-y^2}$	d_{xy}	μ_X (μ_B)
NiO ₂ : C1	↑	0.99	0.99	0.99	0.99	0.54	1.23
	↓	0.03	0.94	0.85	0.97	0.42	
NiO ₂ : C2	↑	0.99	0.91	0.86	0.99	0.48	0.55
	↓	0.99	0.64	0.61	0.99	0.46	
MnO ₂	↑	0.94	0.91	0.86	0.99	0.41	3.49
	↓	0.01	0.10	0.08	0.09	0.28	
FeO ₂	↑	0.98	0.98	1.00	1.00	0.59	3.67
	↓	0.01	0.21	0.14	0.11	0.49	
CoO ₂	↑	0.97	1.00	1.00	0.96	0.52	2.21
	↓	0.00	0.84	0.75	0.14	0.46	

Table 4.3: Individual occupations of the X(d) orbital of the unsupported chains. The spin magnetic moment is included to indicate the spin state.

Seth *et al.* [180] proposed another method to cope with the correlation when strong hybridization between the d and p . In Ref. [180], the "shell folding" (SF) method is proposed, where a renormalization of the U value is done to account for the screening due to the p ligand field. Within the shell-folding approach, the localized subset includes d and also p orbitals, resulting on off-diagonals elements in the Coulomb matrix that will account for the d - p interaction (see Fig. 4.6). Assuming that the total occupation of d and p orbitals is invariant over changes in

⁸Since d_{z^2} and $d_{x^2-y^2}$ form a hybrid atomic orbital⁷, we consider them a single orbital with double maximum occupancy.

	$n^\uparrow n^\downarrow$	E_U
NiO ₂ C1	3.98	26.2
NiO ₂ C2	5.09	12.3
MnO ₂	0.40	1.3
CoO ₂	2.11	12.1
FeO ₂	0.80	6.1

Table 4.4: $n^\uparrow n^\downarrow$ factors and correlation energy estimates E_U of free-standing chains.

the U , the resulting effective screening is calculated as $\tilde{U}(d, d) = U(d, d) - U(d, p)$, where $\tilde{U}(d, d)$ is the renormalized screening, $U(d, d)$ is the average value of the matrix elements of the d - d diagonal block (intraorbital interaction), and $U(d, p)$ is the average of the off-diagonal block. The resulting $\tilde{U}(d, d)$ are given in Table 4.5.

	$U(d, d)$	$U(d, p)$	$U(p, p)$	$\tilde{U} = U(d, d) - U(d, p)$	$\tilde{U} - U$
MnO ₂	12.24	5.67	9.96	6.57	0.36
FeO ₂	15.19	6.13	10.64	9.06	1.39
CoO ₂	14.84	6.22	11.08	8.62	2.89
NiO ₂ (C1)	14.61	6.15	11.26	8.45	1.86
NiO ₂ (C2)	10.31	3.28	8.77	7.03	4.62

Table 4.5: Screened Coulomb parameter using the shell-folding method for the planar unsupported chain. The U values indicate the averaged of block matrices dd , dp or pp . The fourth column is the result of the shell-folding renormalization (\tilde{U}). The last column indicates the difference between the shelf-folded \tilde{U} and the cRPA with projection method with only a d orbital subset. All values in eV.

For all unsupported planar chains, $\tilde{U} > U$ is obtained, as shown in Table 4.2. In the MnO₂ chain, the difference is $\tilde{U} - U = 0.36$ eV. This small difference between the two methods implies that the $d - p$ ligand contribution is correctly described, i.e., the correlated space is well separated from the rest of space. In NiO₂, we already mentioned that the p ligands do not interact in the same manner at the C1 and C2 configurations. The difference is $\tilde{U} - U = 1.86$ eV and 4.62 eV for C1 and C2, respectively. In the C2 configuration, the $d - p$ ligand contribution has a significant effect compared to the C1 one. The block average $U(d, p)$ for the NiO₂-C2 is 3.28 eV, which shows a large difference with respect to the other chains, where $U(d, p) \sim 6$ eV is obtained. The FeO₂ and CoO₂ chains are in-between the

limit behaviors of MnO_2 and NiO_2 -C2 chains.

Non-planarity in free standing chains

In the ideal case, metal and O atoms are coplanar, but as the X and O atom form the chain in an Ir(100) substrate, the O atoms are lifted. The non-planarity induces larger bonds between the X and O atoms, which alters the electron hopping and may affect the Coulomb interaction. To consider separately the effects of the adsorbed geometry in the substrate, we have done a cRPA calculation with the free-standing MnO_2 chains in the adsorbed buckled geometry. In Fig. 4.7, we compare the band structures of both unsupported MnO_2 chain.

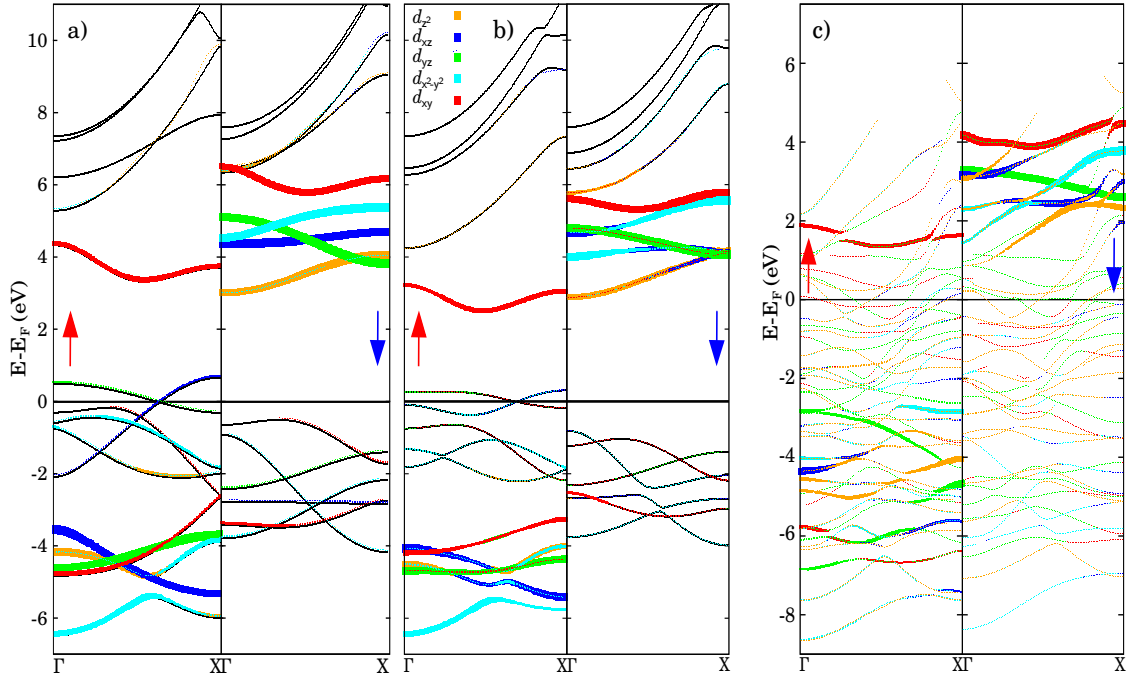


Figure 4.7: Band structure of the unsupported (a) planar, (b) absorbed geometry and (c) supported MnO_2 chain for majority and minority spins. Only Mn(d) projections are shown in this case. The d orbital projections color code is the same as in Fig. 4.5.

In the buckled geometry, the band dispersion is modified with respect to the planar chain, but the general aspects of the hybridization between the Mn and O atoms are maintained. For the buckled MnO_2 , the converged interaction parameters are $U = 6.18$ eV and $J = 1.04$ eV (in the $\uparrow\uparrow$ spin channel). There is a change of 0.03 eV in the intraorbital interaction, while there is no variation on the

interorbital exchange interaction. In the next section, we will study the screened correlation when the Ir substrate is included.

4.4 Supported XO_2 chains on Ir(100)

Charge transfer and orbital hybridization between substrate and chain can alter the electronic structure of the chains, which may, in turn, affect the screened Coulomb interaction. We have already seen that different orbital configurations with the same spin state yield different effective screenings, e.g., NiO₂ C1 vs C2, since the binding with O(*p*) is different in these cases. Hence, a contribution due to multiplet change can not be disregarded in our calculations.

The U value can be defined as the sum between the affinity and ionization energies. However, upon deposition of the oxide chains on metals, the interaction between the d orbitals is further screened by another term, $U = E(d^{n+1}) + E(d^{n-1}) - 2E(d^n) - 2E_{im}$, where E_{im} is the image potential originated from the ions creating a mirror charge in the substrate [160, 161]. However, this regime is not applicable here because the X atom is in a missing row, i.e., they are not on top of the substrate but *in* the substrate (see Fig. 3.1). Therefore, an approximation of the atom as a point charge with a Coulomb interaction tail of $1/|z - z_x|$, where z is the distance and z_x height of the X atom can not be considered.

In the supported case, the initial guess for U and J is set at $U_0 = 3.5$ eV and $J_0 = 0.0$ eV. The converged values of U and J for the supported chains are given in Table 4.6. All U values are reduced in comparison to the planar free-standing chain. In the FeO₂ chain, the effective screening is reduced by as much as ~ 6 eV compared to the free-standing case. The interorbital exchange coupling, J , is also smaller than in the unsupported case. The largest change is ~ 0.30 eV for the Fe atom.

Interaction between the Ir atoms and the chain is visible in the electronic structure of the chains (see Fig. 4.8). We begin by discussing the MnO₂ and CoO₂ chains, as they show a similar trend. Charge transfer from the substrate fills the partially occupied $d_{xz,\uparrow}$ and $d_{yz,\uparrow}$ bands in both chains and, in CoO₂, a partial filling of the $d_{x^2-y^2,\downarrow}$ can be observed near the Fermi level. In Table 4.7, we give the individual partial occupations of the supported chains.

XO_2/Ir	U	J	\tilde{U}
Ni	1.71	0.87	1.16
Mn	3.78	0.98	3.29
Co	2.39	0.90	
Fe	1.38	0.80	

Table 4.6: Converged U and J values ($\uparrow\uparrow$ spin channel) for the $XO_2/Ir(100)$ chains. All units in eV.

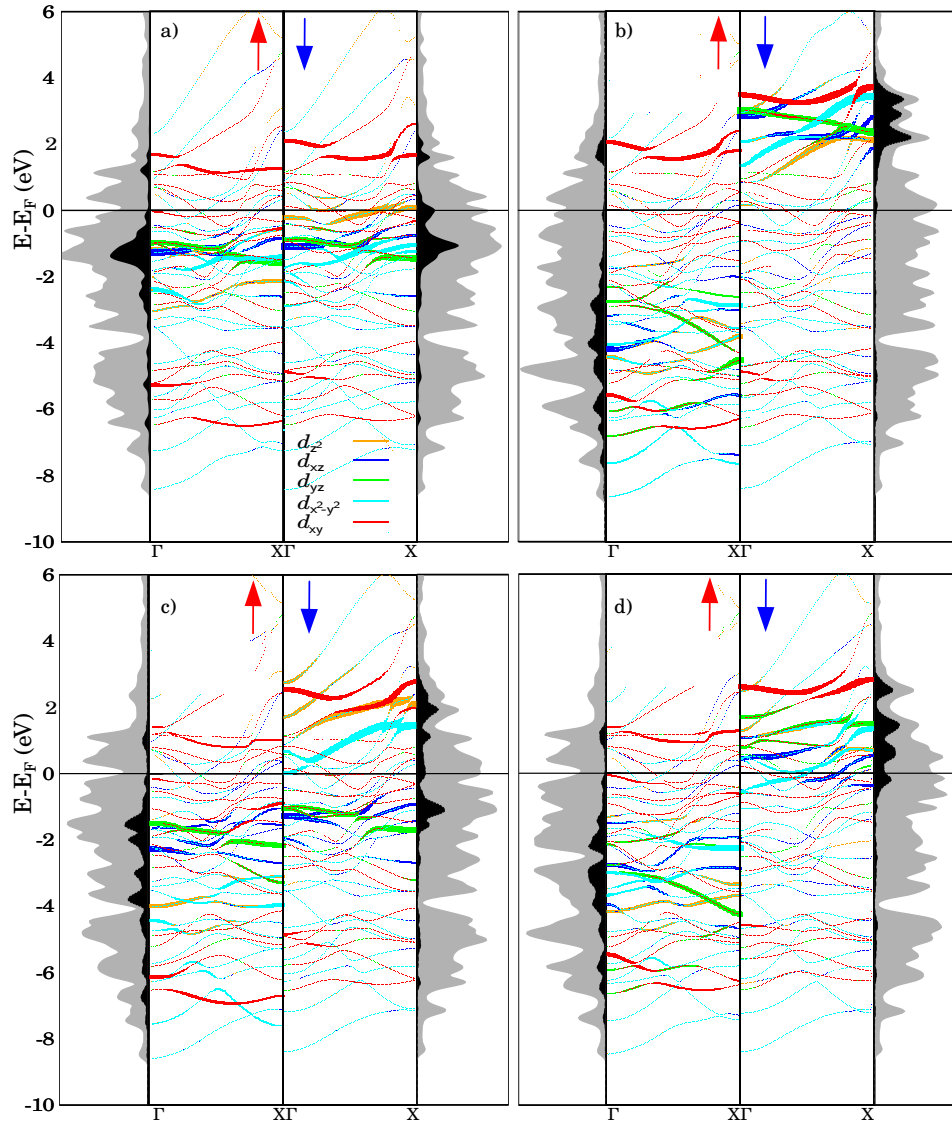


Figure 4.8: Same information as Fig. 4.3 for the supported (a) NiO_2 (b) MnO_2 , (c) CoO_2 and (d) FeO_2 chains.

	Spin	d_{z^2}	d_{xz}	d_{yz}	$d_{x^2-y^2}$	d_{xy}	μ_X (μ_B)
NiO ₂ /Ir	↑	0.97	0.95	0.95	0.97	0.62	0.52
	↓	0.59	0.94	0.95	0.96	0.41	
MnO ₂ /Ir	↑	0.96	0.98	0.98	0.99	0.41	3.66
	↓	0.08	0.08	0.08	0.09	0.23	
FeO ₂ /Ir	↑	0.95	0.97	0.97	0.98	0.68	2.87
	↓	0.25	0.41	0.17	0.36	0.28	
CoO ₂ /Ir	↑	0.97	0.96	0.96	0.98	0.70	2.02
	↓	0.08	0.93	0.94	0.29	0.31	

Table 4.7: Individual occupations of the $X(d)$ orbital in the supported chain. The spin magnetic moment is shown too.

	$n^\uparrow n^\downarrow$	E_U (eV)
NiO ₂ /Ir	5.08	8.7
MnO ₂ /Ir	0.61	2.3
CoO ₂ /Ir	2.74	6.5
FeO ₂ /Ir	1.93	2.7

Table 4.8: $n^\uparrow n^\downarrow$ factors and correlation energy estimates E_U for the supported chains.

Using Eq. (4.1) to estimate the correlation energy, the $\sum_i n_i^\uparrow n_i^\downarrow$ factor shows a subtle increase (see Table 4.8), consistent with the U values decrease as indicated in Table 4.6. The study of individual occupancies shows that the multiplet configuration of the MnO₂ and CoO₂ is maintained upon deposition. Even the magnetic moments are similar to those of the unsupported chain.

Next, we apply the shell-folding method, where all screening processes due to the O(sp) are eliminated, leaving only the Ir substrate, i.e., the localized subset is formed by the $X(d)$ and O(sp). The obtained matrix elements for MnO₂ are plotted in Fig. 4.9. The renormalized \tilde{U} value yields 3.29 eV, similar to the value obtained including O(sp) orbitals in the screening, $U = 3.78$ eV. The small difference (~ 0.5 eV) between shell folding and our method implies that d - p bonds are disentangled as in the free-standing case. In Fig. 4.9, we compare the matrix elements obtained for the MnO₂ and MnO₂/Ir(100). In panels (a) and (b), we show the planar unsupported case where the O(p) is the main source of the screening.

In the supported case (panels (c) and (d)), there is only a small change when the $O(sp)$ is taken out, implying that Ir is the main source of screening.

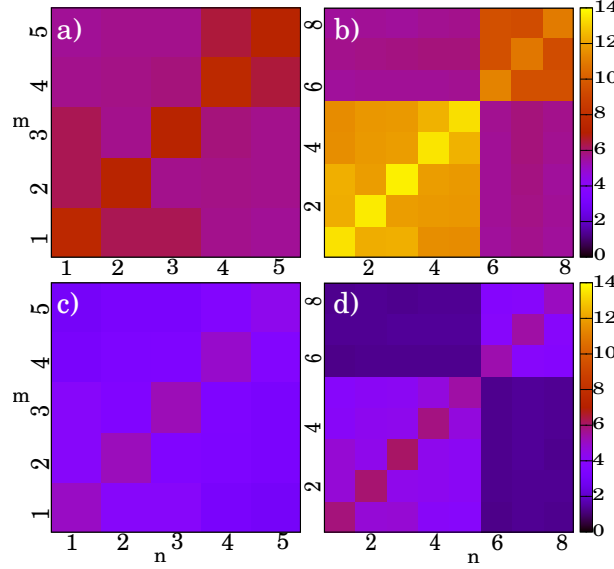


Figure 4.9: Screened Coulomb matrix elements for MnO_2 and MnO_2/Ir . Panel (a) is only for the unsupported $Mn(d)$ orbital, (b) considers the unsupported $Mn(d)$ and $O(p)$ orbital formed subset. Panels (c) and (d) show the same orbitals as panels (a) and (b) for the supported case. The (d) panel orbitals includes the $O(s)$ orbitals in the subset, its matrix elements are not shown. The numbering follows the same code as in Fig. 4.6. All units in eV.

The NiO_2/Ir chain shows a similar trend as CoO_2 and MnO_2 chain on the orbital filling: d_{xz} and d_{yz} become occupied by charge transfer, but in this case the $d_{z^2, x^2-y^2, \downarrow}$ becomes partially occupied (see Table 4.7). All states of $Ni(d)$ form narrow bands around the Fermi level and $E_F - 2$ eV, resembling the narrow peaks present in the C2 configuration. In addition, as given in Table 4.8, the $\sum_i n_i^\uparrow n_i^\downarrow$ factor differs by only 0.01 and the spin magnetic moment by $0.03 \mu_B$ from the free-standing C2 configuration. Hence, we consider that upon deposition a similar state as the C2 is settled for the Ni atom. The converged low value of $U = 1.71$ eV can be considered an effect of the further screening of the Ir to the NiO_2 -C2, which already shows a substantial screening. Thus, the multiplet state plays an important role on the obtained U value.

A comparison with the C1 value would be interesting, but it is not obtained in the adsorbed NiO_2 chains, neither as a ground state nor as a metastable state for the studied U parameter range ($U_0 = 1.5, 3.5$ and 5.5 eV). All calculations ini-

tializing with the orbital configuration of C1 are driven to the similar C2 ground state, yielding the same converged U and J values. We calculate the *shell-folded* interaction for the NiO_2 , being $\tilde{U} = 1.16$ eV. The difference between the d formed correlation space U value and \tilde{U} is ~ 0.6 . The $\text{Ni}(d) - \text{O}(p)$ ligand field is effectively well described when the chain is on the substrate, owing to a change in the $d - p$ interaction due to the Ir.

Note that in the unsupported chains the shell-folded method yields $\tilde{U} > U$, while in the supported case, $\tilde{U} < U$. This implies that Ir layers also modify the p orbitals of the O atoms (see Fig. 4.10). In the supported case, the Ir substrate effectively screens both X and O atoms. The real space representation of the MLWFs shows that including the substrate can indeed affect the shape of the orbitals.

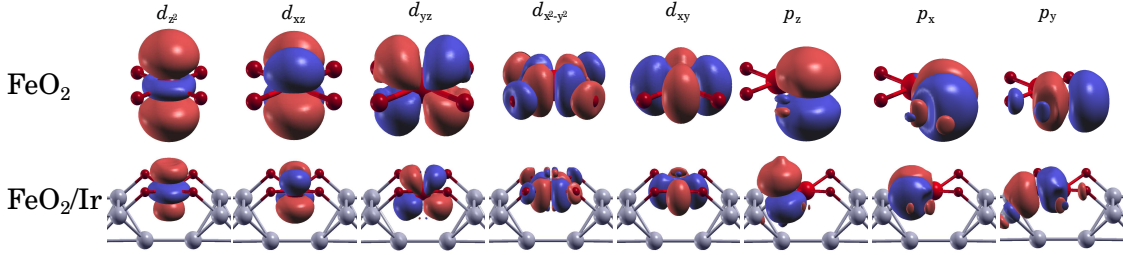


Figure 4.10: Real space representation of the minority spin MLWFs in the FeO_2 and FeO_2/Ir chain. Second and bottom rows show the unsupported and supported FeO_2 chains, respectively.

	$U(d, d)$	$U(d, p)$	$U(p, p)$	$\tilde{U} = U(d, d) - U(d, p)$	$\tilde{U} - U$
$\text{MnO}_2/\text{Ir}(100)$	4.66	1.37	4.34	3.29	-0.49
$\text{NiO}_2/\text{Ir}(100)$	1.99	0.83	1.26	1.16	-0.55

Table 4.9: Screened Coulomb parameters using the shell folding method for the supported MnO_2 and NiO_2 chains. The distribution of the table follows Table 4.5. All values in eV.

Finally, the FeO_2/Ir system is discussed. The converged intraorbital value shows a drastic enhancement of the effective screening compared to the isolated chain case, $U = 1.38$ eV, which is a reduction of more than 6 eV. The real-space representation of the MLWFs do not show major changes due to the substrate (see Fig. 4.10). Hence, the change in U needs to be due to other effects. In Table 4.8,

the sum over $n_i^\downarrow n_i^\uparrow$ increases by one unit compared to the ideal chain case. This increase is also reflected in the change of spin state, where the Fe atom changes from a $S = 2$ (unsupported case) to a $S=3/2$ state. The planar free-standing FeO_2 electronic structure shows the features of a CT insulator, i.e., a band gap between $X(d) - O(p)$ orbitals. However, in the supported case, the chain becomes metallic as spin minority d bands are located around Fermi. The drastic change in the U value can be associated with the insulator-to-metallic transition. We have checked that, despite varying the U value in the GGA+ U calculations, the minority d band is pinned at the Fermi level, and this could be driving the cRPA cycles to the low U values.

Considering the change of state and the large U variation, one could pose the question: in the limit of no hybridization with the substrate, what would be the screening? We artificially set it to two different heights: $z_{Fe} = 2.5 \text{ \AA}$ and $z_{Fe} = 4 \text{ \AA}$, measured from X atom in the absorbed geometry. At the same time, we consider two different initial U values: the converged free-standing value $U_0^f = 7.67 \text{ eV}$ and the converged absorbed one $U_0^s = 1.35 \text{ eV}$. In Table 4.10, we show the obtained U values for each calculation.

$z_{Fe} = 2.5 \text{ \AA}$		$z_{Fe} = 4 \text{ \AA}$	
$U_0^s = 1.35 \text{ eV}$	$U_2^s = 3.38 \text{ eV}$	$U_1^s = 3.18 \text{ eV}$	
$U_0^f = 7.67 \text{ eV}$	$U_2^f = 3.73 \text{ eV}$	$U_1^f = 6.13 \text{ eV}$	

Table 4.10: Resulting U values when the FeO_2 chain is lifted at $z_{Fe} = 2.5$ and 4 \AA starting from U_0^s or U_0^f . The subscript indicates the iteration number, and the $f(s)$ superscript indicates that the starting U value is the free-standing or supported.

The resulting PDOS are shown in Fig. 4.11. At the intermediate height of $z_{Fe} = 2.5 \text{ \AA}$, both cRPA calculations yield a $U \simeq 3.5 \text{ eV}$ after two iterations. In the the PDOS for $z_{Fe} = 2.5 \text{ \AA}$, the $d_{z^2, \downarrow}$ is pinned at the Fermi level for both starting values (panels (a) and (b)), and also a $d_{xy, \uparrow}$ for the U_2^f (panel (b)). This residual hybridization may contribute to reduce the Hubbard- U .

At height $z_{Fe} = 4 \text{ \AA}$, the first iteration of the cRPA results in $U_1^f = 6.13 \text{ eV}$ and $U_1^s = 3.81 \text{ eV}$ values, still far from the free-standing values. Fig. 4.11 panel (c) shows a small peak of $d_{z^2, \uparrow}$ and other d character peaks persist near E_F . For U^f (panel (d)) this pinning of the d_{z^2} vanishes becoming an empty orbital for both U values, but still an empty $d_{xy, \uparrow}$ is near Fermi. If we compare the free-standing FeO_2 PDOS (Fig. 4.3) with the lifted ones (Fig. 4.11), we see that at $z = 4 \text{ \AA}$,

panel (d), the PDOS is similar to the free-standing FeO_2 chain. The d orbitals peaks are at a similar energy range ($E_F - 8$ eV, $E_F - 10$ eV), except for the $d_{xy,\uparrow}$ which is situated near the Fermi level instead of $E_F + 1$ eV.

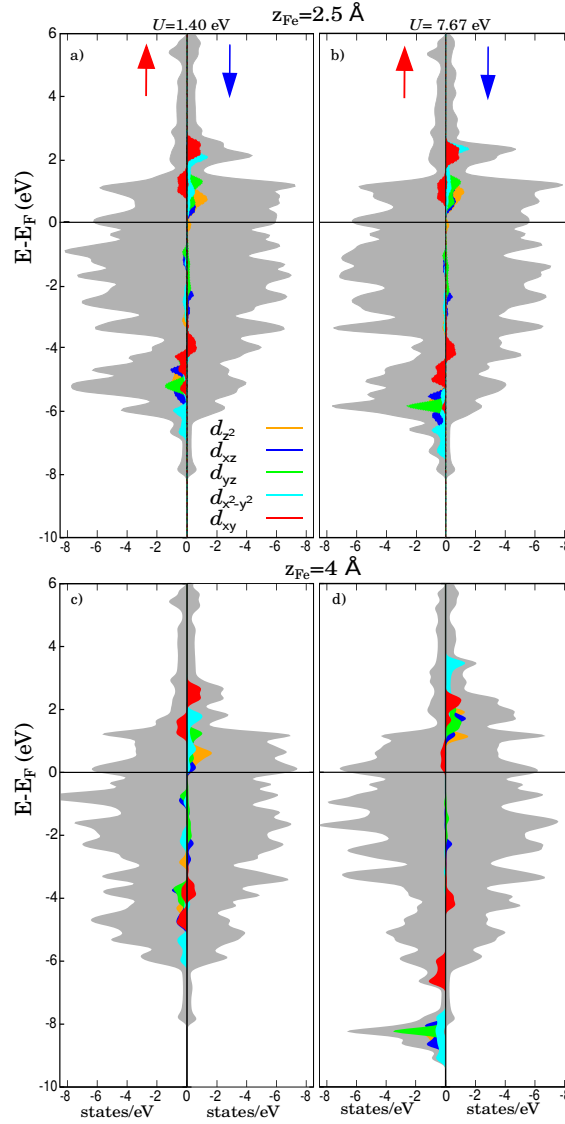


Figure 4.11: The colored curves show $\text{Fe}(d)$ orbital contributions to the PDOS of FeO_2 detached from the $\text{Ir}(100)$ substrate at heights 2.5 \AA (a,b) and 4 \AA (c,d), for $U_0^s = 1.40$ and $U_0^f = 7.67$ eV, which correspond to the limit U values in the adsorbed (a,c) and free standing (b,d) configurations, respectively. The gray curve corresponds to the total DOS.

The artificial lifting of the chain cannot reproduce the free-standing U value, even though hybridization between substrate and chain is almost completely lost

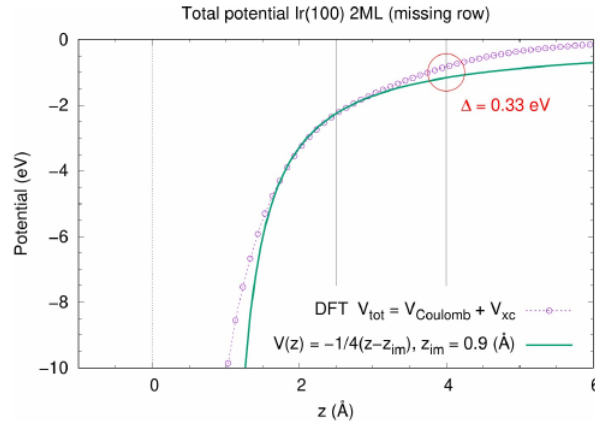


Figure 4.12: Total potential of the bare Ir surface compared with an image potential. z_{im} is set to match the derivative of both curves. Solid grey lines mark the $z = 2 \text{ \AA}$ and $z = 4 \text{ \AA}$ positions.

in the $z = 4 \text{ \AA}$ and U_0^f . The still present long-range screening effect is the effect of a still present non-negligible screening. In Fig. 4.12, we compare the total potential of the bare Ir substrate, i.e, no chains with an image potential. We see that the GGA total potential decays exponentially compared to the $1/z$ tail. At $z = 4 \text{ \AA}$ the GGA has a small value of $\sim 1 \text{ eV}$, which is 0.33 eV smaller than that of the Coulomb-like tail. Therefore, the obtained orbital pinning and screening can be physically possible, albeit, not accurate numerically.

4.5 Conclusions

In conclusion, DFT+ U and cRPA calculations are used to study the electronic correlation of $X\text{O}_2$ chains on Ir(100), where $X = \text{Ni, Co, Fe and Mn}$. We have calculated the U and J values of the free-standing planar and supported chains, with an analysis of the interplay between the ligand field and the substrate.

In the ideal case of the planar free-standing chains, we obtain U values ranging from 2.4 to 7.7 eV , being the largest value that of the insulator FeO_2 chain. DFT+ U calculations show the existence of two different multiplets for the same spin state in NiO_2 : C1 and C2 configurations, which C1 can be associated to a $d-d$ gap, ($U < \Delta_{\text{CT}}$), and C2 is a $d-p$ one ($U > \Delta_{\text{CT}}$), where Δ_{CT} is the charge-transfer energy. Each configuration shows a different U value. Calculations with the shell folding method result in higher values of the U for all chains. These calculations show that each $\text{Ni}(d)$ multiplet interacts differently with the $\text{O}(p)$ orbital depending on the orbital configuration. Calculations varying the correlated space

show that the $O(p)$ is the main source of screening. The non-planar geometry of the chain modifies the band structure, but the U value is slightly affected.

All supported chains show an increased effective screening as expected. The FeO_2/Ir shows an insulator-to-metallic transition, which strongly enhances the screening reducing the U from 7.7 eV to 1.38 eV. The Ir substrate also can modify the d orbital configuration due to charge transfer which can contribute to the screening. The shell folding method allows to estimate the ligand field contribution to the U value, showing that the $X(d)$ - $O(p)$ bonding is different between the unsupported and supported case. An artificial lifting of the FeO_2 chains from the substrate cannot reproduce the free-standing U value. Screening due to Ir is present in the detached chain limit, total potential calculations that an appreciable long-range interaction tail is still present in the calculations.

Chapter 5

Magnetic properties of transition metal-organic chains: the CoQDI and CrQDI cases

They don't know that we know
they know we know.

Phoebe Buffay, *Friends*

5.1 Introduction

In this chapter, we deal with metal-organic chains, i.e., a type of chain where transition metal (TM) atoms are linked by organic ligands. This type of system can be formed on surfaces through self-assembly [42].

The large amount of accessible molecular complexes allows the synthesis of different metal-organic networks. This type of networks are formed by many atoms leading to a high number of spatial degrees of freedom, combined with the spin makes the metal-organic system capable of displaying different possible geometries, and in consequence, they can show different magnetic and electronic properties [25, 181, 182, 183]. Occasionally, they show a spin-crossover (SC) transition [26], where the TM atom can switch from a low-spin (LS) state to a high-spin (HS) state due to an external perturbation, such as, thermal effects, light, pressure or

high-magnetic fields. The SC can be used in pressure sensors, as data storage, devices electronic devices [184, 185, 186, 187] or may be applicable to holography, because of the different refractive indices of the LS and HS states [188].

In low-dimensional systems, where the electron correlation is enhanced, DFT+ U needs to be applied. The inclusion of the new term in the DFT functional (see Eq. (2.28)) adds an implicit bias in the DFT calculation, which becomes dependent on the orbital occupation matrix and the chosen double-counting term (see Section 2.2). In addition, the TM species can show different states (with the same spin or different), i.e., different orbital occupations. Recall that in the previous chapter the NiO₂ could show two different orbital occupations with the same spin state for different values of U , and both could be converged for a given U value. If the energy minimization procedure was exact, the obtained state would be the ground state (GS). However, this numerical minimization procedure can converge to metastable states [72, 189, 190]. The orbital occupation can affect the magnetic anisotropy and exchange coupling. In order to study the properties of both the GS and metastable states, we use the occupancy matrix control (OMC) method [73] (see Section 2.2).

This chapter focuses on the CrQDI and CoQDI 1D polymeric chains, transition metal-organic chains that result from the combination of 2,5-diamino-1,4-benzoquinonediimines (2HQDI) with Cr and Co atoms (see Fig. 5.1 for the structure). The research group of Prof. P. Jelinek from the Czech Academy of Science in Prague synthesized these chains on an Au(111) surface in ultra-high vacuum conditions, forming well-ordered long chains (> 100 nm). The structural properties of the chains have been previously analyzed by V. M. Santhini *et al.* [75] using atomic force microscopy and scanning tunneling microscopy. The experimental data on the magnetic properties of these chains have been obtained by C. Wackerlin *et al.* from the Swiss Federal Laboratories for Materials Science and Technology in collaboration with the group of Prof. P. Jelinek using X-ray absorption spectroscopy combined with X-ray magnetic dichroism (XAS/XMCD) and linear dichroism (XAS/XLD) [6].

In our work, we study the possible states in the CoQDI and CrQDI chains, ground state and metastable, and the consequences that these may have on the magnetic properties. We also study the stability of the magnetic coupling over different conditions: variation of U (this mimics different screening conditions), consider a spin spiral order and structural distortions. The theoretical results are used to interpret the experiments. Previous work, Ref.[75], shows that the chain

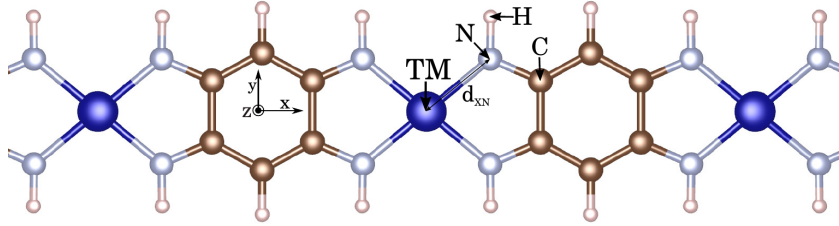


Figure 5.1: Structure of the TMQDI chains where TM=Co, Cr.

could be easily manipulated with the STM, implying a weak substrate-chain interaction. Therefore, our analysis is done considering a planar free-standing chain, i.e., no Au(111) substrate is considered.

The chapter is organized as follows: in Section 5.2, combining DFT+ U and OMC, we calculate the possible spin states and establish the ground state of each system. In Section 5.3, the magnetic properties of the CoQDI and CrQDI chains are analyzed using DFT+ U , with a study of the robustness of the magnetic coupling for the CrQDI chain. We compare our results with the experimental data. Finally, in Section 5.4, we give the main conclusions of the chapter.

5.2 Computational details

The theoretical analysis of the unsupported planar chains is done using DFT+ U calculations with the Vienna Ab Initio Simulation Package (VASP) (see Section 2.2), with the PBE exchange-correlation functional[84]. The Hubbard- U correction scheme is applied via Dudarev's functional[102]. The plane-wave cut-off energy is set at 450 eV with a $10 \times 1 \times 1$ k -grid centered at Γ . The relaxed geometry is calculated imposing a periodic supercell and setting 12 Å of vacuum between the periodic repetitions. The forces minimization threshold is < 0.01 eV/Å and the total energy minimization convergence criterion is set to 10^{-6} eV.

In the geometrical optimization, we modify the lattice parameters of the chain and let the molecule atoms to relax while the TM atom is frozen. The aromatic ring bond lengths are almost unaffected by the geometrical relaxation, the distance between the N and C atoms changes by less than 0.02Å compared to the gas-phase molecule. The main change is at the bond length between the TM atom and N atoms. In Fig. 5.2, we show the resulting total energy curve for $U = 0, 1.5, 4$ and 5 eV. For $U = 0$ and 1.5 eV only one curve is obtained. For high U values (4 and

5 eV), two different curves are obtained showing different minima. At each curve, the Co atom shows a different spin state: a low-spin state (LS) with $S = 1/2$ (blue) and the red curve is a high-spin state (HS) with $S = 3/2$ (red), i.e., there is a spin crossover. Each spin state shows a distinct Co-N bond length as indicated in Fig. 5.2. In Table 5.1, we give the Co-N bond length and the spin magnetic moment of the Co atom for the LS and HS states. The LS state shows a shorter bond length compared to the HS one. The bond lengths do not show a large variation when U increases. For $U = 5$ eV the HS and LS states' energies differ 88 meV, while for $U = 4$ eV, the energy difference is 200 meV.

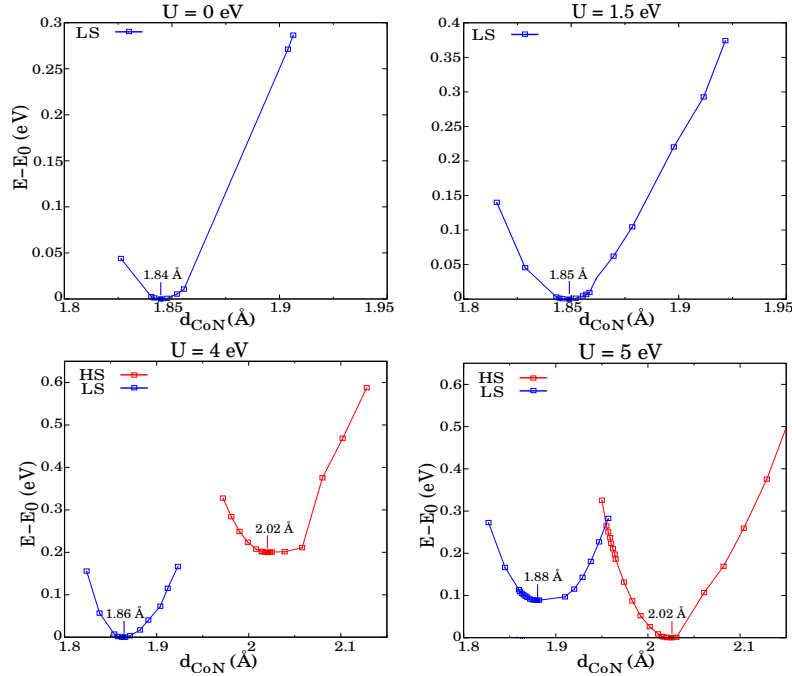


Figure 5.2: Total energy with respect to the Co-N bond length measured from the ground state of each U value. The curve color shows the spin state of the Co atom: blue for $S = 1/2$ (LS) and red for $S = 3/2$ (HS).

In Fig. 5.3, we show the energy at each bond-length for $U = 0, 3, 4$ and 5 eV for the CrQDI chain. As in CoQDI, we have considered different lattice vectors and then let the geometry to relax, maintaining only the TM atom frozen. For all U values, only one spin state is obtained, $S = 2$. The equilibrium bond lengths show a significant change between $U = 0$ and $U = 3$ eV, while there is almost no variation in the Cr-N distance between $U = 3, 4$ and 5 eV. In Table 5.1, we show the bond length between the Cr and O atom and the spin magnetic atom of the

Cr atom for $U = 5$ eV.

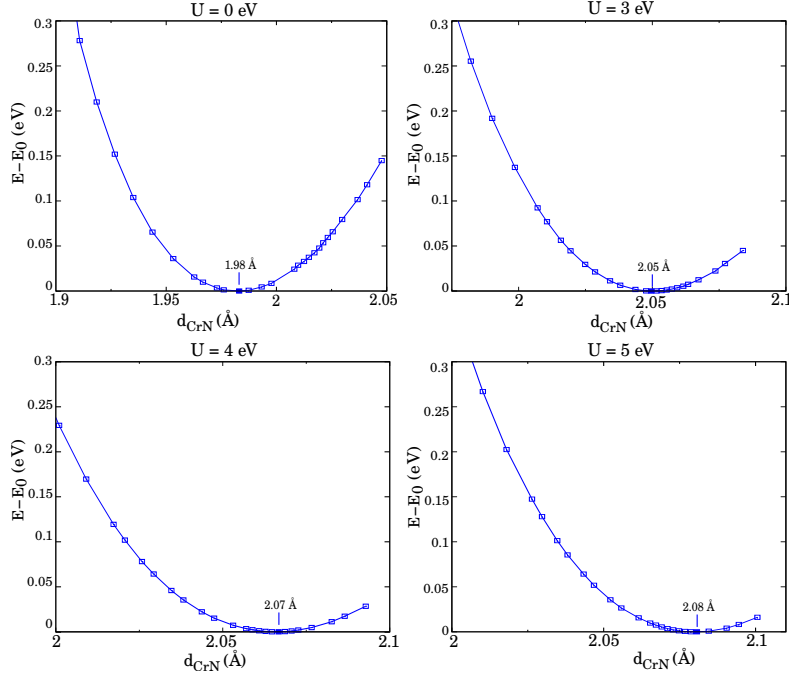


Figure 5.3: Total energy with respect the Cr-N atom bond-length measured from the ground state total.

	$d_{\text{TM-N}}$	μ_{TM}^S (μ_B)
CoQDI (LS) ($U = 4$ eV)	1.86	1.20
CoQDI (HS) ($U = 5$ eV)	2.02	2.73
CrQDI ($U = 5$ eV)	2.08	3.71

Table 5.1: Equilibrium TM-O bond lengths and spin magnetic moment of each TM atom.

In Figs. 5.4 and 5.5, we show the band structure and the projected density of states (PDOS) of both chains. The CoQDI shows a metallic-to-insulator transition when the spin state goes from the LS to the HS state. In the former, the majority d_{xy} band is half-filled, while in the HS state becomes fully occupied. The minority spin bands show the largest change: in the HS state, only the d_{z^2} and $d_{x^2-y^2}$ bands are fully occupied, while in the LS the d_{xy} and d_{xz} bands are partially filled. The change in the orbital occupancy is related to a different hybridization between the Co(d) and O(p) orbitals. The CrQDI chain shows an insulator state with an empty $d_{xy,\uparrow}$ orbital and all minority orbitals unoccupied.

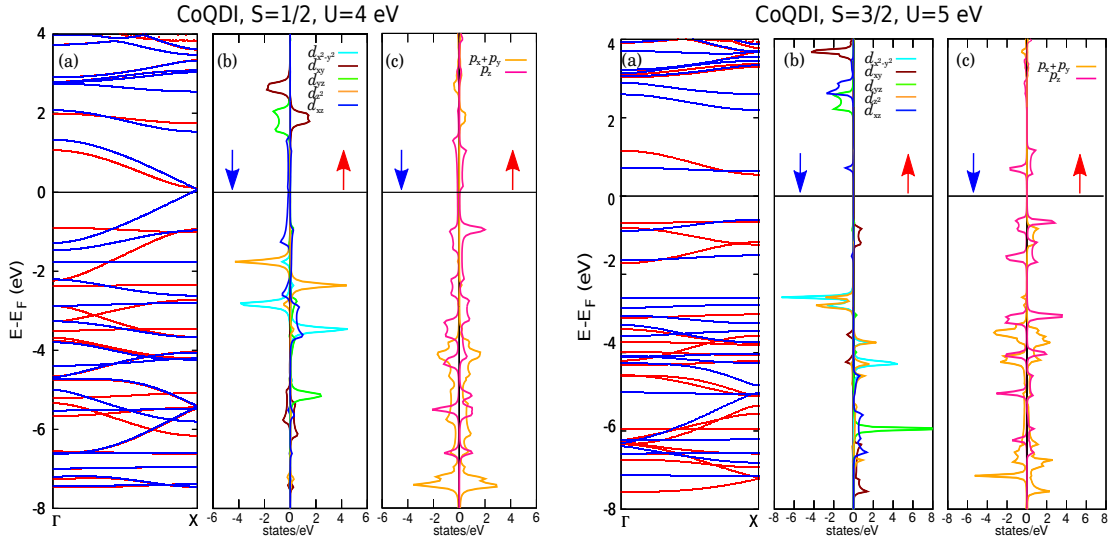


Figure 5.4: Electronic structure of the CoQDI chain in the LS (left) and HS (right) states. (a) Band structure for majority (red) and minority (blue) spins. The PDOS for the Co(d) orbitals is shown in (b) and for the O(p) in (c).

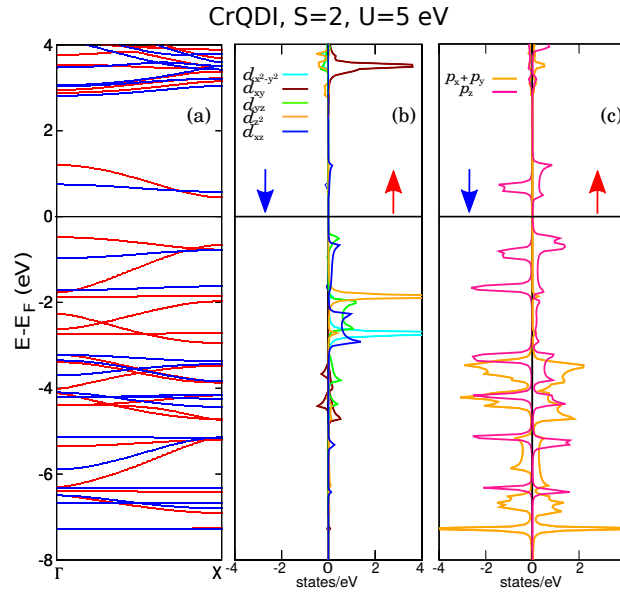


Figure 5.5: Same as in Fig. 5.4 for the CrQDI chain.

Metastable configurations

As previously commented, the U functional introduces a dependence on the initial orbital configuration. A study of the energy minimization for several orbital matrix occupations can confirm if the so-far converged states are the GSs and, in passing, find metastable states of the energy functional. For this analysis, we use

the OMC method.

We consider first the HS state with $U = 5$ eV. The orbitals occupation matrices have to be built keeping a $S = 3/2$ state. The majority spin matrix is fully occupied, while the minority spin one has two occupied orbitals. We have to build combinations with two electrons filling different orbitals. Due to the planar chain symmetry, the out-of-plane d_{xz} and d_{yz} can share an electron, while one of the remaining orbitals can be fully occupied by the remaining electron. We also consider the sp^3d^2 hybrid atomic orbital, where the out-of-plane d_{z^2} and in-plane orbitals $d_{x^2-y^2}$ become hybridized and hence, share an electron. We use the following notation to simplify the matrices:

$$[111111] = \begin{pmatrix} 1 & 0 & 0 & 0 & 0 \\ 0 & 1 & 0 & 0 & 0 \\ 0 & 0 & 1 & 0 & 0 \\ 0 & 0 & 0 & 1 & 0 \\ 0 & 0 & 0 & 0 & 1 \end{pmatrix}, [0h0h1] = \begin{pmatrix} 0 & 0 & 0 & 0 & 0 \\ 0 & 0.5 & 0 & 0.5 & 0 \\ 0 & 0 & 0 & 0 & 0 \\ 0 & 0.5 & 0 & 0.5 & 0 \\ 0 & 0 & 0 & 0 & 1 \end{pmatrix}. \quad (5.1)$$

The last matrix is an example of the d_{xz} and d_{yz} orbitals sharing an electron, indicated with h . The order of the orbitals is $[d_{xy} d_{yz} d_{z^2} d_{xz} d_{x^2-y^2}]$. There are 11 different combinations to be considered. In Table 5.2, we give the initial orbital occupation matrices and the final ones after the OMC is applied and a self-consistent energy minimization procedure (without constraint orbital occupations) has been done. We also give the energy difference with respect to the true ground state. We fix the atomic positions to the relaxed structure obtained in the previous section. From 11 initial matrices, only seven different configurations are converged. The ground state orbital configuration is $[00101]$, the same as obtained without OMC. The $[00h1h]$ orbital occupation configuration shows only 72 meV of difference with respect to the ground state. The interatomic forces in the metastable state are < 0.05 eV/Å, thus, letting the geometry to relax still maintains the HS-2 configurations. Hence, this metastable state may become relevant in the calculations, if any distortion is applied to the chain, the energy minimization can go to the excited state instead of the GS.

To differentiate the GS and this metastable state, in the following we label them as HS-1 and HS-2, respectively. All the other excited states show differences larger than 300 meV with respect to the ground state. Therefore, in principle, these states can be disregarded as the energy difference is too large. The PDOS of the HS-1 and HS-2 configurations is shown in Fig. 5.6. HS-1 and HS-2 differ in the

Initial conf.	Final conf.	μ_{Co}^S (μ_B)	$\Delta E = E - E_0$ (eV)
[1 0 1 0 0]	[1 0 1 0 0]	2.88	1.682
[1 0 0 0 1]	[0 0 1 0 1]	2.73	0.000
[0 0 1 0 1]	[0 0 1 0 1]	2.73	0.000
[0 1 0 1 0]	[0 1 0 1 0]	2.75	0.333
[1 h 0 h 0]	[0 h 1 h 0]	2.75	0.563
[0 h 1 h 0]	[0 h 1 h 0]	2.75	0.563
[0 h 0 h 1]	[0 h 0 h 1]	2.73	0.471
[1 0 h 0 h]	[1 0 h 1 h]	1.06	0.385
[h h h h 0]	[0 0 h 1 h]	2.74	0.072
[0 h h h h]	[0 0 h 1 h]	2.74	0.072
[h 0 h 0 1]	[0 0 1 0 1]	2.73	0.000

Table 5.2: Initial and converged minority spin orbital occupation matrices at the HS state. The energy with respect to the ground state is given for each calculation. We also give the spin magnetic moment of the Co atom of each converged state. The calculations were done at $U = 5$ eV.

minority occupation. In HS-1, the $d_{z^2,\downarrow}$ and $d_{x^2-y^2,\downarrow}$ bands are filled and $d_{xz,\downarrow}$ is empty, while in the HS-2, $d_{z^2,\downarrow}$ and $d_{x^2-y^2,\downarrow}$ are half-filled and d_{xz} is fully occupied. In HS-1 the $d_{xz,\uparrow}$ orbital is localized in energy between $E_F - 7$ and $E_F - 5$ eV, while in the HS-2 it is set between $E_F - 6$ and $E_F - 4$ eV. The $d_{z^2,\uparrow}$ and $d_{x^2-y^2,\uparrow}$ show sharper peaks at $E_F - 4$ eV in the HS-1 state than in the HS-2. Nevertheless, the different occupation does not affect the Co(d)-N(p) bond. As shown in Fig. 5.6, the N(p) PDOS is only slightly affected. We compare both states with a calculation done using the hybrid HSE06 functional. The hybrid calculation shows a similar configuration as the HS-1 state as ground state, albeit with sharper peaks and a larger gap than the GGA calculations. This is due to the Hartree-Fock approximation employed in the hybrid functional, which uses the bare electron interaction, overriding the screened value of the GGA, resulting in a stronger localization and a larger gap.

We make the same study for the LS state. In this case, the occupation matrices are built considering the $S = 1/2$ state. In the converged LS state, the majority orbital is occupied by four electrons and the minority part with three electrons. We also take into account the hybridization, e.g., d_{xz} and d_{yz} symmetry and the sp^3d^2 hybrid orbital. This results in six different orbital occupations for the majority channel and eleven for the minority one, 66 combinations in total. To reduce the total number of combinations to be studied, we make use of an estimation of the correlation energy:

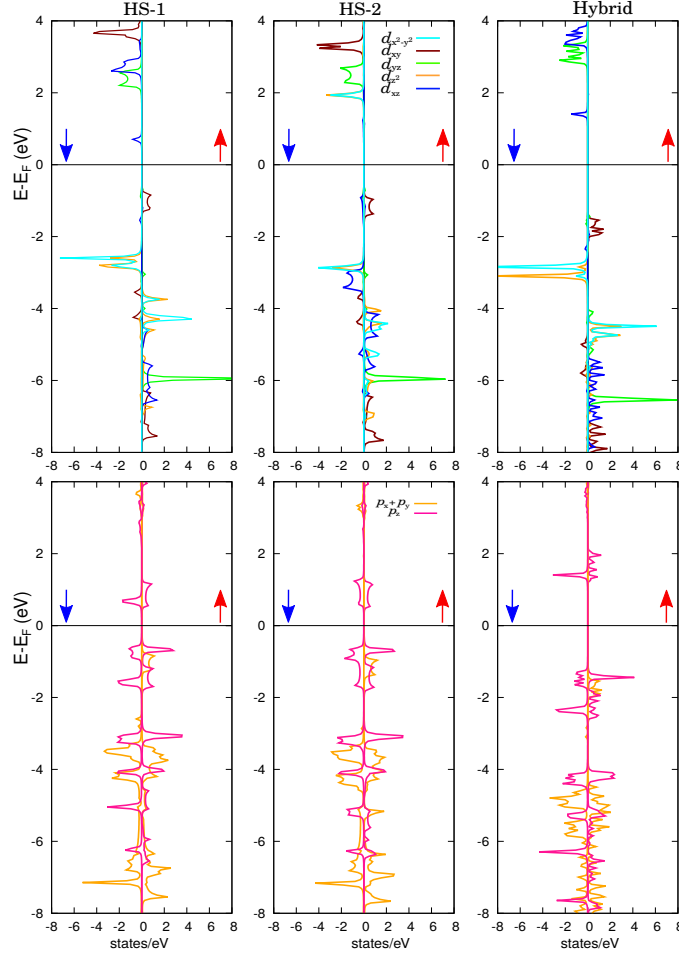


Figure 5.6: PDOS for Co(d) at the HS-1 ground state, HS-2 metastable states with DFT+ U and the hybrid functional result. Calculations for the HS-1 and HS-2 were done with $U = 5$ eV

$$E_U = U \sum_m N_m(N_m - 1) \quad (5.2)$$

where $N_m = \sum_{\sigma} n_{m\sigma}$, being $n_{m\sigma}$ the individual occupation at each m orbital and spin $\sigma = \uparrow, \downarrow$. In the HS state, all the different combinations have $E_U^{\text{HS}} = 6U$ and in the case of the already converged LS is $E_U^{\text{LS}} \sim 4.5U^1$. For a given U , the only possibility to reduce E_U is modifying the orbital occupancy. In a simple approximation, the LS GS should have a lower or equal E_U^{LS} value as the converged LS state. In the end, we consider only those orbital occupations that satisfy $E_U \leq 3.5U$ eV. This reduces the total number of orbital matrices to be tried out to 23 (see Table 5.3).

¹We consider empty, full or half-filled orbitals for this value, i.e., without partial fillings.

After the OMC procedure, only five different states remain. From these states, only one configuration shows a small energy difference (92 meV) with respect to the ground state. However, in this low-energy metastable state, values of the interatomic forces are of the order of ~ 0.3 eV/Å. After geometry relaxation, the orbital occupation converges to the ground state. Therefore, we can disregard this metastable state. Other metastable states show a difference in energy larger than 800 meV. Thus, we consider that only the orbital occupation with $[0.5\ 1\ 1\ 1\ 1]$, $[0.5\ 0\ 1\ 0.75\ 1]$ on-site values will be achieved in DFT calculations. Calculations with occupation matrices that are between $4U < E_U^{LS} < 5U$ show also that the latter state is maintained as GS.

Initial conf. \uparrow, \downarrow	Final conf. \uparrow, \downarrow	μ_{Co}^S (μ_B)	$\Delta E = E - E_0$ (eV)
$[1\ 1\ 1\ 1\ 0]$, $[0\ h\ 1\ h\ 1]$	$[0.5\ 1\ 1\ 1\ 1]$, $[0.5\ 0\ 1\ 0.75\ 1]$	1.14	0.000
$[1\ 1\ 1\ 1\ 0]$, $[1\ h\ 0\ h\ 1]$	$[0.5\ 1\ 1\ 1\ 1]$, $[0.5\ 1\ 0\ 1\ 1]$	1.05	0.092
$[1\ 1\ 1\ 1\ 0]$, $[h\ h\ h\ h\ 1]$	$[0.5\ 1\ 1\ 1\ 1]$, $[0.5\ 0\ 1\ 0.75\ 1]$	1.14	0.000
$[1\ h\ 1\ h\ 1]$, $[1\ 1\ 0\ 1\ 0]$	$[1\ 1\ 1\ 1\ 1]$, $[0, 1, 0, 1, 0]$	2.61	1.23
$[1\ h\ 1\ h\ 1]$, $[0\ 1\ 1\ 1\ 0]$	$[0.5\ 1\ 1\ 1\ 1]$, $[0.5\ 0\ 1\ 0.75\ 1]$	1.14	0.000
$[1\ h\ 1\ h\ 1]$, $[0\ 1\ 0\ 1\ 1]$	$[0.5\ 1\ 1\ 1\ 1]$, $[0.5\ 1\ 0\ 1\ 1]$	1.05	0.092
$[1\ h\ 1\ h\ 1]$, $[0\ h\ 1\ h\ 1]$	$[0.5\ 0\ 1\ 0.75\ 1]$, $[0.5\ 1\ 1\ 1\ 1]$	-1.14	0.000
$[1\ h\ 1\ h\ 1]$, $[h\ 1\ h\ 1\ 0]$	$[0.4\ 1\ 1\ 1\ 1]$, $[0.5\ 1\ 0\ 1\ 1]$	1.05	0.092
$[1\ h\ 1\ h\ 1]$, $[h\ h\ h\ h\ 1]$	$[0.5\ 1\ 1\ 1\ 1]$, $[0.5\ 0\ 1\ 0.75\ 1]$	1.14	0.000
$[1\ h\ 1\ h\ 1]$, $[0\ 1\ h\ 1\ h]$	$[0.4\ 1\ 1\ 1\ 1]$, $[0.5\ 1\ 0\ 1\ 1]$	1.05	0.092
$[1\ h\ 1\ h\ 1]$, $[1\ h\ h\ h\ h]$	$[0.4\ 1\ 1\ 1\ 1]$, $[0.5\ 1\ 0\ 1\ 1]$	1.05	0.092
$[1\ 1\ 0\ 1\ 1]$, $[1\ h\ 1\ h\ 0]$	$[0.5\ 1\ 0\ 1\ 1]$, $[0.4\ 1\ 1\ 1\ 1]$	-1.05	0.092
$[1\ 1\ 0\ 1\ 1]$, $[0\ h\ 1\ h\ 1]$	$[0.4\ 1\ 1\ 1\ 1]$, $[0.5\ 1\ 0\ 1\ 1]$	1.05	0.092
$[0\ 1\ 1\ 1\ 1]$, $[1\ h\ 1\ h\ 0]$	$[0.4\ 1\ 1\ 1\ 1]$, $[0.5\ 1\ 0\ 1\ 1]$	1.05	0.092
$[0\ 1\ 1\ 1\ 1]$, $[1\ h\ 0\ h\ 1]$	$[0.4\ 1\ 1\ 1\ 1]$, $[0.5\ 1\ 0\ 1\ 1]$	1.05	0.092
$[0\ 1\ 1\ 1\ 1]$, $[1\ h\ h\ h\ h]$	$[0.5\ 1\ 1\ 1\ 1]$, $[0.5\ 0\ 1\ 0.75\ 1]$	1.14	0.000
$[1\ 1\ h\ 1\ h]$, $[0\ h\ 1\ h\ 1]$	$[0.5\ 1\ 1\ 1\ 1]$, $[0.5\ 0\ 1\ 0.75\ 1]$	1.14	0.000
$[1\ 1\ h\ 1\ h]$, $[h\ h\ h\ h\ 1]$	$[0.5\ 1\ 1\ 1\ 1]$, $[0.5\ 0\ 1\ 0.75\ 1]$	1.14	0.000
$[1\ 1\ h\ 1\ h]$, $[1\ h\ h\ h\ h]$	$[1\ 1\ 1\ 1\ 1]$, $[0\ 0\ h\ 1\ h]$	2.47	0.811
$[h\ 1\ h\ 1\ 1]$, $[1\ 0\ 1\ 0\ 1]$	$[0.5\ 1\ 1\ 1\ 1]$, $[0.5\ 0\ 1\ 0.75\ 1]$	1.14	0.000
$[h\ 1\ h\ 1\ 1]$, $[1\ h\ 1\ h\ 0]$	$[0.5\ 1\ 1\ 1\ 1]$, $[0.5\ 1\ 1\ 1\ 0]$	1.17	1.323
$[h\ 1\ h\ 1\ 1]$, $[h\ h\ h\ h\ 1]$	$[0.5\ 1\ 1\ 1\ 1]$, $[0.5\ 0\ 1\ 0.75\ 1]$	1.14	0.000
$[h\ 1\ h\ 1\ 1]$, $[1\ h\ h\ h\ h]$	$[0.5\ 1\ 1\ 1\ 1]$, $[0.5\ 0\ 1\ 0.75\ 1]$	1.14	0.000

Table 5.3: Same information as in Table 5.2 for the LS state. We show the majority and minority matrices of each calculation. The calculations were done at $U = 4$ eV.

To obtain a complete analysis of all the chains, we also use the OMC method in the CrQDI chain. In the converged ground state the majority spin orbital matrix has four electrons while the minority one is completely empty. From seven different initial matrices, only two different states are kept after the energy minimization procedure (see Table 5.4). One is the ground state given by [0 1 1 1 1], and the other one is a metastable state, [1 1 1 1 0], with a large energy difference of 2.15 eV.

Initial configuration	Final conf.	μ_{Cr}^S (μ_B)	$\Delta E = E - E_0$ (eV)
[0 1 1 1 1]	[0 1 1 1 1]	3.71	0.000
[1 0 1 1 1]	[0 1 1 1 1]	3.71	0.000
[1 1 0 1 1]	[0 1 1 1 1]	3.71	0.000
[1 1 1 0 1]	[0 1 1 1 1]	3.71	0.000
[1 1 1 1 0]	[1 1 1 1 0]	3.54	2.151
[1 1 <i>h</i> 1 <i>h</i>]	[0 1 1 1 1]	3.71	0.000
[1 <i>h</i> 1 <i>h</i> 1]	[0 1 1 1 1]	3.71	0.000

Table 5.4: Same information as in Table 5.2 for the CrQDI chain. The calculations were done at $U = 5$ eV.

5.3 Magnetic anisotropy and exchange coupling

Knowledge of the true ground state is mandatory to obtain the actual magnetic properties of the chains. In this section, we + calculate the magnetic anisotropic energy (MAE) and the magnetic exchange coupling constant of the CoQDI and CrQDI chains.

XAS, XMCD and XML experiments

In this section, we present the experimental data of the CoQDI and CrQDI obtained by XAS/XMCD and XAS/XLD experiments provided by C. Wackerlin *et al.*. The XAS experiment is based on electrons getting excited by the absorption of an X-ray photon. In the XAS/XMCD and XAS/XLD experiments, the photons are polarized circularly (σ^L and σ^R) or linearly (σ^h or σ^v) while an external magnetic field is applied to the sample. Combining the XAS/XMCD and XAS/XLD data with atomic multiplet calculations the spin state, magnetic coupling and the MAE of each chain can be determined. The obtained results are given in Table 5.5.

The CoQDI is determined to be in the $S = 3/2$ ground state, which agrees with our calculations for the HS state, which points to a high electron correlation with $U \geq 5$ eV. The CrQDI is in a $3d^4$ state, i.e., $S = 2$, also in agreement with the DFT+ U calculations. By fitting the XLD data, the CoQDI chain is shown to have the easy-axis aligned along the y -axis, while in the CrQDI the easy-axis is along the z -axis. The fitted data of the XLD experiment is used to obtain the crystal field parameters of the systems. The latter parameters are used in the multiplet calculations to simulate the XMCD spectra. Because atomic multiplet calculations consider the metal atoms individually (as if they were paramagnetic), the simulated XMCD spectra (b-f) show a large magnetic dichroism in the absence of magnetic interactions. However, the experimental XMCD of Co is quenched (b,c) and the one of Cr is very weak (e,f), thus, suggesting an antiferromagnetic interaction in both cases.

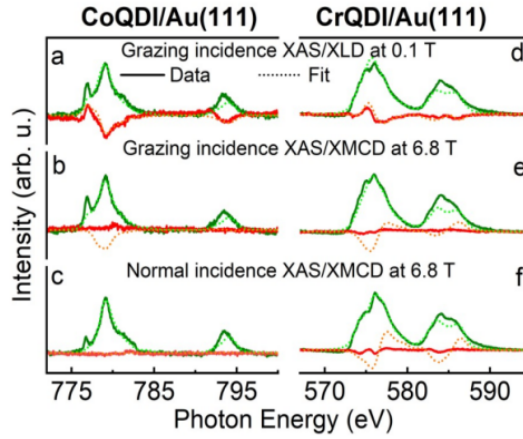


Figure 5.7: XAS/XMLD and XAS/XMCD experimental and simulated data. The XAS/XMLD fitted data results are used to simulate the XAS/XMCD spectra. The solid line indicates the experimental data (green: XAS and red: XLD and XMCD). The simulations are indicated by the dotted lines (light green: XAS and orange: XLD and XMCD). The figure has been obtained from [191]

TM atom	Spin state	μ_{TM}^S (μ_B)	μ_{TM}^L (μ_B)	Easy-axis	ZFS (meV)
Co	$1.47 \cong 3/2$ (HS)	2.94	1.79	y	37
Cr	$4/2$	4	0.05	z	0.7

Table 5.5: Resulting magnetic properties from the XAS/XMCD and XAS/XMLD data for the CoQDI and CrQDI chains. The MAE is given by the zero-field splitting (ZFS)[149, 150] value.

DFT calculations

The DFT calculations are used to interpret the obtained experimental results in terms of the electronic structure of the systems. In addition, we analyze the consequences on the MAE and exchange coupling of the previously found low-energy states in the CoQDI chain. First, we calculate the MAE for each metal-organic chain. The spin-orbit coupling (SOC) is evaluated self-consistently, and the MAE is calculated as the difference in the total energy between the different magnetization alignments (see Section 2.3). The total energy convergence threshold is set at 10^{-8} eV.

Magnetic anisotropic energy

For the CoQDI, we have calculated the MAE for the LS, HS-1 and HS-2 states. The results are given in Table 5.6. For the LS state, the easy axis is along the chain axis. In both cases, HS-1 and HS-2 states have an in-plane easy axis across the chain, with the HS-2 MAE value being twice that of the HS-1 one. In the PDOS (Fig. 5.6) of the HS-1 state, we see that the $d_{xz,\downarrow}$ is the empty state closest to the Fermi level. According to Ke *et al.* [113], transitions between the d_{z^2} and $d_{x^2-y^2}$ orbitals to the d_{xz} ($m' = m + 1$ and $\sigma = \sigma'$ type) favor the in-plane easy-axis. In the HS-2 state, the $d_{xz,\downarrow}$ is filled, therefore a hopping electron in this orbital can contribute to set the orbital moment along the y -axis, which is missing in the HS-1 state [55] (see Fig. 3.6). The obtained result for the HS states agrees with the experimentally observed easy-axis, but the values differ by one order of magnitude from the experimental ones. The magnitude order difference appears also between the theoretical and measured orbital moments (see Table 5.7). Note that DFT+ U calculations tend to underestimate the orbital moment (\mathbf{L}) [95, 192]. Bruno's relation states that MAE is proportional to the orbital moment [114, 54]. In all the cases, the orbital anisotropy shows the largest projection of \mathbf{L} along the easy-axis directions. The change of the MAE between the HS-1 and HS-2 states is not reflected in the orbital moment anisotropy, as it is almost unaffected. The easy-axis change between the HS and LS states results from the orbital occupancy matrix variation.

In the CrQDI chain, the easy-axis is out-of-plane of the chain, i.e., it is the z -axis. The DFT calculation agrees with the XAS/XMLD results in the sign and order of magnitude. In Table 5.6, the orbital moment also shows a similar value in both experimental and DFT results. The calculated orbital anisotropy also follows Bruno's relation. The antiparallel alignment between the orbital moment (\mathbf{L}) and

spin (\mathbf{S}) is due to Hund's third rule.

TM atom	μ_{TM}^L (μ_B)	MAE (meV)	Easy-axis
Co	0.200	-0.76 ($x - z$)	x
Co (HS-1)	0.207	-1.22 ($y - z$)	y
Co (HS-2)	0.236	-2.76 ($y - z$)	y
Cr	-0.039	0.54 ($x - z$)	z

Table 5.6: MAE results for the CoQDI and CrQDI chains. The total energy difference is calculated between the easy and hardest axis of each chain. The calculation for the LS state is done with $U = 4$ eV and the rest with $U = 5$ eV. We indicate the easy-axis of each chain and give the orbital moment (μ_{TM}^L) projection along the easy axis of each TM atom.

TM atom	$\mu_{\text{TM},x}^L$ (μ_B)	$\mu_{\text{TM},y}^L$ (μ_B)	$\mu_{\text{TM},z}^L$ (μ_B)
Co (LS)	0.200	0.039	0.066
Co (HS-1)	0.200	0.207	0.086
Co (HS-2)	0.191	0.236	0.100
Cr	-0.013	-0.017	-0.039

Table 5.7: Orbital moment anisotropy of the TM atoms. The projection is calculated by setting \mathbf{L} along the direction of \mathbf{S} at the beginning of each calculation (throughout the self-consistent calculations the collinearity is maintained, i.e., transverse directions values are negligible).

Magnetic coupling

To obtain the magnetic coupling constant we double the periodic cell and calculate the total energy for ferromagnetic (FM) and antiferromagnetic (AFM) spin alignments. We let the doubled cell geometry to relax. OMC method is applied to the HS-CoQDI to ensure convergence to the HS-1 configuration. From these calculations, the magnetic exchange coupling constant (\mathcal{J}) can be obtained (see Eq. (3.2)). In Table 5.8, we give the resulting total energy differences between the AFM and FM states, the coupling constant \mathcal{J} and the TM atoms spin magnetic moment.

In the CoQDI, the LS spin state favors a weak FM coupling, being the total energy difference less than 1.50 meV. In both HS states, the TM atoms spins prefer the antiparallel alignment. The obtained result in the HS-1 state agrees with the absence of signal in the XMCD experiments. The Cr spins show an AFM coupling.

Remarkably, the band structure of each chain (see Figs. 5.4 and 5.5), shows that the LS state which prefers a FM coupling is the only metallic one, while the HS states and CrQDI are both insulators with an AFM coupling. The metallicity and magnetic coupling follow the same trend observed in the TMO chains.

TM atom	$\Delta E(\text{meV})$	\mathcal{J} (meV)	$\mu_{\text{TM}}^S (\mu_B)$
Co (LS)	1.48	2.05 (FM)	1.20
Co (HS-1)	-11.07	-2.97 (AFM)	2.73
Co (HS-2)	-7.60	-2.02 (AFM)	2.74
Cr	-30.43	-4.42 (AFM)	3.71

Table 5.8: Total energy difference calculated as $\Delta E = E^{\text{AFM}} - E^{\text{FM}}$, coupling constant and spin magnetic moment. The electron interaction is set to $U = 5$ eV, except for the LS state where $U = 4$ eV.

We will address the AFM coupling of the CrQDI. Considering that the magnetic interactions between the distant TM atoms occur via the organic molecule, and the magnetic moment is largely localized in the TM atom. Therefore, one could expect that the interaction between the TM atoms is small, hence, a low value of the magnetic coupling constant could be expected. Indeed, the XMCD data shows an almost negligible signal. The obtained total energy difference and \mathcal{J} value for the CrQDI does not agree with that interpretation. The disagreement can be a result of different assumptions made in the theoretical calculations, such as the U value, the planar geometry, or even a consequence of effects not considered previously, for instance, the presence of a different spin ordering or an anisotropic exchange coupling due to SOC. Therefore, we have performed an analysis of the change of the CrQDI chain exchange coupling constant when the previous situations are considered.

We start by varying the value of U . Experimental control of the chains with STM showed a weak interaction with the Au(111) substrate. This effect is also confirmed by the good agreement between the experimental and DFT calculations in the unsupported chain. The value of U can be quite large in one-dimensional systems in the absence of interaction with the substrate, for instance, cRPA calculations have shown that free-standing oxide chains could reach up to $U \approx 8$ eV (see Chapter 4). Therefore, we analyze the change of \mathcal{J} in the range of U between 0 and 8 eV. The results are given in Table 5.9. As expected, the trend of \mathcal{J} is to decrease its value upon the increase of U , because the coupling constant is known to behave as $\propto U^{-n}$, e.g., direct exchange, superexchange interaction, etc. [10].

The coupling for a value of U as large as 8 eV is halved compared to the $U = 5$ eV, as the energy difference, in this case, is ~ 15 meV. The energy difference is reduced, but the system is weakly AFM.

U	\mathcal{J} (meV)
0	-19.03
3	-14.56
4	-6.45
5	-4.42
8	-2.09

Table 5.9: Exchange coupling constant variation with respect to the value of U for the CrQDI chain.

Next, we investigate the possibility that \mathcal{J} has an anisotropic behavior, i.e., its value depends on the magnetization orientation. We have performed DFT+SOC calculations at different magnetization alignments in the doubled cell. The variation of the resulting magnetic coupling constants, shown in Table 5.10, is weak.

We have also examined the possibility of a non-collinear spin ordering, originated

Axis	\mathcal{J} (meV)
x	-4.336
y	-4.339
z	-4.335

Table 5.10: Exchange coupling constant at each crystallographic axis when SOC is considered for the CrQDI chain.

from the non-negligible interaction between neighbors further than the nearest ones. The exchange coupling constant between a spin and its n -th neighbors can be obtained by Fourier transforming the coupling constant for different values of the spin spiral wave q , \mathcal{J}_q :

$$\mathcal{J}_n = \frac{1}{N_q} \sum_{-q}^q \mathcal{J}_q e^{iqna}, \quad \text{where} \quad \mathcal{J}_q = \frac{E_q - E_0}{S^2}, \quad (5.3)$$

where n is the atom number, a the lattice parameter and N_q the total number of used q values. In Fig. 5.8(a), we show the obtained total energies for the CrQDI referred to the energy of $q = 0$, E_0 . $q = 0$ corresponds to the FM alignment and $q = \frac{2\pi}{a}\frac{1}{2}$ to AFM. Since the latter q value shows the lowest energy, the AFM alignment is favored against the formation of spin spirals. Fig. 5.8(b) shows that the

next-nearest exchange constant $|\mathcal{J}_2|$ is half the $|\mathcal{J}_1|$ value. The exchange constant \mathcal{J} for $n > 2$ is drastically reduced by one order of magnitude. Thus, the AFM coupling is preferred over a non-collinear order.

We continue to investigate other possible effects that may change the nearest-neighbor interaction. We have said earlier that the Au substrate is inert, i.e., negligible charge transfer, but the substrate can affect the geometry of the chains. Therefore, we have investigated the stability of the exchange coupling under vibrational distortions of the CrQDI chain that modify the Cr-N bond. We have done these studies at the Γ point in the doubled cells. Neglecting distortions that do not affect the Cr-N bonds and the three translational modes, only three possible low-energy ($E \lesssim 6$ meV) and low-frequency ($\nu \lesssim |1.5|$ THz) distortions are possible candidates. These three modes appear in the AFM and FM states. These modes are a soft mode that bends the TM-N bond and two real modes that twist the molecule: one out-of-plane and the other in-plane. These three distortions are shown in Fig. 5.9. Neither of these low-energy distortions can change the preferred coupling. Remarkably, both magnetic orders show the same trend, showing that \mathcal{J} remains constant when low amplitude distortions are applied.

The analysis shows that the exchange coupling is robust under different modifications of the CrQDI chain. The mismatch can be due to other effects, such as, neglecting the effect of the substrate through weak van der Waals interactions or screenings effects, recall that the Ir substrate showed a non-negligible screening even if there was no charge transfer to the TMO chains. In addition, as we are in the low-dimensional case, the description of the enhanced exchange-correlation interactions is within the limit of DFT theory [193].

5.4 Conclusions

We have studied two metal-organic chains, CoQDI and CrQDI, where organic ligands connect the transition metal atoms. Our DFT+ U calculations show that the CoQDI has a spin-crossover from a low-spin state ($S = 1/2$) to a high-spin state ($S = 3/2$), triggered by a U value change from 4 to 5 eV. Occupancy matrix control calculations show that the CoQDI chain has a metastable state with $S = 3/2$ at 72 meV from the HS ground state. The $S = 1/2$ state does not show any metastable state. The CrQDI chain shows only the $S = 2$ state without metastable states.

In the LS, the exchange coupling between Co atoms is predicted to be FM and

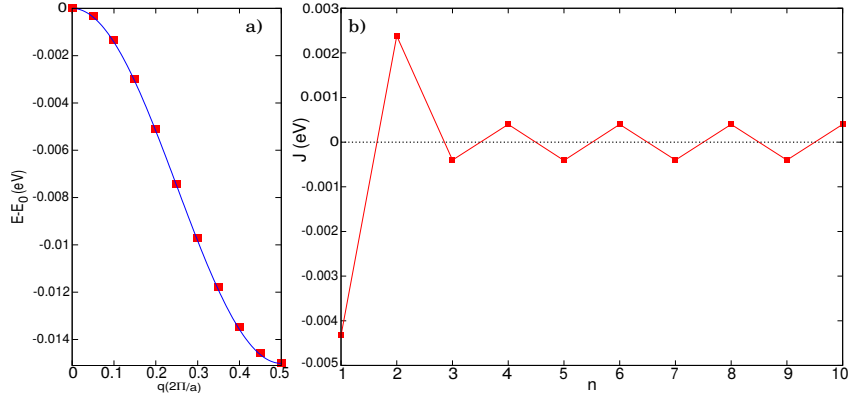


Figure 5.8: Total energies and coupling constant resulting from a spin spiral calculation for the CrQDI chain. (a) The red points are the total energy for each q vector with respect to the total energy of $q = 0$, E_0 . The blue curve shows a fitting to $A\cos(q)$, where A is constant. (b) Resulting J_n for n -th neighbors.

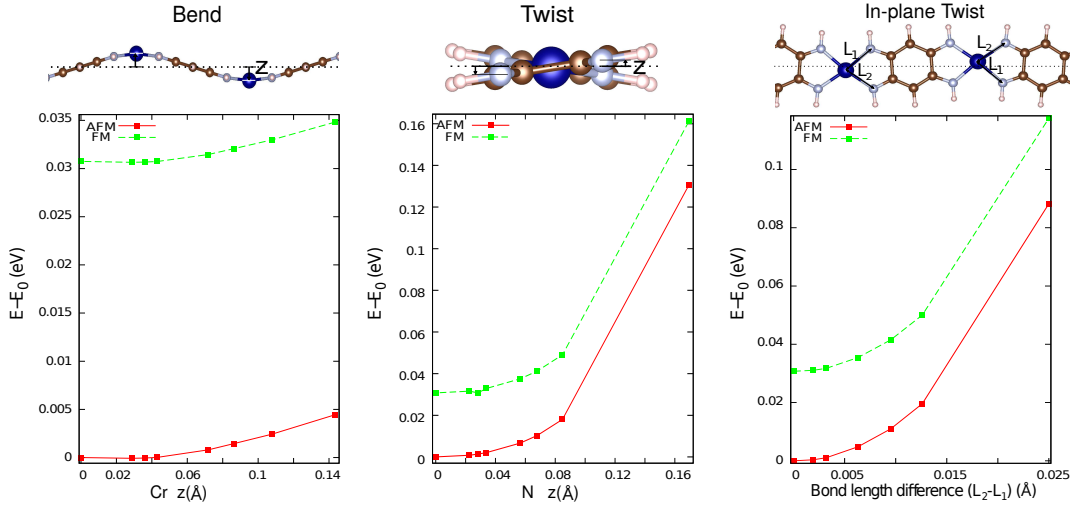


Figure 5.9: Total energy with respect to the lowest energy (AFM without distortion) for the AFM and FM orderings in the distorted CrQDI chain.

the easy axis is orientated along the chain axis, while in both (ground state and metastable) HS states an AFM coupling is preferred and the easy axis is across the chain axis. The HS state is the one that agrees with the XAS/XMCD and XAS/XMLD spin and MAE.

In the CrQDI chain, the easy axis is aligned out-of-plane of the chain in agreement with the experiments. The XAS/XMCD suggests the presence of a significant AFM coupling. However, our theoretical calculations show an evident AFM coupling. To sort out these differences, we have analyzed the coupling constant, \mathcal{J} ,

under several variations, such as, for U values between 0 and 8 eV, including SOC if there is an anisotropic exchange effect, a non-collinear spin ordering and lastly, distortions that modify the Cr-N bond. Except for high values of U , none of these changes significantly modify the magnetic coupling.

Conclusions

It'll pass.

The Priest, *Fleabag*

The main goal of this Thesis is to provide a theoretical description, at the Density Functional Theory (DFT) level, of the magnetic properties and electronic correlation of one-dimensional systems. In particular, we have focused on two types of magnetic chains: oxide chains XO_2 , where $X=Ni, Co, Fe$ and Mn on an $Ir(100)$ substrate, and $XQDI$ chains, where the $X=Co$ and Cr atoms are connected with the organic molecule QDI, grown in an $Au(111)$ substrate.

In the first part of the Thesis, we have analyzed the XO_2 chains using the DFT+ U method. By varying the distance between the atoms for different values of U , we show that the X atoms can have different spin states. The bond-length variations allows to achieve different magnetic states, while the larger U values the larger the S value that can be obtained. For large U values all equilibrium geometries are in a magnetic state. Considering that the $Ir(100)$ substrate screens the value of U , we first set $U = 1.5$ eV to start the calculations for the free-standing chain. The NiO_2, CoO_2, FeO_2 chains prefer the antiferromagnetic (AFM) coupling, while the MnO_2 favors a ferromagnetic (FM) coupling. The metallicity of each chain seems to be related to the preferred magnetic coupling, as the MnO_2 is half-metallic while the other chains are insulators. We have also studied the magnetic anisotropy energy (MAE) using two different methods: the self-consistent, where the spin-orbit coupling (SOC) is evaluated self-consistently, and by force theorem (FT), where SOC is added to a converged scalar-relativistic electron density without self-consistent iterations. In the latter method, the MAE is obtained by the difference over the band energies of the system for two different magnetization directions and in the former by the difference of the total energies. The calculations show that NiO_2 and CoO_2 have the easy-axis of magnetization across

the chain direction, while in FeO_2 and MnO_2 the easy-axis is out-of-plane of the chain. In the NiO_2 , the FT and the self-consistent MAE agree in the predicted easy-axis, but the values differ largely. An analysis of the bands when SOC is included shows that the FT methods fails to accurately describe SOC splittings in bands near Fermi level. Because of the low-dimensionality of the system, the wave functions are not as constrained with symmetries as in bulk, hence, allowing a larger change when SOC is included in the DFT calculation, which the FT is not able to describe. We have calculated the contribution of each eigenstate the MAE and find that the main difference between the preference of in-plane or out-of-plane is in the occupation of the d_{z^2} orbital. When this latter orbital is empty (FeO_2 and MnO_2 chains) the easy axis is out-of-plane.

We have seen that the Hubbard- U parameter is a key component to obtain different magnetic states. In the previous calculations the value of U has been estimated considering screenings effects due to the Ir(100) substrate. By combining DFT and constrained random phase approximation (cRPA) calculations, we have obtained the value of U and J for each chain. The cRPA calculations based on the projection method allow to separate the correlated space and from the rest of the Hilbert space, while transitions between these two spaces are not neglected. cRPA calculation have been done for the unsupported and supported chains. In the planar unsupported case, the insulator FeO_2 reaches the largest value of $U \sim 7.67$ eV, while CoO_2 and MnO_2 are of the order of $U \sim 6$ eV. NiO_2 shows a different behavior, having two different orbital occupation configurations depending on the value of the U while maintaining the same spin state, labeled as C1 and C2. Each configuration converges to a different U value: $U^{\text{C1}} = 6.6$ eV and $U^{\text{C2}} = 2.41$ eV. To account for the p ligand effects, we use the shell folding method: the $\text{O}(p)$ orbitals are included in the correlated space and the resulting $d - p$ interaction is used to renormalize the value of U . These calculations confirm that the ligand-field effect on the correlation varies for each configuration. Non-planar unsupported chain calculations do not show any significant variation of U with respect to the planar case.

In the supported case, the value of U is reduced in comparison with the unsupported case. The largest difference is for $\text{FeO}_2/\text{Ir}(100)$, whereupon deposition, the chain goes from an insulating to a metallic state. Because of the charge transfer from the Ir(100) substrate to the chain, the orbital configuration can be modified. For example, the NiO_2/Ir shows a similar configuration to the C2, and the Fe atom's spin state changes from a $S = 2$ to a $S = 3/2$ state. This, in turn, modifies the ligand-field contribution to the screening. The shell folding method

confirms that the substrate changes the ligand field between the $X(d)$ - $O(p)$ atoms. Inclusion of the $O(sp)$ states into the correlated space shows that in this case the Ir substrate screens both X and O atoms. So, there are two contributions to the screening hybridization with the Ir substrate and the ligand-field modification due to charge transfer. These two contributions can not be decoupled from each other.

In the last part of the Thesis, we have studied the CoQDI and CrQDI polymeric chains. Previous experiments showed that the chains could be easily manipulated with the STM, suggesting a weak coupling with the Au(111) substrate. Therefore, the calculations have been done considering free-standing chains. For values of $4 \leq U \leq 5$ eV the CoQDI chain shows a spin crossover, i.e., a spin transition from a low spin (LS) state $S = 1/2$ to a high spin (HS) state ($S = 3/2$). In CrQDI, only the $S = 2$ state is found for the studied range of U values. We have analyzed the different possible orbital occupations with the same spin using the occupancy matrix control (OMC) method. OMC calculations show that there is an excited state for the CoQDI with $S = 3/2$ at 72 meV with respect to the ground state for $U = 5$ eV. The converged metastable states of LS-CoQDI and CrQDI show a large difference in the energy with respect to the ground state energy. Thus, these states can be disregarded. We have calculated the MAE for the CrQDI, and GS and metastable states of the CoQDI chain. In the CoQDI, the HS ground and metastable states prefer an AFM coupling and an in-plane easy axis across the chain axis. In the LS state, the preferred coupling is FM, and the easy axis is aligned to the chain axis. In the case of the CrQDI, the preferred magnetic coupling is AFM and the easy-axis is the out-of-plane of the chain. These theoretical results are used to interpret the experimental data obtained by XMCD and XLD experiments performed by C. Wackerlin *et al.* [191]. In the CoQDI chain, the data agree with the predicted magnetic properties of the HS state. For the CrQDI, the experimental data agree with the MAE and AFM prediction. The magnetic coupling constant \mathcal{J} , remains unchanged in various situations, such as, increasing the U value, non-collinear spin orders or geometrical distortions of the chain.

To sum up, we show that electron correlation is a key feature to determine the magnetic properties of one-dimensional systems. The cRPA calculations show that different values of U are allowed for different atomic species depending on the configuration of the d orbital and the interaction with the substrate. In addition, a study over different U needs to be done to avoid missing the possible states with different orbital configurations. Magnetic properties in localized magnetism, are governed by the orbital occupations, hence, varying the orbital occupations can

alter the magnetic properties of the same atomic species. Metastable states are a handicap for the DFT+ U calculation, as the energy minimization procedure can get trapped in a local minimum. Therefore, methods like the OMC needs to be applied to facilitate finding the ground state.

Appendix A

Magnetic Anisotropy Energy (MAE) convergence test

A.1 Convergence details

The small value of the MAE in bulk ($\sim 10 \mu\text{eV}$) and low dimensional systems ($\sim 10 \text{ meV}$) impose a strict convergence criterion. We compute the MAE of the TMO chains for different energy cut-offs for the plane-wave basis, from 350 to 650 eV, with a step of 50 eV. and $25 \times 1 \times 1$, $35 \times 1 \times 1$ and $45 \times 1 \times 1$ k -point grids. For the DFT+SOC calculations, the convergence threshold of the total energy is set to 10^{-8} . The MAE can be considered converged by 500 eV, with subtle differences ($\sim \mu\text{eV}$) for higher cut-offs. All chains show a properly converged MAE for a $35 \times 1 \times 1$ k -grid, except the MnO_2 where 45 k -points are needed. To characterize the orbital partial occupation effects, we calculate the self-consistent MAE with the tetrahedron method¹ [194] and with Fermi-Dirac distribution for several values of the width, $\sigma = 0.02, 0.05, 0.1$ eV. In the FT approach, we use a Fermi smearing of $\sigma = 0.05$ eV width to consider an in-between value of the SCF.

In Tables A.1 to A.3 the resulting energy differences are shown. In the SCF calculations, the MAE shows little variation with the smearing, particularly in the FeO_2 chain. Considering that σ influences the partial occupations of orbitals, it is to be expected that the metallic systems, i.e., NiO_2 , and MnO_2 , are the ones that have a larger variation compared to the semimetallic CoO_2 and the insulating FeO_2 chains.

¹We say tetrahedron as it is the methods name, but as 1D instead of tetrahedron is *triangular*.

	MAE= $E^x - E^y$ (meV)				
	FT	Tetra	SCF		
	$\sigma = 0.05$ (eV)		$\sigma = 0.02$	$\sigma = 0.05$	$\sigma = 0.1$
NiO ₂	1.74	6.09	6.62	7.06	5.23
CoO ₂	0.40	0.57	0.57	0.58	0.59
FeO ₂	0.02	0.07	0.07	0.08	0.07
MnO ₂	0.23	0.32	0.29	0.25	0.21

Table A.1: XO₂ MAE between $x - y$ directions computed with a cut-off of 650 eV and a $45 \times 1 \times 1$ k -point mesh.

	MAE= $E^x - E^z$ (meV)				
	FT	Tetra	SCF		
	$\sigma = 0.05$ (eV)		$\sigma = 0.02$	$\sigma = 0.05$	$\sigma = 0.1$
NiO ₂	-0.29	-0.35	-0.36	-0.36	-0.33
CoO ₂	-0.12	-0.27	-0.26	-0.28	-0.30
FeO ₂	0.83	1.12	1.20	1.20	1.22
MnO ₂	0.31	0.64	0.59	0.52	0.51

Table A.2: Same as Table A.1 for directions $x - z$.

	MAE= $E^y - E^z$ (meV)				
	FT	Tetra	SCF		
	$\sigma = 0.05$ (eV)		$\sigma = 0.02$	$\sigma = 0.05$	$\sigma = 0.1$
NiO ₂	-2.04	-6.43	-6.98	-7.15	-5.57
CoO ₂	-0.51	-0.84	-0.83	-0.86	-0.86
FeO ₂	0.81	1.13	1.27	1.13	1.13
MnO ₂	0.54	0.96	0.88	0.78	0.96

Table A.3: Same as Table A.1 for directions $y - z$.

Appendix B

cRPA calculations

B.1 FLEUR and SPEX convergence parameters

A summary of the convergence parameters is given in Table B.1. The FLAPW wavefunctions are expanded up an the angular moment $l_{max} = 8, 6, 8$ for X, O and Ir atoms respectively, and the non-spherical contribution is set to $l_{max}^{nonsph} = l_{max} - 2$. In SPEX, the mixed basis product angular moment is set to $L_{max} = l_{max}/2$ and the plane wave energy cut-off is set to $0.75E_c^{wvf}$, where E_c^{wvf} is the plane-wave energy cut-off.

	MnO ₂	FeO ₂	CoO ₂	NiO ₂
R_{MT}^X (a.u.)	2.24(2.16)	2.28(2.14)	2.23(2.11)	2.23(2.11)
R_{MT}^O (a.u.)	1.27(1.22)	1.29(1.21)	1.26(1.19)	1.26(1.19)
R_{MT}^{Ir} (a.u.)	2.45	2.35	2.37	2.34
E_c^{wvf} (a.u. ⁻¹)	4.7(4.9)	4.5(5.0)	4.7(5.0)	4.6(4.5)
E_c^{pot} (a.u. ⁻¹)	14.2(14.7)	13.8(14.9)	14.2(14.9)	14.1(13.0)

Table B.1: Convergence parameter used in the FLAPW and SPEX calculations for the unsupported (supported) chains. The R are the muffin-tin radii where the local basis functions are considered for each atom. The energy cut-offs of the interstitial planes and potential are given by E_c^{wvf} and E_c^{pot} . Values between the parenthesis are for the supported case.

B.2 cRPA calculation results

In Table B.2 we give the converged U and J values at each spin channel combination. The maximum spread between the different spin channels is ~ 0.5 eV for the U value and ~ 0.15 eV for the J .

	$U^{\uparrow\uparrow}$	$U^{\uparrow\downarrow}$	$U^{\downarrow\downarrow}$	$J^{\uparrow\uparrow}$	$J^{\uparrow\downarrow}$	$J^{\downarrow\downarrow}$
MnO ₂	6.21	5.95	5.73	1.04	0.95	0.89
MnO ₂ /Ir(100)	3.78	3.53	3.33	0.98	0.88	0.83
FeO ₂	7.67	7.38	7.12	1.13	1.04	0.97
FeO ₂ /Ir	1.38	-	1.32	0.80	-	0.73
CoO ₂	5.73	5.58	5.45	1.11	1.05	1.00
CoO ₂ /Ir	2.39	-	-	0.90	-	-
NiO ₂ (C1)	6.59	6.49	6.38	1.17	1.13	1.10
NiO ₂ (C2)	2.41	2.40	2.39	1.01	1.00	1.00
NiO ₂ /Ir	1.71	-	1.70	0.87	-	0.86

Table B.2: Averaged screened Coulomb parameter for different spin channels. All values in eV.

MnO₂ with 3 layers of Ir(100)

We calculate the Hubbard- U interaction for a three-layered MnO₂/Ir system. We obtain $U = 3.86$ eV and $J = 1.00$ eV on a first iteration with cRPA. The obtained U value differs slightly by 0.12 eV from the two-layer case, suggesting that two layers are enough to characterize the screening due to Ir substrate. In Fig. B.1 we show the MLWFs band interpolation compared to the band structure obtained with FLEUR.

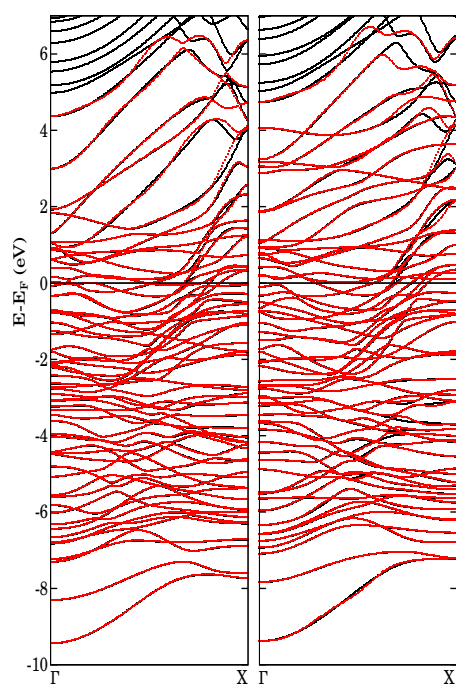


Figure B.1: Wannier band interpolation (FLAPW band structure) for MnO₂ with 3 layers of Ir in red (black).

Bibliography

- [1] Deung Jang Choi, Nicolas Lorente, Jens Wiebe, Kirsten Von Bergmann, Alexander F. Otte, and Andreas J. Heinrich. Colloquium: Atomic spin chains on surfaces. *Reviews of Modern Physics*, 91(4):041001, oct 2019. (Cited in pages 1 and 5.)
- [2] Brad S. Singer, Brian R. Jicha, Nobutatsu Mochizuki, and Robert S. Coe. Synchronizing volcanic, sedimentary, and ice core records of Earth’s last magnetic polarity reversal. *Science Advances*, 5(8):1–12, 2019. (Cited in page 2.)
- [3] Walther Gerlach and Otto Stern. Der experimentelle Nachweis der Richtungsquantelung im Magnetfeld. *Zeitschrift für Physik*, 9(1):349–352, 1922. (Cited in page 2.)
- [4] G. E. Uhlenbeck and S. Goudsmit. Ersetzung der Hypothese vom unmechanischen Zwang durch eine Forderung bezüglich des inneren Verhaltens jedes einzelnen Elektrons. *Die Naturwissenschaften*, 13(47):953–954, 1925. (Cited in page 2.)
- [5] Daniel C Mattis. *The theory of magnetism made simple: An introduction to physical concepts and to some useful mathematical methods*. 2006. (Cited in page 2.)
- [6] Joachim Stöhr and Hans Christoph Siegmann. *Magnetism: From fundamentals to nanoscale dynamics*, volume 152. 2006. (Cited in pages 2, 3 and 76.)
- [7] Tôru Moriya. Ferro- and antiferromagnetism of transition metals and alloys. *Solid State Communications*, 2(8):239–243, 1964. (Cited in page 3.)
- [8] R J Elliot Editor. *Magnetic Properties of Rare Earth Metals*. 1972. (Cited in page 3.)

-
- [9] Stefan Blügel and Gustav Bihlmayer. Magnetism of Low-dimensional Systems: Theory. In *Handbook of Magnetism and Advanced Magnetic Materials*. 2007. (Cited in pages 3, 5, 6, 23 and 35.)
- [10] Kei Yosida. *Theory of magnetism*. Springer-Verlag Berlin Heidelberg, 1996. (Cited in pages 3, 17, 52 and 89.)
- [11] W. Heisenberg. Zur Theorie des Ferromagnetismus. *Zeitschrift für Physik*, 49(9-10):619–636, 1928. (Cited in pages 3 and 5.)
- [12] M. Louis Néel. Propriétés magnétiques des ferrites ; ferrimagnétisme et antiferromagnétisme. *Annales de Physique*, 12(3):137–198, 1948. (Cited in page 3.)
- [13] Motor Technology. *Magnetic Materials : Domestic*. (Krebs), 1995. (Cited in page 3.)
- [14] Taeyoung Choi. Studies of single atom magnets via scanning tunneling microscopy. *Journal of Magnetism and Magnetic Materials*, 481(January):150–155, 2019. (Cited in page 4.)
- [15] David Reinsel, John Gantz, and John Rydning. The Digitization of the World - From Edge to Core. *Framingham: International Data Corporation*, (November):US44413318, 2018. (Cited in page 4.)
- [16] L. W. McKeehan. Physical theory of ferromagnetic domains [37]. *Physical Review*, 79(4):745, 1950. (Cited in page 4.)
- [17] Dieter Weller and Andreas Moser. Thermal effect limits in ultrahigh-density magnetic recording. *IEEE Transactions on Magnetics*, 35(6):4423–4439, 1999. (Cited in page 4.)
- [18] Joerg Appenzeller, Joachim Knoch, Mikael T. Björk, Heike Riel, Heinz Schmid, and Walter Riess. Toward nanowire electronics. *IEEE Transactions on Electron Devices*, 55(11):2827–2845, 2008. (Cited in page 4.)
- [19] Nihar Mohanty, David Moore, Zhiping Xu, T. S. Sreeprasad, Ashvin Nagaraja, Alfredo Alexander Rodriguez, and Vikas Berry. Nanotomy-based production of transferable and dispersible graphene nanostructures of controlled shape and size. *Nature Communications*, 3(May):844–848, 2012. (Cited in page 4.)

- [20] J. Schlappa, K. Wohlfeld, K. J. Zhou, M. Mourigal, M. W. Haverkort, V. N. Strocov, L. Hozoi, C. Monney, S. Nishimoto, S. Singh, A. Revcolevschi, J. S. Caux, L. Patthey, H. M. Rønnow, J. Van Den Brink, and T. Schmitt. Spin-orbital separation in the quasi-one-dimensional Mott insulator Sr 2 CuO3. *Nature*, 485(7396):82–85, 2012. (Cited in page 4.)
- [21] Svetlozar Surnev, Francesco Allegretti, Georg Parteder, Thomas Franz, Florian Mittendorfer, Jesper N. Andersen, and Falko P. Netzer. One-dimensional oxide-metal hybrid structures: Site-specific enhanced reactivity for CO oxidation. *ChemPhysChem*, 11(12):2506–2509, 2010. (Cited in page 4.)
- [22] Sebastian Loth, Susanne Baumann, Christopher P Lutz, D M Eigler, and Andreas J Heinrich. Bistability in Atomic-Scale Antiferromagnets. 335(January):196–200, 2012. (Cited in page 4.)
- [23] Pascal Ferstl, Lutz Hammer, Christopher Sobel, Matthias Gubo, Klaus Heinz, M. Alexander Schneider, Florian Mittendorfer, and Josef Redinger. Self-Organized Growth, Structure, and Magnetism of Monatomic Transition-Metal Oxide Chains. *Physical Review Letters*, 117(4):1–5, 2016. (Cited in pages 4, 7, 36, 37 and 40.)
- [24] Mario Ruben, Esther Breuning, Jean Marie Lehn, Vadim Ksenofontov, Franz Renz, Philip Gütllich, and Gavin B.M. Vaughan. Supramolecular spintronic devices: Spin transitions and magnetostructural correlations in [Fe4IIL4]8+ [2 × 2]-grid-type complexes. *Chemistry - A European Journal*, 9(18):4422–4429, 2003. (Cited in page 4.)
- [25] Marisa N. Faraggi, Vitaly N. Golovach, Sebastian Stepanow, Tzu Chun Tseng, Nasiba Abdurakhmanova, Christopher Seiji Kley, Alexander Langner, Violetta Sessi, Klaus Kern, and Andres Arnau. Modeling ferro- and antiferromagnetic interactions in metal-organic coordination networks. *Journal of Physical Chemistry C*, 119(1):547–555, 2015. (Cited in pages 4 and 75.)
- [26] Hassan Denawi, Mathieu Koudia, Roland Hayn, Olivier Siri, and Mathieu Abel. On-Surface Synthesis of Spin Crossover Polymeric Chains. *Journal of Physical Chemistry C*, 122(26):15033–15040, 2018. (Cited in pages 4 and 75.)
- [27] Hassan Denawi, Mathieu Abel, and Roland Hayn. Magnetic Polymer Chains of Transition Metal Atoms and Zwitterionic Quinone. *Journal of Physical Chemistry C*, 123(7):4582–4589, 2019. (Cited in page 4.)

- [28] Jing Liu, Yifan Gao, Tong Wang, Qiang Xue, Muqing Hua, Yongfeng Wang, Li Huang, and Nian Lin. Collective Spin Manipulation in Antiferroelastic Spin-Crossover Metallo-Supramolecular Chains. *ACS Nano*, 14(9):11283–11293, 2020. (Cited in page 4.)
- [29] A. Ayuela, H. Raebiger, M. J. Puska, and R. M. Nieminen. Spontaneous magnetization of aluminum nanowires deposited on the NaCl(100) surface. *Physical Review B - Condensed Matter and Materials Physics*, 66(3):1–8, 2002. (Cited in pages 5 and 35.)
- [30] N. D. Mermin and H. Wagner. Absence of ferromagnetism or antiferromagnetism in one- or two-dimensional isotropic Heisenberg models. *Physical Review Letters*, 17(22):1133–1136, 1966. (Cited in pages 5 and 35.)
- [31] Yi Cui, Xiangfeng Duan, Yu Huang, and Charles M. Lieber. *Nanowires as Building Blocks for Nanoscale Science and Technology*, volume 35. 2003. (Cited in page 5.)
- [32] Y. Huang, X. Duan, Y. Cui, L. J. Lauhon, K. H. Kim, and C. M. Lieber. Logic gates and computation from assembled nanowire building blocks. *Science*, 294(5545):1313–1317, 2001. (Cited in page 5.)
- [33] Yao Zhen, Henk W.Ch Postma, Leon Balents, and Cees Dekker. Carbon nanotube intramolecular junctions. *Nature*, 402(6759):273–276, 1999. (Cited in page 5.)
- [34] Sander J. Tans, Alwin R.M. Verschueren, and Cees Dekker. Room-temperature transistor based on a single carbon nanotube. *Nature*, 393(6680):49–52, 1998. (Cited in page 5.)
- [35] Pho Nguyen, Hou T. Ng, Toshishige Yamada, Michael K. Smith, Jun Li, Jie Han, and M. Meyyappan. Direct integration of metal oxide nanowire in vertical field-effect transistor. *Nano Letters*, 4(4):651–657, 2004. (Cited in page 5.)
- [36] Xiuzhen Yu, John P. Degraeve, Yuka Hara, Toru Hara, Song Jin, and Yoshinori Tokura. Observation of the magnetic skyrmion lattice in A MnSi nanowire by Lorentz TEM. *Nano Letters*, 13(8):3755–3759, 2013. (Cited in page 5.)
- [37] A. Manchon, J. Železný, I. M. Miron, T. Jungwirth, J. Sinova, A. Thiaville, K. Garello, and P. Gambardella. Current-induced spin-orbit torques in ferro-

- magnetic and antiferromagnetic systems. *Reviews of Modern Physics*, 91(3), 2019. (Cited in page 5.)
- [38] S. A. Wolf, D. D. Awschalom, R. A. Buhrman, J. M. Daughton, S. Von Molnár, M. L. Roukes, A. Y. Chtchelkanova, and D. M. Treger. Spintronics: A spin-based electronics vision for the future. *Science*, 294(5546):1488–1495, 2001. (Cited in page 5.)
- [39] Stuart S.P. Parkin, Masamitsu Hayashi, and Luc Thomas. Magnetic domain-wall racetrack memory. *Science*, 320(5873):190–194, 2008. (Cited in page 5.)
- [40] Zheng Duan, Andrew Smith, Liu Yang, Brian Youngblood, Jürgen Lindner, Vladislav E. Demidov, Sergej O. Demokritov, and Ilya N. Krivorotov. Nanowire spin torque oscillator driven by spin orbit torques. *Nature Communications*, 5:1–7, 2014. (Cited in page 5.)
- [41] Atsufumi Hirohata, Keisuke Yamada, Yoshinobu Nakatani, Lucian Prejbeanu, Bernard Diény, Philipp Pirro, and Burkard Hillebrands. Review on spintronics: Principles and device applications. *Journal of Magnetism and Magnetic Materials*, 509(March), 2020. (Cited in page 5.)
- [42] H W Yeom, S Takeda, E Rotenberg, I Matsuda, K Horikoshi, J Schaefer, C M Lee, S D Kevan, T Ohta, T Nagao, and S Hasegawa. Instability and charge density wave of metallic quantum chains on a silicon surface. *Physical Review Letters*, 82(24):4898–4901, 1999. (Cited in pages 5 and 75.)
- [43] F. J. Himpsel, J. E. Ortega, G. J. Mankey, and R. F. Willis. Magnetic nanostructures. *Advances in Physics*, 47(4):511–597, 1998. (Cited in page 5.)
- [44] P. Segovia, D. Purdle, M. Hengsberger, and Y. Baer. Observation of spin and charge collective modes in one-dimensional metallic chains. *Nature*, 402(6761):504–507, 1999. (Cited in page 5.)
- [45] P. Gambardella, M. Blanc, H. Brune, K. Kuhnke, and K. Kern. One-dimensional metal chains on Pt vicinal surfaces. *Physical Review B - Condensed Matter and Materials Physics*, 61(3):2254–2262, 2000. (Cited in page 5.)
- [46] Eigler DM and Schweizer EK. Positioning single atoms with scanning tunnelling microscope. *Nature*, 344(April):524, 1990. (Cited in page 5.)
- [47] Cyrus F. Hirjibehedin, Christopher P. Lutz, and Andreas J. Heinrich. Spin coupling in engineered atomic structures. *Science*, 312(5776):1021–1024, 2006. (Cited in page 5.)

- [48] Pietro Gambardella, A. Dallmeyer, K. Maiti, M. C. Malagoli, W. Eberhardt, K. Kern, and C. Carbone. Ferromagnetism in one-dimensional monatomic metal chains. *Nature*, 416(6878):301–304, 2002. (Cited in pages 5 and 35.)
- [49] M. A. Van Hove. Surface crystallography with low-energy electron diffraction. *Proceedings - Royal Society of London, A*, 442(1914):61–72, 1993. (Cited in page 5.)
- [50] J. Tersoff and D. R. Hamann. Theory of the scanning tunneling microscope. *Physical Review B*, 31(2):805–813, 1985. (Cited in page 5.)
- [51] Yigal Meir and Ned S. Wingreen. Landauer formula for the current through an interacting electron region. *Physical Review Letters*, 68(16):2512–2515, 1992. (Cited in page 5.)
- [52] B. C. Stipe, M. A. Rezaei, and W. Ho. Single-molecule vibrational spectroscopy and microscopy. *Science*, 280(5370):1732–1735, 1998. (Cited in page 5.)
- [53] Xingjiang Zhou, Shaolong He, Guodong Liu, Lin Zhao, Li Yu, and Wentao Zhang. New developments in laser-based photoemission spectroscopy and its scientific applications: A key issues review. *Reports on Progress in Physics*, 81(6), 2018. (Cited in page 5.)
- [54] Gerrit Van Der Laan. Microscopic origin of magnetocrystalline anisotropy in transition metal thin films. *Journal of Physics Condensed Matter*, 10(14):3239–3253, 1998. (Cited in pages 5, 24, 45 and 87.)
- [55] J Stöhr. Exploring the microscopic origin of magnetic anisotropies with X-ray magnetic circular dichroism (XMCD) spectroscopy. *Journal of Magnetism and Magnetic Materials*, 200:470–497, 1999. (Cited in pages 5, 45 and 87.)
- [56] A. J. Heinrich, J. A. Gupta, C. P. Lutz, and D. M. Eigler. Single-atom spin-flip spectroscopy. *Science*, 306(5695):466–469, 2004. (Cited in page 5.)
- [57] M. Bode. Spin-polarized scanning tunnelling microscopy. *Reports on Progress in Physics*, 66(4):523–582, 2003. (Cited in page 5.)
- [58] Roland Wiesendanger. Spin mapping at the nanoscale and atomic scale. *Reviews of Modern Physics*, 81(4):1495–1550, 2009. (Cited in page 5.)
- [59] Jens Wiebe, Lihui Zhou, and Roland Wiesendanger. Atomic magnetism revealed by spin-resolved scanning tunnelling spectroscopy. *Journal of Physics D: Applied Physics*, 44(46), 2011. (Cited in page 5.)

-
- [60] Fabian D. Natterer, Kai Yang, William Paul, Philip Willke, Taeyoung Choi, Thomas Greber, Andreas J. Heinrich, and Christopher P. Lutz. Reading and writing single-atom magnets. *Nature*, 543(7644):226–228, 2017. (Cited in page 5.)
- [61] H. Bethe. Zur Theorie der Metalle - I. Eigenwerte und Eigenfunktionen der linearen Atomkette. *Zeitschrift für Physik*, 71(3-4):205–226, 1931. (Cited in page 5.)
- [62] Jacques Des Cloizeaux and J. J. Pearson. Spin-wave spectrum of the antiferromagnetic linear chain. *Physical Review*, 128(5):2131–2135, 1962. (Cited in page 6.)
- [63] J. P. Gauyacq and N. Lorente. Excitation of spin waves by tunneling electrons in ferromagnetic and antiferromagnetic spin-1/2 Heisenberg chains. *Physical Review B - Condensed Matter and Materials Physics*, 83(3):1–13, 2011. (Cited in page 6.)
- [64] F. D.M. Haldane. Nonlinear field theory of large-spin Heisenberg antiferromagnets: Semiclassically quantized solitons of the one-dimensional easy-axis Néel state. *Physical Review Letters*, 50(15):1153–1156, 1983. (Cited in page 6.)
- [65] O. K. Andersen. Linear methods in band theory. *Phys. Rev. B - Condens. Matter Mater. Phys.*, 12(8), 1975. (Cited in pages 6 and 24.)
- [66] M. Weinert, R. E. Watson, and J. W. Davenport. Total-energy differences and eigenvalue sums. *Physical Review B*, 32(4):2115–2119, 1985. (Cited in page 6.)
- [67] Vladimir I Anisimov, F Aryasetiawan, and A I Lichtenstein. First-principles calculations of the electronic structure and spectra of strongly correlated systems: The LDA + U method. *Journal of Physics Condensed Matter*, 9(4):767–808, 1997. (Cited in pages 6, 17 and 26.)
- [68] J. P. Perdew and Alex Zunger. Self-interaction correction to density-functional approximations for many-electron systems. *Physical Review B*, 23(10):5048–5079, 1981. (Cited in page 6.)
- [69] A. Svane and O. Gunnarsson. Localization in the self-interaction-corrected density-functional formalism. *Physical Review B*, 37(16):9919–9922, 1988. (Cited in page 6.)

- [70] A. Svane and O. Gunnarsson. Transition-metal oxides in the self-interaction corrected density-functional formalism. *Physical Review Letters*, 65(9):1148–1151, 1990. (Cited in page 6.)
- [71] J. Hubbard. Electron correlations in narrow energy bands. *Proceedings of the Royal Society of London. Series A. Mathematical and Physical Sciences*, 276(1365):238–257, 1963. (Cited in pages 6, 17 and 51.)
- [72] A. B. Shick, W. E. Pickett, and A. I. Liechtenstein. Ground and metastable states in γ -Ce from correlated band theory. *Journal of Electron Spectroscopy and Related Phenomena*, 114-116:753–758, 2001. (Cited in pages 6 and 76.)
- [73] Jeremy P. Allen and Graeme W. Watson. Occupation matrix control of d- and f-electron localisations using DFT + U. *Physical Chemistry Chemical Physics*, 16(39):21016–21031, 2014. (Cited in pages 6, 22 and 76.)
- [74] Martin Schmitt, Chong H. Park, Paula Weber, Andreas Jäger, Jeannette Kemmer, Matthias Vogt, and Matthias Bode. Structural and magnetic properties of 3d transition metal oxide chains on the (001) surfaces of Ir and Pt. *Physical Review B*, 100(5):54431, 2019. (Cited in pages 7, 36 and 40.)
- [75] Vijai M. Santhini, Christian Wäckerlin, Aleš Čahlík, Martin Ondráček, Simon Pascal, Adam Matěj, Oleksandr Stetsovych, Pingo Mutombo, Petr Lazar, Olivier Siri, and Pavel Jelínek. 1D Coordination π -d Conjugated Polymers with Distinct Structures Defined by the Choice of the Transition Metal: Towards a New Class of Antiaromatic Macrocycles. *Angewandte Chemie - International Edition*, 60(1):439–445, 2021. (Cited in pages 7 and 76.)
- [76] M Born and R J Oppenheimer. On the quantum theory of molecules (English translation). *Annalen der Physik*, 457(1927):1–32, 1927. (Cited in page 10.)
- [77] Neil W. Ashcroft and David Mermin. *Solid State Physics*. 1978. (Cited in page 10.)
- [78] V. Fock. Näherungsmethode zur Lösung des quantenmechanischen Mehrkörperproblems. *Zeitschrift für Physik*, 61(1-2):126–148, 1930. (Cited in page 11.)
- [79] J. C. Slater. The theory of complex spectra. *Physical Review*, 34(10):1293–1322, nov 1929. (Cited in page 11.)

-
- [80] P Hohenberg and W Kohn. Inhomogeneous Electron Gas. *Physical Review*, 136(3B):B864—B871, nov 1964. (Cited in page 12.)
- [81] W. Kohn and L. J. Sham. Self-Consistent Equations Including Exchange and Correlation Effects. *Physical Review*, 140(4A):A1133–A1138, nov 1965. (Cited in pages 13 and 15.)
- [82] Richard M. Martin. *Electronic Structure Basic Theory and Practical Methods*. Cambridge University Press, apr 2004. (Cited in page 15.)
- [83] B. Hammer, L. B. Hansen, and J. K. Nørskov. Improved adsorption energetics within density-functional theory using revised Perdew-Burke-Ernzerhof functionals. *Physical Review B - Condensed Matter and Materials Physics*, 59(11):7413–7421, mar 1999. (Cited in page 15.)
- [84] John P Perdew, Kieron Burke, and Matthias Ernzerhof. Generalized gradient approximation made simple. *Physical Review Letters*, 77(18):3865–3868, 1996. (Cited in pages 15, 37 and 77.)
- [85] Axel D. Becke. A new mixing of Hartree-Fock and local density-functional theories. *The Journal of Chemical Physics*, 98(2):1372–1377, jan 1993. (Cited in page 15.)
- [86] Jochen Heyd, Gustavo E. Scuseria, and Matthias Ernzerhof. Hybrid functionals based on a screened Coulomb potential. *Journal of Chemical Physics*, 118(18):8207–8215, 2003. (Cited in page 16.)
- [87] Aliaksandr V. Krukau, Oleg A. Vydrov, Artur F. Izmaylov, and Gustavo E. Scuseria. Influence of the exchange screening parameter on the performance of screened hybrid functionals. *Journal of Chemical Physics*, 125(22):224106, dec 2006. (Cited in page 16.)
- [88] U. Von Barth and L. Hedin. A local exchange-correlation potential for the spin polarized case. I. *Journal of Physics C: Solid State Physics*, 5(13):1629–1642, 1972. (Cited in page 16.)
- [89] Gustav Bihlmayer. Density Functional Theory for Magnetism and Magnetic Anisotropy. *Handbook of Materials Modeling*, pages 895–917, 2020. (Cited in pages 16 and 23.)
- [90] A. Rohrbach, J. Hafner, and G. Kresse. Electronic correlation effects in transition-metal sulfides. *Journal of Physics Condensed Matter*, 15(6):979–996, 2003. (Cited in page 17.)

- [91] N. F. Mott. The basis of the electron theory of metals, with special reference to the transition metals. *Proceedings of the Physical Society. Section A*, 62(7):416–422, jul 1949. (Cited in pages 17 and 51.)
- [92] J. H. De Boer and E. J.W. Verwey. Semi-conductors with partially and with completely filled 3d-lattice bands. *Proceedings of the Physical Society*, 49(4S):59–71, aug 1937. (Cited in pages 17 and 51.)
- [93] A. M. Oleś. Correlation effects in the cohesion and magnetic properties of transition metals. *Physical Review B*, 23(1):271–278, 1981. (Cited in page 17.)
- [94] A. M. Oles and G. Stollhoff. Correlation effects in ferromagnetism of transition metals. *Physical Review B*, 29(1):314–327, 1984. (Cited in page 17.)
- [95] Vladimir I. Anisimov, Jan Zaanen, and Ole K. Andersen. Band theory and Mott insulators: Hubbard U instead of Stoner I. *Physical Review B*, 44(3):943–954, 1991. (Cited in pages 17, 18 and 87.)
- [96] V. I. Anisimov, I. V. Solovyev, M. A. Korotin, M. T. Czyzyk, and G. A. Sawatzky. Density-functional theory and NiO photoemission spectra. *Physical Review B*, 48(23):16929–16934, 1993. (Cited in pages 17, 18 and 58.)
- [97] A. I. Liechtenstein, V. I. Anisimov, and J. Zaanen. Density-functional theory and strong interactions: Orbital ordering in Mott-Hubbard insulators. *Physical Review B*, 52(8):5467–5471, 1995. (Cited in pages 17 and 18.)
- [98] A. B. Shick, A. I. Liechtenstein, and W. E. Pickett. Implementation of the LDA+U method using the full-potential linearized augmented plane-wave basis. *Physical Review B - Condensed Matter and Materials Physics*, 60(15):10763–10769, 1999. (Cited in pages 17 and 54.)
- [99] P. Mohn, C. Persson, P. Blaha, K. Schwarz, P. Novák, and H. Eschrig. Correlation induced paramagnetic ground state in FeAl. *Physical Review Letters*, 87(19):1–4, 2001. (Cited in page 18.)
- [100] A. G. Petukhov, I. I. Mazin, L. Chioncel, and A. I. Liechtenstein. Correlated metals and the LDA + U method. *Physical Review B - Condensed Matter and Materials Physics*, 67(15):1531061–1531064, 2003. (Cited in pages 18 and 54.)
- [101] M. T. Czyzyk and G. A. Sawatzky. Local-density functional and on-site correlations: The electronic structure of La₂CuO₄ and LaCuO₃. *Physical Review B*, 49(20):14211–14228, 1994. (Cited in page 18.)

- [102] S. Dudarev and G. Botton. Electron-energy-loss spectra and the structural stability of nickel oxide: An LSDA+U study. *Physical Review B - Condensed Matter and Materials Physics*, 57(3):1505–1509, 1998. (Cited in pages 18, 38 and 77.)
- [103] Felix Bloch. Über die Quantenmechanik der Elektronen in Kristallgittern. *Zeitschrift für Physik*, 52(7-8):555–600, 1929. (Cited in page 19.)
- [104] P. E. Blöchl. Projector augmented-wave method. *Physical Review B*, 50(24):17953–17979, 1994. (Cited in page 19.)
- [105] D. Joubert. From ultrasoft pseudopotentials to the projector augmented-wave method. *Physical Review B - Condensed Matter and Materials Physics*, 59(3):1758–1775, jan 1999. (Cited in page 19.)
- [106] E. Wimmer, H. Krakauer, M. Weinert, and A. J. Freeman. Full-potential self-consistent linearized-augmented-plane-wave method for calculating the electronic structure of molecules and surfaces: O₂ molecule. *Physical Review B*, 24(2):864–875, 1981. (Cited in page 20.)
- [107] S. Blügel and G. Bihlmayer. Full-Potential linearized augmented planewave method. *Computational Nanoscience*, 31:85–129, 2006. (Cited in page 20.)
- [108] E. Abate and M. Asdente. Tight-binding calculation of 3d bands of fe with and without spin-orbit coupling. *Physical Review*, 140(4A), 1965. (Cited in pages 22 and 46.)
- [109] C. Elsasser, M. Fahnle, E. H. Brandt, and M. C. Bohm. Theory of local magnetic anisotropy in amorphous alloys. *Journal of Physics F: Metal Physics*, 18(11):2463–2477, 1988. (Cited in pages 22 and 46.)
- [110] María Blanco-Rey, Paolo Perna, Adrian Gudin, Jose Manuel Diez, Alberto Anadón, Pablo Olleros-Rodríguez, Leticia De Melo Costa, Manuel Valvidares, Pierluigi Gargiani, Alejandra Guedeja-Marron, Mari-ona Cabero, María Varela, Carlos García-Fernández, Mikhail M. Otrokov, Julio Camarero, Rodolfo Miranda, Andrés Arnau, and Jorge I. Cerdá. Large Perpendicular Magnetic Anisotropy in Nanometer-Thick Epitaxial Graphene/Co/Heavy Metal Heterostructures for Spin-Orbitronics Devices. *ACS Applied Nano Materials*, 4(5):4398–4408, 2021. (Cited in page 23.)
- [111] Soner Steiner, Sergii Khmelevskyi, Martijn Marsmann, and Georg Kresse. Calculation of the magnetic anisotropy with projected-augmented-wave

- methodology and the case study of disordered Fe_{1-x}Co_x alloys. *Physical Review B*, 93(22):1–6, 2016. (Cited in page 24.)
- [112] H. Takayama, Klaus-Peter Bohnen, and Peter Fulde. Magnetic surface anisotropy of transition metals. *Physical Review B - Condensed Matter and Materials Physics*, 14(12):12–15, 1976. (Cited in page 24.)
- [113] Liqin Ke and Mark Van Schilfhaarde. Band-filling effect on magnetic anisotropy using a Green's function method. *Physical Review B - Condensed Matter and Materials Physics*, 92(1):1–9, 2015. (Cited in pages 24 and 87.)
- [114] Patrick Bruno. Tight-binding approach to the orbital magnetic moment and magneto crystalline anisotropy. *Physical Review B*, 39(1):865, 1989. (Cited in pages 24, 45 and 87.)
- [115] G. H.O. Daalderop, P. J. Kelly, and M. F.H. Schuurmans. First-principles calculation of the magnetocrystalline anisotropy energy of iron, cobalt, and nickel. *Physical Review B*, 41(17):11919–11937, 1990. (Cited in page 24.)
- [116] M. Blanco-Rey, J. I. Cerdá, and A. Arnau. Validity of perturbative methods to treat the spin-orbit interaction: Application to magnetocrystalline anisotropy. *New Journal of Physics*, 21(7), 2019. (Cited in pages 25 and 43.)
- [117] O. Gunnarsson, O. K. Andersen, O. Jepsen, and J. Zaanen. Density-functional calculation of the parameters in the Anderson model: Application to Mn in CdTe. *Physical Review B*, 39(3):1708–1722, 1989. (Cited in pages 26 and 52.)
- [118] A. K. McMahan, Richard M. Martin, and S. Satpathy. Calculated effective Hamiltonian for La₂CuO₄ and solution in the impurity Anderson approximation. *Physical Review B*, 38(10):6650–6666, 1988. (Cited in page 26.)
- [119] F. Aryasetiawan, K. Karlsson, O. Jepsen, and U. Schönberger. Calculations of Hubbard U from first-principles. *Physical Review B - Condensed Matter and Materials Physics*, 74(12):1–9, 2006. (Cited in pages 26 and 53.)
- [120] Matteo Cococcioni and Stefane De Gironcoli. Linear response approach to the calculation of the effective interaction parameters in the LDA+U method. *Physical Review B - Condensed Matter and Materials Physics*, 71(3):1–16, 2005. (Cited in pages 26 and 52.)
- [121] M. Springer and F. Aryasetiawan. Frequency-dependent screened interaction in Ni within the random-phase approximation. *Physical Review B -*

- Condensed Matter and Materials Physics*, 57(8):4364–4368, 1998. (Cited in pages 26 and 27.)
- [122] F. Aryasetiawan, M. Imada, A. Georges, G. Kotliar, S. Biermann, and A. I. Lichtenstein. Frequency-dependent local interactions and low-energy effective models from electronic structure calculations. *Physical Review B - Condensed Matter and Materials Physics*, 70(19):1–8, 2004. (Cited in pages 26, 28 and 53.)
- [123] Takashi Miyake and F. Aryasetiawan. Screened Coulomb interaction in the maximally localized Wannier basis. *Physical Review B - Condensed Matter and Materials Physics*, 77(8):1–9, 2008. (Cited in pages 26 and 53.)
- [124] Richard D. Mattuck. *A Guide to Feynman Diagrams in the Many-Body Problem (2nd edn)*. McGraw-Hill, 1976. (Cited in page 26.)
- [125] Takashi Miyake, Ferdi Aryasetiawan, and Masatoshi Imada. Ab initio procedure for constructing effective models of correlated materials with entangled band structure. *Physical Review B - Condensed Matter and Materials Physics*, 80(15):1–6, 2009. (Cited in page 28.)
- [126] Ersoy Şaşıoğlu, Christoph Friedrich, and Stefan Blügel. Effective Coulomb interaction in transition metals from constrained random-phase approximation. *Physical Review B - Condensed Matter and Materials Physics*, 83(12), 2011. (Cited in pages 28 and 30.)
- [127] Ersoy Şaşıoğlu, Christoph Friedrich, and Stefan Blügel. Strength of the effective coulomb interaction at metal and insulator surfaces. *Physical Review Letters*, 109(14), 2012. (Cited in pages 29, 52 and 61.)
- [128] Christoph Friedrich, Stefan Blügel, and Arno Schindlmayr. Efficient implementation of the GW approximation within the all-electron FLAPW method. *Physical Review B - Condensed Matter and Materials Physics*, 81(12):1–16, 2010. (Cited in pages 30 and 54.)
- [129] Giovanni Pizzi, Valerio Vitale, Ryotaro Arita, Stefan Blügel, Frank Freimuth, Guillaume Géranton, Marco Gibertini, Dominik Gresch, Charles Johnson, Takashi Koretsune, Julen Ibañeta-Azpiroz, Hyungjun Lee, Jae Mo Lihm, Daniel Marchand, Antimo Marrazzo, Yuriy Mokrousov, Jamal I. Mustafa, Yoshiro Nohara, Yusuke Nomura, Lorenzo Paulatto, Samuel Poncé, Thomas Ponweiser, Junfeng Qiao, Florian Thöle, Stepan S. Tsirkin, Małgorzata Wierzbowska, Nicola Marzari, David Vanderbilt, Ivo Souza,

- Arash A. Mostofi, and Jonathan R. Yates. Wannier90 as a community code: New features and applications. *Journal of Physics Condensed Matter*, 32(16), 2020. (Cited in page 30.)
- [130] Christoph Friedrich, Arno Schindlmayr, and Stefan Blügel. Efficient calculation of the Coulomb matrix and its expansion around $k = 0$ within the FLAPW method. *Computer Physics Communications*, 180(3):347–359, 2009. (Cited in page 30.)
- [131] Gregory H. Wannier. The structure of electronic excitation levels in insulating crystals. *Physical Review*, 52(3):191–197, 1937. (Cited in page 30.)
- [132] Nicola Marzari, Arash A. Mostofi, Jonathan R. Yates, Ivo Souza, and David Vanderbilt. Maximally localized Wannier functions: Theory and applications. *Reviews of Modern Physics*, 84(4):1419–1475, oct 2012. (Cited in pages 30 and 54.)
- [133] Nicola Marzari and David Vanderbilt. Maximally localized generalized Wannier functions for composite energy bands. *Physical Review B - Condensed Matter and Materials Physics*, 56(20):12847–12865, 1997. (Cited in page 32.)
- [134] E. I. Blount. Formalisms of Band Theory. *Solid State Physics - Advances in Research and Applications*, 13(C), 1962. (Cited in page 32.)
- [135] Ivo Souza, Nicola Marzari, and David Vanderbilt. Maximally localized Wannier functions for entangled energy bands. *Physical Review B - Condensed Matter and Materials Physics*, 65(3):1–13, 2002. (Cited in page 33.)
- [136] Susanne Schulz, Ilya A. Nechaev, Monika Güttler, Georg Poelchen, Alexander Generalov, Steffen Danzenbächer, Alla Chikina, Silvia Seiro, Kristin Kliemt, Alexandra Yu Vyazovskaya, Timur K. Kim, Pavel Dudin, Evgueni V. Chulkov, Clemens Laubschat, Eugene E. Krasovskii, Christoph Geibel, Cornelius Krellner, Kurt Kummer, and Denis V. Vyalikh. Emerging 2D-ferromagnetism and strong spin-orbit coupling at the surface of valence-fluctuating EuIr₂Si₂. *npj Quantum Materials*, 4(1), 2019. (Cited in page 35.)
- [137] S. Blügel, B. Drittler, R. Zeller, and P. H. Dederichs. Magnetic properties of 3 d transition metal monolayers on metal substrates. *Applied Physics A Solids and Surfaces*, 49(6):547–562, 1989. (Cited in page 35.)
- [138] P. Gambardella, A. Dallmeyer, K. Maiti, M. C. Malagoli, S. Rusponi, P. Ohresser, W. Eberhardt, C. Carbone, and K. Kern. Oscillatory mag-

- netic anisotropy in one-dimensional atomic wires. *Physical Review Letters*, 93(7):7–10, 2004. (Cited in page 35.)
- [139] P. Lang, V. S. Stepanyuk, K. Wildberger, R. Zeller, and P. H. Dederichs. Local moments of 3d, 4d, and 5d atoms at Cu and Ag (001) surfaces. *Solid State Communications*, 92(9), 1994. (Cited in page 35.)
- [140] A M Lambowitz, Spring Harbor, Cold Spring Harbor, H Guo, P Perlman, A Lambowitz, W Seo, S Zimmerly, F Michel, K Halanych, J Boore, F Michel, F Michel, E Westhof, T Mitros, A Pyle, H Murray, H Zhou, B Turczyk, K Jarrell, A Pyle, J Sanfilippo, R Singh, M Matsuura, A Lambowitz, M Podar, U Stahl, P Perlman, S Hamill, A Pyle, G Hausner, S Zimmerly, A Robart, J Christianson, S Zimmerly, D Mindell, V Chu, A Pyle, P Perlman, F Michel, M Norgren, J Smith, S Sheriff, R Rambo, R Batey, J Kieft, M Zhang, C Peebles, F Michel, A De Lencastre, A Pyle, A Jacquier, F Michel, A Pyle, F Michel, A Pyle, O Fedorova, C Waldsich, S Holbrook, M Stahley, A Kosek, J Wang, S Strobel, J Doudna, A Jacquier, J Piccirilli, J Steitz, S Strobel, H De Bondt, A Pardi, S Holbrook, E Westhof, P Perlman, P Perlman, R Fong, J Piccirilli, R Padgett, G Wuenschell, J Termini, R Lin, C Guthrie, E Koonin, N Sukumar, J Osipiuk, C Whalen, A Saxena, W Shi, M Stahley, M Stahley, J Cochrane, J Cabral, O Fedorova, and R Batey. Revealing Magnetic Interactions from Single-Atom Magnetization Curves. *Science*, 320(April):82–87, 2008. (Cited in page 35.)
- [141] B. Dieny and M. Chshiev. Perpendicular magnetic anisotropy at transition metal/oxide interfaces and applications. *Reviews of Modern Physics*, 89(2), 2017. (Cited in page 36.)
- [142] S. Ikeda, K. Miura, H. Yamamoto, K. Mizunuma, H. D. Gan, M. Endo, S. Kanai, J. Hayakawa, F. Matsukura, and H. Ohno. A perpendicular-anisotropy CoFeB-MgO magnetic tunnel junction. *Nature Materials*, 9(9):721–724, 2010. (Cited in page 36.)
- [143] S. F. Zhang, W. L. Gan, J. Kwon, F. L. Luo, G. J. Lim, J. B. Wang, and W. S. Lew. Highly Efficient Domain Walls Injection in Perpendicular Magnetic Anisotropy Nanowire. *Scientific Reports*, 6(April):1–8, 2016. (Cited in page 36.)
- [144] Martin Schmitt, Paolo Moras, Gustav Bihlmayer, Ryan Cotsakis, Matthias Vogt, Jeannette Kemmer, Abderrezak Belabbes, Polina M. Sheverdyeva, Asish K. Kundu, Carlo Carbone, Stefan Blügel, and Matthias Bode. Indirect

- chiral magnetic exchange through Dzyaloshinskii–Moriya-enhanced RKKY interactions in manganese oxide chains on Ir(100). *Nature Communications*, 10(1):1–6, 2019. (Cited in pages 36 and 40.)
- [145] P. W. Anderson. Antiferromagnetism. Theory of superexchange interaction. *Physical Review*, 79(2):350–356, 1950. (Cited in pages 40 and 52.)
- [146] P. W. Anderson. New approach to the theory of superexchange interactions. *Physical Review*, 115(1):2–13, 1959. (Cited in page 40.)
- [147] Piotr Błoński and Jürgen Hafner. Density-functional theory of the magnetic anisotropy of nanostructures: An assessment of different approximations. *Journal of Physics Condensed Matter*, 21(42), 2009. (Cited in page 43.)
- [148] Piotr Błoński, Anne Lehnert, Samuel Dennler, Stefano Rusponi, Markus Etzkorn, Géraud Moulas, Peter Bencok, Pietro Gambardella, Harald Brune, and Jürgen Hafner. Magnetocrystalline anisotropy energy of Co and Fe adatoms on the (111) surfaces of Pd and Rh. *Physical Review B - Condensed Matter and Materials Physics*, 81(10):1–18, 2010. (Cited in page 43.)
- [149] Allan H. Morrish. *The physical principles of magnetism*. 2001. (Cited in pages 43 and 86.)
- [150] Dadi Dai, Hongjun Xiang, and Myung Hwan Whangbo. Effects of spin-orbit coupling on magnetic properties of discrete and extended magnetic systems. *Journal of Computational Chemistry*, 29(13):2187–2209, 2008. (Cited in pages 43 and 86.)
- [151] M. Capone, M. Fabrizio, C. Castellani, and E. Tosatti. Strongly correlated superconductivity. *Science*, 296(5577):2364–2366, 2002. (Cited in page 51.)
- [152] A. P. Ramirez. Colossal magnetoresistance. *Journal of Physics Condensed Matter*, 9(39):8171–8199, 1997. (Cited in page 51.)
- [153] Sang Wook Cheong. Transition metal oxides: The exciting world of orbitals. *Nature Materials*, 6(12):927–928, 2007. (Cited in page 51.)
- [154] Jan M. Tomczak and Silke Biermann. Optical properties of correlated materials: Generalized Peierls approach and its application to VO₂. *Physical Review B - Condensed Matter and Materials Physics*, 80(8):1–13, 2009. (Cited in page 51.)
- [155] Bernard Raveau. Strongly correlated electron systems: From chemistry to physics. *Comptes Rendus Chimie*, 14(9):856–864, 2011. (Cited in page 51.)

- [156] D. B. McWhan, A. Menth, J. P. Remeika, W. F. Brinkman, and T. M. Rice. Metal-insulator transitions in pure and doped V₂O₃. *Physical Review B*, 7(5):1920–1931, 1973. (Cited in page 51.)
- [157] J. Zaanen, G. A. Sawatzky, and J. W. Allen. Band gaps and electronic structure of transition-metal compounds. *Physical Review Letters*, 55(4), 1985. (Cited in pages 52 and 62.)
- [158] V. I. Anisimov, M. A. Korotin, and E. Z. Kurmaev. Band-structure description of Mott insulators (NiO, MnO, FeO, CoO). *Journal of Physics: Condensed Matter*, 2(17):3973–3987, 1990. (Cited in page 52.)
- [159] P. Kuiper, G. Kruizinga, J. Ghijsen, G. A. Sawatzky, and H. Verweij. Character of Holes in Li_xNi_{1-x}O and Their Magnetic Behavior. *Physical Review Letters*, 62(10):1214–1214, 1989. (Cited in page 52.)
- [160] D. M. Duffy and A. M. Stoneham. Conductivity and 'negative U' for ionic grain boundaries. *Journal of Physics C: Solid State Physics*, 16(21):4087–4092, 1983. (Cited in pages 52 and 66.)
- [161] G. A. Sawatzky and T. Hibma. Reduction of coulomb and charge-transfer energies in oxide films on metals. *Physical Review B - Condensed Matter and Materials Physics*, 59(4):R2517–R2520, 1999. (Cited in pages 52, 58 and 66.)
- [162] J. Van Den Brink and G. A. Sawatzky. Non-conventional screening of the Coulomb interaction in low-dimensional and finite-size systems. *Europhysics Letters*, 50(4):447–453, 2000. (Cited in page 52.)
- [163] Jack Deslippe, Mario Dipoppa, David Prendergast, Marcus V.O. Moutinho, Rodrigo B. Capaz, and Steven G. Louie. Electron - Hole interaction in carbon nanotubes: Novel screening and exciton excitation spectra. *Nano Letters*, 9(4):1330–1334, 2009. (Cited in page 52.)
- [164] M. R. Norman. Band theory and the insulating gap in CoO. *Physical Review B*, 40(15):10632–10634, 1989. (Cited in page 52.)
- [165] Lars Hedin. New method for calculating the one-particle Green's function with application to the electron-gas problem. *Physical Review*, 139(3A):618–622, 1965. (Cited in page 52.)
- [166] F. Aryasetiawan and O. Gunnarsson. The GW method. *Reports on Progress in Physics*, 61(3):237–312, 1998. (Cited in page 52.)

-
- [167] A. Lichtenstein and M. Katsnelson. Ab initio calculations of quasiparticle band structure in correlated systems: LDA++ approach. *Physical Review B - Condensed Matter and Materials Physics*, 57(12):6884–6895, 1998. (Cited in page 52.)
- [168] Chr Møller and M. S. Plesset. Note on an approximation treatment for many-electron systems. *Physical Review*, 46(7):618–622, 1934. (Cited in page 52.)
- [169] D. C. Langreth and J. P. Perdew. The exchange-correlation energy of a metallic surface. *Solid State Communications*, 17(11):1425–1429, 1975. (Cited in page 52.)
- [170] G. Kotliar, S. Y. Savrasov, K. Haule, V. S. Oudovenko, O. Parcollet, and C. A. Marianetti. Electronic structure calculations with dynamical mean-field theory. *Reviews of Modern Physics*, 78(3):865–951, 2006. (Cited in page 52.)
- [171] S. Biermann, F. Aryasetiawan, and A. Georges. First-Principles Approach to the Electronic Structure of Strongly Correlated Systems: Combining the [Formula presented] Approximation and Dynamical Mean-Field Theory. *Physical Review Letters*, 90(8):4, 2003. (Cited in page 52.)
- [172] Silke Biermann. Dynamical screening effects in correlated electron materials - A progress report on combined many-body perturbation and dynamical mean field theory: 'GW + DMFT'. *Journal of Physics Condensed Matter*, 26(17), 2014. (Cited in page 52.)
- [173] E. Antonides, E. C. Janse, and G. A. Sawatzky. LMM Auger spectra of Cu, Zn, Ga, and Ge. I. Transition probabilities, term splittings, and effective Coulomb interaction. *Physical Review B*, 15(4):1669–1679, 1977. (Cited in page 52.)
- [174] G. A. Sawatzky. Quasiatomic auger spectra in narrow-band metals. *Physical Review Letters*, 39(8):504–507, 1977. (Cited in page 52.)
- [175] D van der Marel and G.A. Sawatzky. Electron-electron interaction and localization in d and f transition metals. *Physical Review B*, 37(18):674–684, 1988. (Cited in pages 52 and 58.)
- [176] I. V. Solovyev and P. H. Dederichs. Ab initio calculations of Coulomb U parameters for transition-metal impurities. *Physical Review B*, 49(10):6736–6740, 1994. (Cited in page 52.)

- [177] Iurii Timrov, Nicola Marzari, and Matteo Cococcioni. Hubbard parameters from density-functional perturbation theory. *Physical Review B*, 98(8):1–15, 2018. (Cited in page 52.)
- [178] J. Zaanen and G. A. Sawatzky. Systematics in band gaps and optical spectra of 3D transition metal compounds. *Journal of Solid State Chemistry*, 88(1):8–27, 1990. (Cited in page 58.)
- [179] F. M.F. De Groot, J. C. Fuggle, B. T. Thole, and G. A. Sawatzky. 2p x-ray absorption of 3d transition-metal compounds: An atomic multiplet description including the crystal field. *Physical Review B*, 42(9):5459–5468, sep 1990. (Cited in page 58.)
- [180] Priyanka Seth, Philipp Hansmann, Ambroise Van Roekeghem, Loig Vaugier, and Silke Biermann. Towards a First-Principles Determination of Effective Coulomb Interactions in Correlated Electron Materials: Role of Intershell Interactions. *Physical Review Letters*, 119(5):1–7, 2017. (Cited in page 63.)
- [181] Lei Dong, Zi’Ang A. Gao, and Nian Lin. Self-assembly of metal–organic coordination structures on surfaces. *Progress in Surface Science*, 91(3):101–135, 2016. (Cited in page 75.)
- [182] María. Blanco-Rey, Ane Sarasola, Corneliu Nistor, Luca Persichetti, Christian Stamm, Cinthia Piamonteze, Pietro Gambardella, Sebastian Stepanow, Mikhail M. Otrokov, Vitaly N. Golovach, and Andres Arnau. Magnetic properties of metal–organic coordination networks based on 3d transition metal atoms. *Molecules*, 23(4):1–18, 2018. (Cited in page 75.)
- [183] Benjamin Mallada, Piotr Błoński, Rostislav Langer, Pavel Jelínek, Michal Otyepka, and Bruno De La Torre. On-Surface Synthesis of One-Dimensional Coordination Polymers with Tailored Magnetic Anisotropy. *ACS Applied Materials and Interfaces*, 13(27):32393–32401, 2021. (Cited in page 75.)
- [184] Z. H. Xiong, Di Wu, Z. Valy Vardeny, and Jing Shi. Giant magnetoresistance in organic spin-valves. *Nature*, 427(6977):821–824, 2004. (Cited in page 76.)
- [185] Jean-François Létard, Philippe Guionneau, and Laurence Goux-Capes. Towards Spin Crossover Applications. *Spin Crossover in Transition Metal Compounds III*, 1:221–249, 2006. (Cited in page 76.)
- [186] Hongjun Xiang, Jinlong Yang, J. G. Hou, and Qingshi Zhu. One-dimensional transition metal-benzene sandwich polymers: Possible ideal conductors for

- spin transport. *Journal of the American Chemical Society*, 128(7):2310–2314, 2006. (Cited in page 76.)
- [187] Yiyin Mao, Gaoran Li, Yi Guo, Zhoupeng Li, Chengdu Liang, Xincheng Peng, and Zhan Lin. Foldable interpenetrated metal-organic frameworks/carbon nanotubes thin film for lithium-sulfur batteries. *Nature Communications*, 8, 2017. (Cited in page 76.)
- [188] Philipp Gütllich, Yann Garcia, and Harold A. Goodwin. Spin crossover phenomena in Fe(II) complexes. *Chemical Society Reviews*, 29(6):419–427, 2000. (Cited in page 76.)
- [189] Alexander B. Shick, Václav Janiš, Václav Drchal, and Warren E. Pickett. Spin and orbital magnetic state of UGe₂ under pressure. *Physical Review B - Condensed Matter and Materials Physics*, 70(13):1–6, 2004. (Cited in page 76.)
- [190] Boris Dorado, Bernard Amadon, Michel Freyss, and Marjorie Bertolus. DFT+U calculations of the ground state and metastable states of uranium dioxide. *Physical Review B - Condensed Matter and Materials Physics*, 79(23):1–8, 2009. (Cited in page 76.)
- [191] Christian Wäckerlin, Aleš Cahlík, Joseba Goikoetxea, Oleksandr Stesovych, Daria Medvedeva, Jesús Redondo, Martin Švec, Bernard Delley, Martin Ondráček, Andres Pinar, Maria Blanco-Rey, Jindrich Kolorenc, and Andres Arnau Pavel Jelínek. The Role of the Magnetic Anisotropy in Atomic-Spin Sensing of 1D Molecular Chains. jan. (Cited in pages 86 and 97.)
- [192] L. Peters, I. Di Marco, O. Grånäs, E. Şaşloğlu, A. Altun, S. Rossen, C. Friedrich, S. Blügel, M. I. Katsnelson, A. Kirilyuk, and O. Eriksson. Correlation effects and orbital magnetism of Co clusters. *Physical Review B*, 93(22):1–10, 2016. (Cited in page 87.)
- [193] Aron J. Cohen, Paula Mori-Sánchez, and Weitao Yang. Insights into current limitations of density functional theory. *Science*, 321(5890):792–794, 2008. (Cited in page 91.)
- [194] Peter E. Blöchl, O. Jepsen, and O. K. Andersen. Improved tetrahedron method for Brillouin-zone integrations. *Physical Review B*, 49(23):16223–16233, 1994. (Cited in page 99.)

